STUDIES ON THE DEVELOPMENT OF MAGNETOELECTRIC CERAMIC COMPOSITES

A THESIS SUBMITTED TO
THE GRADUATE SCHOOL OF NATURAL AND APPLIED SCIENCES
OF
MIDDLE EAST TECHNICAL UNIVERSITY

BY

YANKI BAŞARAN

IN PARTIAL FULFILLMENT OF THE REQUIREMENTS
FOR
THE DEGREE OF MASTER OF SCIENCE
IN
METALLURGICAL AND MATERIALS ENGINEERING

JUNE 2008

Approval of the thesis:

STUDIES ON THE DEVELOPMENT OF MAGNETOELECTRIC CERAMIC COMPOSITES

Submitted by **YANKI BAŞARAN** in partial fulfillment of the requirements for the degree of **Master of Science in Metallurgical and Materials Engineering Department, Middle East Technical University** by,

Prof. Dr. Canan Özgen
Dean, Graduate School of **Natural and Applied Sciences**

Prof. Dr. Tayfur Öztürk
Head of Department, **Metallurgical and Materials Engineering**

Prof. Dr. Muharrem Timuçin
Supervisor, **Metallurgical and Materials Engineering Dept., METU**

Examining Committee Members:

Prof. Dr. Macit Özenbaş
Metallurgical and Materials Engineering Dept., METU

Prof. Dr. Muharrem Timuçin
Metallurgical and Materials Engineering Dept., METU

Prof. Dr. Mehmet Parlak
Physics Dept., METU

Prof. Dr. Abdullah Öztürk
Metallurgical and Materials Engineering Dept., METU

Assist. Prof. Dr. Arcan Dericioğlu
Metallurgical and Materials Engineering Dept., METU

Date: 19.06.2008

I hereby declare that all information in this document has been obtained and presented accordance with the academic rules and ethical conduct. I also declare that, as required by these rules and conduct, I have fully cited and referenced all material and results that are not original to this work.

Name, Last name : Yankı Başaran

Signature :

ABSTRACT

STUDIES ON THE DEVELOPMENT OF MAGNETOELECTRIC CERAMIC COMPOSITES

Başaran, Yankı
M.S., Department of Metallurgical and Materials Engineering
Supervisor: Prof. Dr. Muharrem Timuçin

June 2008, 134 pages

The aim of this thesis work was to develop magnetoelectric (ME) composites consisting of piezoelectric and magnetostrictive components. The piezoelectric constituent was selected as a PZT ceramic modified by strontium, bismuth and manganese. The magnetostrictive phase was nickel ferrite (NF) ceramic doped by cobalt, copper and manganese. The properties of component phases were optimized in order to enhance the ME effect in the composite.

In the first part of the thesis, effects of sintering temperature on the dielectric and piezoelectric properties of PZT and on the electrical and magnetic properties of NF ceramics were investigated in the temperature range covered from 1150 to 1250 °C. The best piezoelectric properties in PZT were attained at 1250 °C. At this sintering temperature, values of piezoelectric strain coefficient, dielectric constant, and electromechanical coupling coefficient were 434 pC/N, 1320 and 0.48, respectively. NF ceramics showed poor densification; 80 %TD was attained at 1250 °C. In order to obtain higher densities in ferrites, Bi_2O_3 was used as a sintering aid. Addition of Bi_2O_3 enhanced densification up to 97 %TD, and improved electrical and magnetic properties of ferrites. Highest DC-resistivity of 1.15×10^8 ohm-cm and highest magnetostriction of ~26 ppm were attained in NF ceramics doped with 1 wt% Bi_2O_3.

In the second part of the thesis, ME composites were manufactured either as bulk composites or as laminated composites. The efficiency of different composite types was evaluated in terms of voltage output in response to the applied magnetic field. Higher outputs were observed in laminated composites.

Keywords: PZT, dielectric and piezoelectric properties, nickel ferrite, magnetostriction, ME effect

ÖZ

MANYETOELEKTRİK SERAMİK KOMPOZİTLERİN GELİŞTİRİLMESİ ÜZERİNDE ÇALIŞMALAR

Başaran, Yankı
Y. Lisans, Metalurji ve Malzeme Mühendisliği Bölümü
Tez Yöneticisi: Prof. Dr. Muharrem Timuçin

Haziran 2008, 134 sayfa

Bu tez çalışmasının amacı, piezoelektrik ve manyetik gerinim özelliklerine sahip bileşenlerden oluşan manyetoelektrik (ME) kompozitlerin geliştirilmesidir. Piezoelektrik bileşen olarak stronsiyum, bizmut ve manganez ile doplanmış PZT seçilmiştir. Manyetik gerinim gösteren bileşen ise kobalt, bakır ve manganez ile katkılanmış nikel ferrittir (NF). Bileşen fazların özellikleri kompozitteki ME etkisini arttırmak için optimize edilmiştir.

Tezin birinci bölümünde, 1150'den 1250 °C'ye kadar olan sıcaklık aralığında, pişirme sıcaklığının PZT'nin dielektrik ve piezoelektrik özellikleri ile NF seramiklerinin elektriksel ve manyetik özelliklerine etkisi incelenmiştir. PZT'de en iyi piezoelektrik özelliklere 1250 °C'de ulaşılmıştır. Bu sinterleme sıcaklığında, piezoelektrik gerinim katsayısı, dielektrik sabiti ve elektromekanik bağlaşma katsayısı değerleri, sırasıyla, 434 pC/N, 1320 ve 0.48 olmuştur. NF seramikleri az yoğunlaşma göstermiştir; 1250 °C'de % 80 teorik yoğunluğa ulaşılmıştır. Ferritlerden daha yüksek yoğunluk değerleri elde etmek için, Bi_2O_3 sinterleme yardımcısı olarak kullanılmıştır. Bi_2O_3 katılması yoğunlaşmayı % 97 teorik yoğunluğa kadar arttırmış ve ferritlerin elektriksel ve manyetik özelliklerini iyileştirmiştir. En yüksek özdirenç 1.15×10^8 ohm-cm ve en yüksek manyetik büzülüm ~26 ppm olarak, ağırlıkça % 1 Bi_2O_3 içeren NF seramiklerinde elde edilmiştir.

Tezin ikinci bölümünde, ME kompozitler hem parçacık kompozit hem de lamine kompozit olarak üretilmiştir. Farklı çeşitteki kompozitlerin etkinliği, uygulanan manyetik alan karşısındaki voltaj üretimi ile değerlendirilmiştir. Lamine kompozitlerde daha yüksek dönüşme verimi gözlenmiştir.

Anahtar Kelimeler: PZT, dielektrik ve piezoelektrik özellikler, nikel ferrit, manyetik gerinim, ME etkisi

To Şenol, Emin and
Çağrı Başaran,

ACKNOWLEDGEMENTS

I would like to express my sincere gratitude to my supervisor Prof. Dr. Muharrem Timuçin for his guidance, support and encouragement during the study. Without his supervision I would not complete this study.

I am also thankful to Dr. İbrahim Çam from METU Central Laboratory for his valuable criticism and helps.

My special thanks go to Volkan Kalem and M. Barış Okatan for their continuous support and valuable recommendations throughout this study.

I would also like to thank to Necmi Avcı for XRD analyses and Cengiz Tan for the instruction in SEM studies.

Thanks are also extended to Gürol İpek, Onur Bütün and A. İrfan Bostanlı from BİAS Mühendislik for their help and guidance in magnetostriction measurements.

I would like to express my sincere thanks to Ceren Büyükyıldız, Burcu Araç, and Göktürk Emre Uzunçakmak for always being supportive in my life. I am also thankful to my colleagues Sıla Süer, Ali Erdem Eken and Nurdan Gürkan for their friendship and helps.

Finally, I want to express my great thanks to my mother, Şenol Başaran, my father, Emin Başaran, and my brother, Çağrı Başaran for their endless love, invaluable trust, support and guidance throughout my life.

TABLE OF CONTENTS

CHAPTERS

APPENDICES

LIST OF TABLES

LIST OF FIGURES

CHAPTER 1

INTRODUCTION

Magnetoelectric (ME) effect is defined as the induction of magnetization in a material under the applied electrical field or induction of electrical polarization under the applied magnetic field [1]. This effect was noticed first in single phase materials and later in composites composed of piezoelectric and magnetostrictive constituent phases [2].

The observed ME effect in composites is a result of product property [3, 4]. When magnetic field is applied to the composite, dimensions of ferrite grains change due to magnetostriction and this strain passes along the piezoelectric phase and induces electric field due to piezoelectricity. The efficiency of ME composites have been represented with the voltage output from the composites in response to an applied magnetic field.

ME composites can be classified into three groups according to the production technique as observed from the literature review [5]. First class is bulk (or particulate) composites, which are manufactured by blending the powders of the piezoelectric and magnetostrictive constituent phases in specific portions and sintering the compact. Second one is laminated (or layered) ME composites, which are produced either by stacking and bonding the sintered piezoelectric and magnetostrictive disc ceramics or by laminating thin layers of constituent phases followed by sintering the laminate. Third group is in situ grown composites, which are produced by unidirectional cooling of a eutectic melt.

The first observation of the ME effect gave rise to a lot of excitement due to the obvious potential of the cross correlation between the magnetic and electrical properties of a material for technical applications [1]. ME effect makes the conversion of magnetic energy into electrical energy, or vice versa, possible. Thus ME composites can be used in many devices such as magnetic probes in detecting ac or dc fields, transducers or leak detectors for microwave ovens. Moreover, due to their hysteretic nature they can be utilized in memory devices [1, 5]. Wood and Austin [6] reviewed the possible applications for ME materials as well as the characteristics of 15 devices including switches, rectifiers and sensors.

Although ME composites are potential candidates for numerous devices, no commercial application has yet been found for these composites due to the lack of reproducibility in achieving the product property in the composite material [1, 5]. The roots of the problem may lie in the methods followed during composite manufacture.

The main objective of the present thesis work was to conduct an optimization study on the piezoelectric and magnetic ceramics which constitute the components of the ME composite. Later, ME composites were manufactured from powders or sintered discs of the optimized ceramics with the aim of comparing the performance of two different types of such composite structures.

In the first part of the thesis, influence of sintering temperature on the dielectric and piezoelectric properties of piezoelectric constituent ceramics and on the electrical and magnetic properties of magnetostrictive constituent ceramics were examined together with their microstructural analyses. In the second part of the study, bulk and laminated ME composites were produced. Composites were characterized by means of ME outputs. In previous studies [4, 7], ME composites were sintered either at low temperatures such as 1000 ºC for long durations like 12 h or at higher temperatures like 1250 ºC for shorter durations. In the present study, however, the temperature interval in the ceramic production was selected to range from 1150 °C to 1250 °C and soaking time was kept constant at 2 h with the intention to explore how processing under more practical ceramic processing conditions would influence the properties.

CHAPTER 2

LITERATURE SURVEY

2.1 Piezoelectricity

The ability of certain crystalline materials to develop an electric charge in response to a mechanical stress is called piezoelectricity. This characteristic property is referred to as the direct piezoelectric effect and was discovered first in 1880 by Jacques and Pierre Curie in various substances including Rochelle salt, quartz and tourmaline [8]. Soon it was found that piezoelectric materials could be also utilized for the reverse effect, i.e., material shows deformation (strain) when exposed to an applied electric field. This response is called the converse piezoelectric effect. Converse effect is useful for actuator applications, whereas direct effect is beneficial in sensor applications [9]. The direct and converse effects are represented schematically in Figure 2.1.

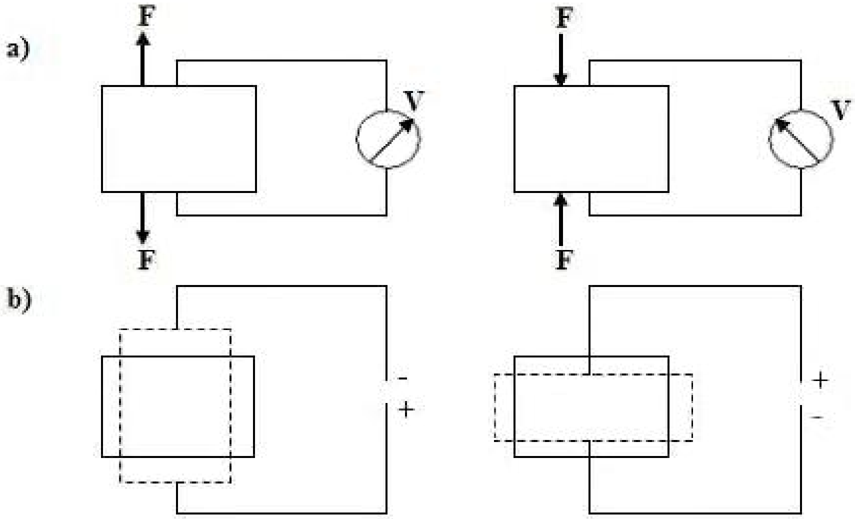

Figure 2.1 a) Direct and b) Converse piezoelectric effect.

An understanding of the concept of piezoelectricity in solid begins with the comprehension of the internal structure of the material. The smallest repeating unit of the lattice and the specific symmetry possessed by it determines whether it is possible for the crystal to show piezoelectricity. All crystals can be divided into 32 different point groups. Of the 32 point groups, 21 classes lack center of symmetry and 20 of these are piezoelectric. Noncentrosymmetric structure is all important for the presence of piezoelectricity when it is considered that a homogeneous stress is centrosymmetric and cannot produce an unsymmetric result (e.g. a vector quantity like electric polarization, which has positive and negative ends) if the material does not lack a center of symmetry. For piezoelectricity, the effect is linear and reversible. The magnitude of the polarization and the sign of the charge produced are dependent on the magnitude and type (tensile or compressive) of the stress, respectively [10].

Piezoelectric activity is generated in a ferroelectric ceramic after poling process [8]. Before poling, due to the random orientation, piezoelectric effects of the individual domains cancel each other [11]. During poling, ceramic is electroded, and a sufficiently high electric field is applied across the electrodes such that dipoles within the individual domains are reoriented and aligned in the direction of the applied field. In poling treatment, due to switching of domains, there is a small expansion of the material along the poling axis and a contraction in directions perpendicular to it [9]. An illustration of the poling effect on a ceramic microstructure is given in Figure 2.2.

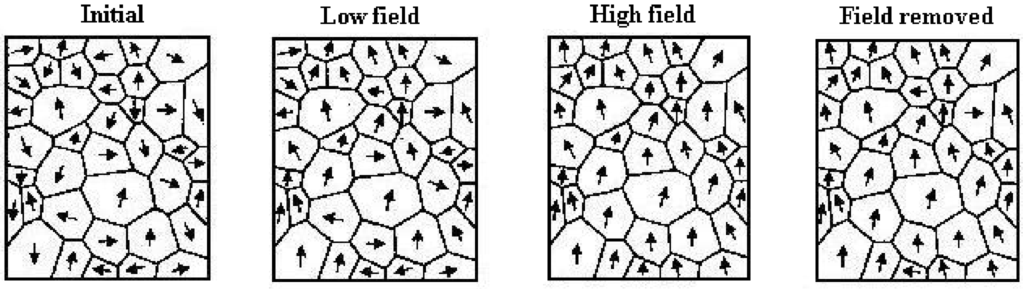

Figure 2.2 Microstructural changes in a piezoelectric body during poling [9].

2.2 Perovskite Structure

A large group of piezoelectric ceramics crystallizes in the perovskite structure. The formula, ABO_3, can be used to represent a perovskite compound where A stand for 2+ valence ion and B for 4+ valence ion. As seen from the structure shown in Figure 2.3, in a perovskite unit cell, large A cations are at the corners, small B cation occupies the body center and oxygen ions are located in the face centers. The structure is a network of corner-linked oxygen octahedral, with the smaller cation filling the octahedral holes and the large cations filling the sites within the octahedral structure [8].

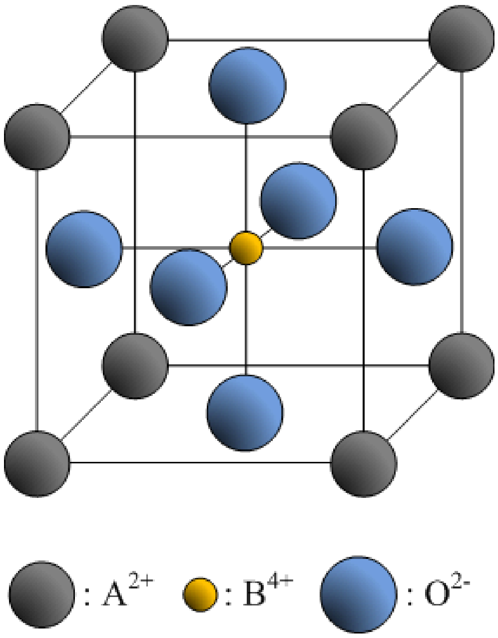

Figure 2.3 The perovskite structure.

In the case of lead zirconate titanate system, which will be discussed in detail in the following sections, A ion is Pb^{2+}, and B ion is Ti^{4+} and/or Zr^{4+}. In the oxygen octahedral, Ti^{4+} cation tends to shift to minimum energy configurations by occupying the off-center positions. This noncentrosymmetry gives rise to permanent dipoles to occur, below the Curie temperature. The dipoles are ordered and give a domain structure with a net spontaneous polarization within the domains.

2.3 Dielectric and Piezoelectric Parameters

The definition of commonly used material coefficients that are employed in the characterization of piezoelectric materials are provided below.

2.3.1 Dielectric Constant, K

The ratio between the charge stored on an electroded slab of material brought to a given voltage and the charge stored on a set of identical electrodes separated by vacuum is known as the relative dielectric constant, K [8]. It is commonly referred to simply as the dielectric constant, and is dimensionless.

The relative dielectric constant may be measured at constant (zero) stress or constant (zero) strain. The former is called the 'free' dielectric constant and denoted by the superscript T, whereas the latter is referred to 'clamped' dielectric constant and is denoted by the superscript S [8].

2.3.2 Loss Tangent, tanδ

The charge stored on a dielectric has both real (in phase) and imaginary (out of phase) components under alternating voltages. The ratio of the imaginary component to the real component is expressed as the dielectric loss. This is also known as dissipation factor, and frequently called the loss tangent, tanδ, in the literature [8].

2.3.3 Piezoelectric Strain Coefficient, d

The piezoelectric strain coefficient is represented by the symbol d. For the direct piezoelectric effect, the piezoelectric strain coefficient can be expressed in terms of dielectric displacement, D, and stress, T, according to:

$$d = \frac{D}{T} \tag{2.1}$$

where, unit of d is coulombs/Newton.

For the converse effect in which an applied electric field, E, produces strain, S, the relationship can be written as:

$$d = \frac{S}{E} \tag{2.2}$$

where, d is expressed in terms of meters/Volt.

For both direct and converse effects, piezoelectric strain coefficient is the proportionality constant and is numerically identical. The relationship can be shown as:

$$d = \frac{D}{T} = \frac{S}{E} \tag{2.3}$$

For materials utilized in motional or vibrational devices such as sonar or ultrasonic cleaner transducers, high d constants are desirable [8].

In a piezoelectric material, the magnitude of the piezoelectric action varies with direction [8]. In order to show the directionality of the piezoelectric response, a subscript notation is used, after defining crystallographic axis in the material. Axis 1, 2, and 3 in Figure 2.4 describe the normal stress (or strain) directions whereas arrows 4, 5 and 6 are used to indicate the ones for shear stress (strains). In a piezoelectric property d_{ij}, the subscript i designates the direction of poling whereas subscript j denotes the response direction. For piezoelectric materials, poling is conventionally applied along the 3-direction.

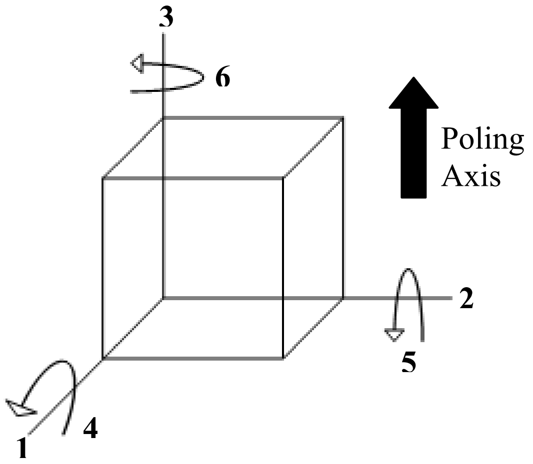

Figure 2.4 Notation of axis for a poled piezoelectric element.

Expressions describing the dielectric displacement that is developed when the material is subjected to a change in stress, or the resulting strain that is developed under an applied electric field can be written by including the directionality of the response in a general form of [9]:

$$D_i = d_{ij} \cdot T_j + \varepsilon_{ii}^T \cdot E_i \tag{2.4}$$

$$S_j = s_{ij}^E \cdot T_j + d_{ij} \cdot E_i \tag{2.5}$$

where ε^T is the free dielectric constant and s^E is the material compliance. Equation 2.4 is for the direct piezoelectric effect, whereas Equation 2.5 stands for the converse effect.

2.3.4 Electromechanical Coupling Factor, k

The efficiency of a piezoelectric material to convert mechanical energy into electrical energy, or vice versa, is expressed by its electromechanical coupling coefficient, k. The energy conversion is shown in terms of k^2 according to the following formula [9]:

$$k^2 = \frac{\text{mechanical energy converted to electrical energy}}{\text{input mechanical energy}}$$

$$k^2 = \frac{\text{electrical energy converted to mechanical energy}}{\text{input electrical energy}}$$

Since the conversion of mechanical to electrical energy is always incomplete, k is always less than unity [8].

2.3.5 Equivalent Circuit

The equivalent circuit of a piezoelectric body near a fundamental resonance is shown schematically in Figure 2.5. The part of the circuit with R-L-C elements is referred to as mechanical branch, which is parallel to the electrical branch comprised of a capacitance element. At the resonant frequency, the impedances $2\pi f_r L_1$ and $1/2\pi f_r C_1$ are equal in magnitude and opposite in sign such that the total impedance of the mechanical branch is given only by the mechanical resistance R_1 which is comparatively quite small [8].

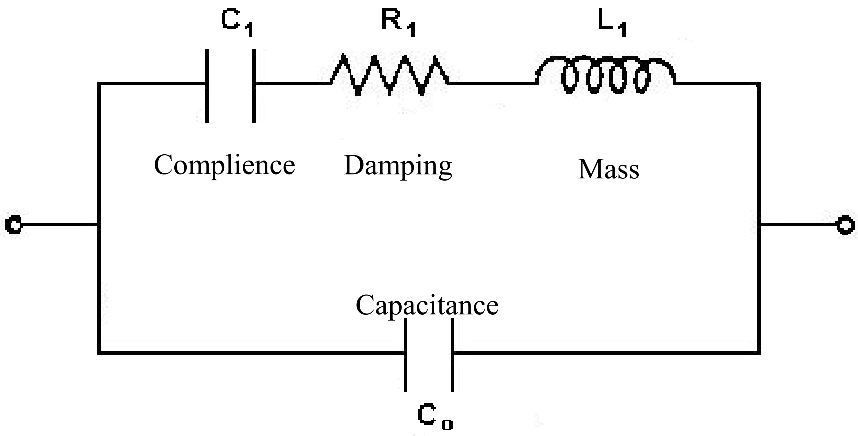

Figure 2.5 Equivalent circuit of a piezoelectric ceramic.

Elements of the equivalent circuit are used in determination of various piezoelectric properties.

2.3.6 Mechanical Quality Factor, Q_m

The mechanical quality factor is the reciprocal of internal friction [11]. It is described as the ratio of strain in phase with stress to strain out of phase with stress [8].

Level of Q_m is dominated by the existence of movable domain walls. Since a vibrating body is heated due to the energy lost to mechanical damping, high Q_m is desirable in a piezoelectric driver or resonator [8].

2.3.7 Curie Point, T_C

If the capacitance of poled ceramics was measured as a function of temperature from RT to higher, a maximum is observed in the T-C plot. The temperature at which this maximum occurs is referred to as Curie point, T_C.

When ferroelectric ceramics are heated above their T_C, they possess a centrosymmetric cubic structure which shows paraelectric behavior; hence no piezoelectric activity is observed in this temperature regime [9]. Below T_C, ceramic attains noncentrosymmetric structure and piezoelectricity is observed due to the existence of electric dipoles within the unit cell.

2.4 Barium Titanate and Lead Zirconate Titanate

The first synthetic piezoelectric substance, barium titanate ($BaTiO_3$), was developed in 1940. When it was tested in the laboratory, dielectric constant in the range of 1100 was observed. This was an enormous value at that time since rutile (TiO_2) had the known highest value with a dielectric constant of about 100. Coupling factors of $BaTiO_3$ are substantially higher than that of any previously known material, except for Rochelle salt. Moreover, it is chemically more stable than Rochelle salt, it has a wider temperature range of operations and has the advantage of easy in manufacturing by ceramic processing techniques [8].

Development of $BaTiO_3$ piezoelectrics continued with compositional modifications, which were desirable to improve the temperature stability or voltage outputs. Piezoelectric lead niobate, followed by several niobate solid solution systems, was discovered in 1952. An advance of great practical importance was the discovery of lead zirconate titanate (PZT) solid solutions showing very strong and stable piezoelectric effects. Since then, PZT ceramics have been the dominant piezoelectric materials [8].

Until now, piezoelectric ceramics have been formulated from a number of compositions containing $BaTiO_3$, barium strontium titanate, PZT, lead niobate, bismuth titanate, sodium potassium niobate, lead magnesium niobate and other relaxor ferroelectric compositions. The use of $BaTiO_3$ for piezoelectric applications has been largely supplanted by PZT-based materials. This is because PZT compositions possess higher electromechanical coupling coefficients and a wide range of dielectric constants. Moreover they have higher Curie point permitting higher operation temperatures in service [9].

2.5 The Lead Zirconate Titanate System

The piezoelectric material PZT was developed as a solid solution phase in the PbO-ZrO_2-TiO_2 ternary system. The isothermal phase relations of this system were first studied by Ikeda et al. at 1100 °C [12, 13]. As seen from the diagram reproduced in Figure 2.6, there exists an area extending as a narrow band between the compounds $PbTiO_3$ and $PbZrO_3$ representing the stability field of homogeneous PZT solutions. This implies that, a wide range of $Pb(Zr_{1-x}Ti_x)O_3$ ceramics can be produced with x varying between 0 to 1 since Zr^{4+} and Ti^{4+} cations can occupy positions in the perovskite lattice interchangeably. As should be noted from the diagram, considerable excess of TiO_2 and ZrO_2 can be dissolved in the PZT solid solutions before the precipitation of a second phase. This means that PZT can retain its homogeneous and single phase structure allowing limited loss of lead during ceramic manufacturing.

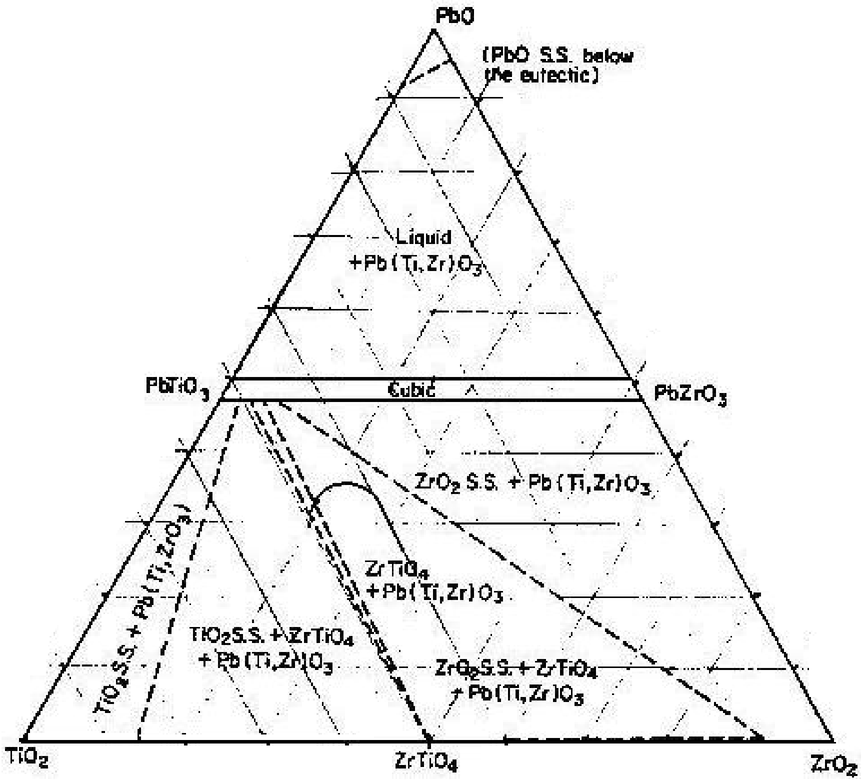

Figure 2.6 The isothermal section of the system PbO-ZrO_2-TiO_2 at 1100 °C after Ikeda et al.[12, 13].

Phase relations between $PbZrO_3$ and $PbTiO_3$ at subsolidus temperatures are displayed in Figure 2.7. The upper boundary extending from 235 °C at the $PbZrO_3$ corner to 480 °C at the $PbTiO_3$ corner is the locus of Curie temperatures for PZT solid solutions. Above this boundary, the structure is cubic with no piezoelectric activity. Below the boundary, the PZT ceramics may have any one of the three crystalline forms, orthorhombic, rhombohedral or tetragonal, depending on their ZrO_2 /TiO_2 ratio. The orthorhombic phase, occupying the limited area near the $PbZrO_3$ corner, is paraelectric whereas the rhombohedral and the tetragonal phases possess piezoelectric properties.

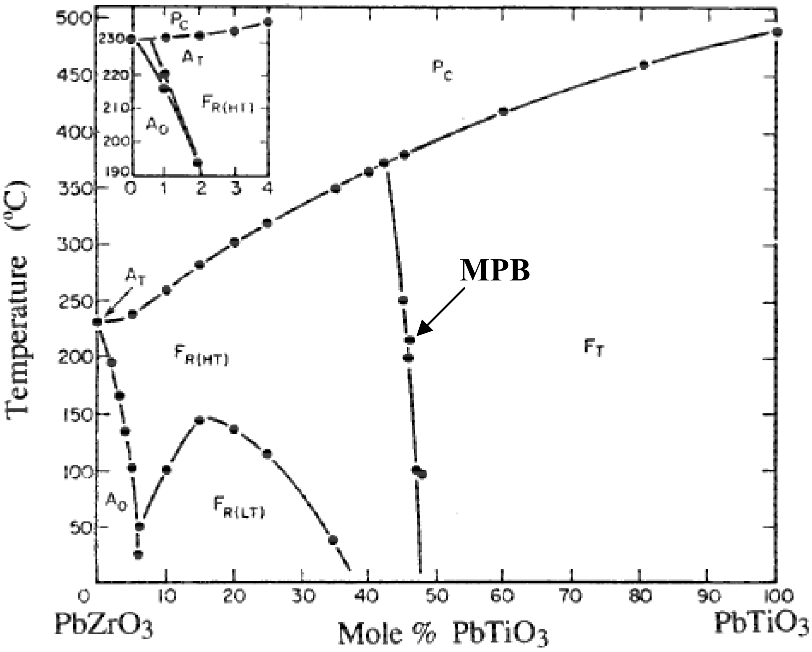

Figure 2.7 $PbZrO_3$-$PbTiO_3$ (PZT) subsolidus phase diagram [8].

The rhombohedral and tetragonal phases are separated from each other by the boundary named Morphotropic Phase Boundary (MPB). MPB has quite a large significance in PZT technology since compositions close to this boundary show optimum piezoelectric activity [8]. Both phases near the MPB are ferroelectric. The tetragonal phase has six easy polarization directions, <001>, and the rhombohedral phase has eight easy polarization directions, <111>. In compositions near the MPB, both phases coexist hence the total polarization directions increase to fourteen. As indicated by Randall et al. [14], anomalously high piezoelectric properties are obtained when PZT compositions are selected in the vicinity of the MPB due to the large number of polarization directions.

2.6 Compositional Modifications and Previous Studies on PZT

While the MPB is helpful in tailoring the properties of PZT ceramics, it has become customary to modify them greatly with the use of dopants. Because of their immense role on the performance of PZT ceramics, the effects of dopants have been studied quite extensively.

In a very broad sense, the dopants may lead to the formation of “soft” or “hard” PZT ceramics. Soft ones are produced by modifying the base PZT composition with higher valence cations, called donors. Donor additives are generally compensated by A-site vacancies. This type of ceramics exhibit enhanced domain wall translation and reorientation, therefore they have high dielectric constant, maximum coupling factors, high dielectric loss and higher aging rates. Hard PZT ceramics, on the other hand, are produced by the addition of lower valence cations, called acceptors, into the lattice. Acceptor ions create oxygen vacancies which in turn pin the domain movement giving lower dielectric constant, low dielectric loss and lower aging rates [9].

Strontium (Sr) has long been known as a hardener in the PZT systems. For every atom of Sr addition, Curie point of the ceramic decreases about 9.5 °C and room temperature dielectric constant increases. Due to its lattice straining effect, Sr also has contribution to the piezoelectric strain coefficient. Loss tangent remains quite low and electromechanical coupling of the ceramic increases slightly with the addition of Sr [8].

Longtu et al. [15] used bismuth (Bi) as a component of a low temperature frit in the production of a PZT ceramic having $Pb_{0.95}(Zr_{0.52}Ti_{0.48})O_3$+(0.1-0.4)wt%$MnO_2$ composition. The ceramic attained 96 % of theoretical density when sintered at 960 ºC in the presence of the frit. Electromechanical properties of the ceramic were enhanced when compared to those of the ceramic sintered at 1250 ºC without frit.

The effects of manganese (Mn) modification on PZT systems were studied by He and Li [16]. Their work was confined to two different PZT compositions soaked in the temperature range 1240 to 1270 ºC for a fixed duration of 2 h. They noted that Mn might exist in PZT structure as Mn^{2+} and Mn^{3+} ions. For the composition of $Pb_{0.95}Sr_{0.05}(Zr_{0.52}Ti_{0.48})O_3$ when Mn concentration was less than 0.5 mol%, Mn ion was incorporated in the A-site increasing piezoelectric strain coefficient and electromechanical coupling factor. This was attributed to the formation of vacancies in the Pb position that made domain walls mobile. In the intermediate concentrations between 0.5-1.5 mol%, Mn was incorporated in B site, acting like an acceptor and it increased mechanical quality factor of the ceramic without changing electromechanical coupling factor or piezoelectric strain coefficient considerably. When Mn concentration exceeded 1.5 mol%, Mn accumulated at grain boundaries degrading the piezoelectric properties.

Çağatay [17] examined the combined effects of Sr, Mn and Bi modifications on the electromechanical properties of $Pb(Zr_{0.53}Ti_{0.47})O_3$ ceramic sintered by soaking at 1260 ºC for 2 h. It was shown that Sr stabilized the dielectric properties and Bi led to an increase in dielectric constant, coupling coefficient, and piezoelectric strain coefficient. In the presence of Mn, mechanical quality factor of the ceramics was improved together with reduction in piezoelectric strain coefficient, coupling factor, and dielectric constant. Her study showed that combinations of Sr, Mn, and Bi as dopants could be effective in attaining the soft and hard properties. Optimum results for piezoelectric strain coefficient and mechanical quality factor were obtained from $Pb_{0.95}Sr_{0.05}(Zr_{0.53}Ti_{0.47})O_3$+1wt%$Bi_2O_3$+0.4mol%MnO composition.

2.7 Ferrites

Ferrites are ceramic materials that are dark grey or black in color [18]. They are divided into three subclasses according to their crystal structures: spinels (cubic ferrites), magnetoplumbite (hexagonal ferrites), and garnets (rare earth ferrites). The cubic ferrites are used as soft magnetic materials, whereas hexagonal ferrites are hard magnets exhibiting permanent magnetism. Garnets are utilized in high frequency microwave applications [19]. These subclasses are distinguished with respect to the molar ratio of Fe_2O_3 to the other oxide component within the ceramic as shown in Table 2.1.

Table 2.1 Summary of ferrite structure types, typified by changes in the Fe_2O_3-MeO (or Me_2O_3) modifier oxide ratios [9].

Spinel	1 Fe_2O_3-1 MeO	where MeO is a transition metal oxide
Magnetoplumbite	6 Fe_2O_3-1 MeO	where MeO is a divalent metal oxide from group IIA – BaO, CaO, SrO
Garnet	5 Fe_2O_3-3 Me_2O_3	where Me_2O_3 is a rare earth metal oxide

2.8 Spinel Structure

Spinel ferrites represent the widest subclass. They exhibit intriguing intrinsic properties such as high electrical resistivity and low magnetic losses [20].

The spinel structure, which crystallizes in the cubic symmetry, takes its name from the mineral $MgAl_2O_4$. The general formula of the spinel ferrite is shown with $MeFe_2O_4$ where Me represents one of the divalent ions of the transition metals Mn, Fe, Co, Ni, Cu, and Zn, or Mg and Cd. It is also possible to have a combination of these ions (mixed ferrites) and to replace some or all of the Fe^{3+} ions with others such as Al^{3+} and Cr^{3+} leading to the formation of mixed crystals with aluminates and chromites [18, 21].

The spinel unit cell consists of eight molecules of $MeFe_2O_4$. In this cubic closed packed structure, the relatively large oxygen ions are arranged accommodating tetrahedral and octahedral interstitial sites (sublattices) for metal cations. Of the 64 tetrahedral sites (A sites) and 32 octahedral sites (B sites), 8 and 16 are occupied, respectively [9]. The unit cell of a spinel lattice is shown in Figure 2.8.

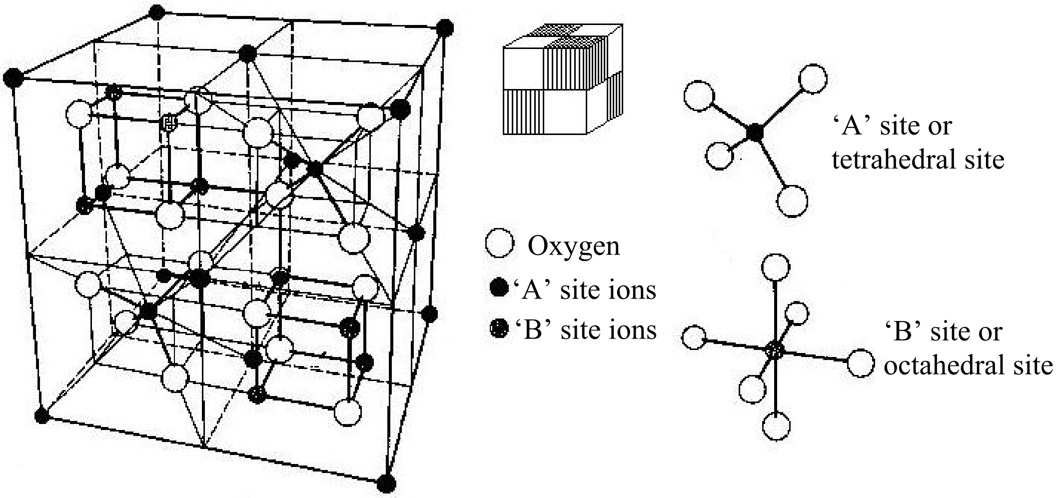

Figure 2.8 Unit cell of the spinel lattice [18].

In the spinel ferrite, cations are distributed among tetrahedral and octahedral sites according to their site preference energies. If divalent cations occupy the tetrahedral sites and trivalent cations occupy the octahedral sites, structure is referred to as "normal spinel", e.g. $ZnFe_2O_4$. If tetrahedral positions are occupied by half of the Fe^{3+} ions and octahedral positions are occupied by the remainder Fe^{3+} ions and divalent cations, compound is called "inverse spinel", e.g. $NiFe_2O_4$ and $CoFe_2O_4$. Cation distribution may also be intermediate between the inverse and normal arrangements [9, 19, 22].

The general cation distribution in the spinel lattice can be shown as

$$(\mathrm{Me}^{2+}_{\delta}\ \mathrm{Fe}^{3+}_{1-\delta})\ [\mathrm{Me}^{2+}_{1-\delta}\ \mathrm{Fe}^{3+}_{1+\delta}]\ \mathrm{O}_4$$

where the ions on tetrahedral sites are given in round brackets and the ions in octahedral sites are given in square brackets. The quantity of δ is the measure of inversion and its value is between 0 and 1 [21].

2.9 Magnetism in Ferrites

Ferrimagnetism in solids is due to the antiparallel alignment of the magnetic moments of the ions, which are produced by electron spin and electron orbits around the nucleus of the atom, on different sublattices in the crystal [9].

A ferrimagnetic oxide shows spontaneous magnetization in the form of Weiss domains due to energy considerations. Domains are the areas within which magnetic dipoles are aligned in the same direction. They are separated by the domain walls, called Bloch walls, which are comprised of regions having transition of spin orientation. In the absence of a magnetic field, due to the random orientation of the domains, net magnetization within the structure is zero [9, 18].

2.10 Some of the Magnetic and Electrical Properties of Ferrites

2.10.1 Magnetocrystalline Anisotropy

A spinning electron, which is free from any restraints, can be aligned by an infinitely small field, giving an infinite permeability. However, due to the spin-orbit coupling in the lattice, spins are oriented relative to the crystal in a minimum energy direction, i.e. 'easy direction'. The energy needed to rotate the magnetization vector from this easy direction to others is called the magnetocrystalline anisotropy energy, E_K. For cubic structures like spinels, E_K can be expressed with anisotropy constants, K_1 and K_2, according to,

$$E_K = K_1\left(\alpha_1^2 \cdot \alpha_2^2 + \alpha_2^2 \cdot \alpha_3^2 + \alpha_3^2 \cdot \alpha_1^2\right) + K_2\left(\alpha_1^2 \cdot \alpha_2^2 \cdot \alpha_3^2\right) + \ldots \qquad (2.6)$$

where α_i's are direction cosines of the magnetization vector relative to the crystallographic axes [22]. If it is assumed that K_2 is negligibly small, magnitude of anisotropy is proportional to K_1. Crystal anisotropy constant of selected ferrites are listed in Table 2.2. Anisotropy is strongly influenced by the cations present in the lattice [9].

Table 2.2 Room temperature anisotropy constant of selected ferrites [20, 22].

Ferrite	K_1 (kJ/m^3)
Fe_3O_4	- 11
$NiFe_2O_4$	- 6.2
$CoFe_2O_4$	- 380
$CuFe_2O_4$	- 6
$MnFe_2O_4$	-2

2.10.2 Magnetostriction, λ

Magnetostriction, which is also an anisotropy effect, is the change in length of a crystal along the direction of an applied magnetic field (Joule effect). It increases with the applied field until saturation and is due to the reorientation of domains within the ceramic. Reverse of this phenomenon is also possible (Villari effect), i.e. application of a stress to a magnetostrictive material results in change in crystal lattice energy and hence in magnetic properties [9]. From the atomistic point of view it could be attributed to spin-orbit lattice couplings such that changes in the spin directions cause changes in the orbit orientation. Since orbits are restrained by the lattice, this change results in slight alteration in lattice dimensions [22].

Magnetostriction may be positive or negative and its magnitude changes with the composition and previous history of the material, applied field strength and temperature. Positive values imply the elongation of the material in the applied field direction. In a polycrystalline material, λ occurring at saturation is named as saturation magnetostriction, λ_S [20].

In cubic structures, λ_S can be specified by a two-constant system, with the constants λ_{100} and λ_{111}, where subscripts represent the direction of magnetostriction. After introducing the direction cosines α and β for the angle between the direction of magnetization and the respective crystal axis, λ_S can be expressed by the following relationship [20]:

$$\lambda_S = \frac{3}{2}\lambda_{100}\left(\alpha_1^2\beta_1^2 + \alpha_2^2\beta_2^2 + \alpha_3^2\beta_3^2 - \frac{1}{3}\right) + 3\lambda_{111}\left(\alpha_1\alpha_2\beta_1\beta_2 + \alpha_2\alpha_3\beta_2\beta_3 + \alpha_1\alpha_3\beta_1\beta_3\right) \quad (2.7)$$

Saturation magnetostriction varies with the crystallographic directions for single crystals; hence for the ceramic form, λ_S is an average of the single crystal values [22]. By averaging Equation 2.7 over all possible directions, for a polycrystalline substance λ_S will be

$$\lambda_S = \frac{2}{5}\lambda_{100} + \frac{3}{5}\lambda_{111} \quad (2.8)$$

Data on saturation magnetostriction for selected ferrites are given in Table 2.3.

Table 2.3 Saturation magnetostriction constant for selected ferrites [22].

Ferrite	**λ_S (10^{-6})**
Fe_3O_4	+ 40
$NiFe_2O_4$	- 26
$Ni_{0.5}Zn_{0.5}Fe_2O_4$	- 11
$CoFe_2O_4$	- 110
$MgFe_2O_4$	- 6
$MnFe_2O_4$	- 5

2.10.2.1 Giant Magnetostriction and TERFENOL-D

Magnetostriction occurs to some degree in all magnetic materials, however, only a small number of materials containing rare earth elements exhibit giant magnetostriction [23].

In rare earth elements, the unbalanced spins are sheltered in inner orbitals. These orbitals neither overlap with neighboring orbitals nor participate in the bonding.

This occurs because in rare earths 6s and 5d states are occupied by two or three electrons before the more tightly bound 4f shell is filled. In addition to the spin imbalance, the partially filled 4f shell has an orbital imbalance giving an orbital contribution to the magnetic moment [23].

Rare earth elements preserve essentially the same magnetostriction in the element, alloy and compound forms since magnetic moments of the rare earths are correlated to the electrons occupying 4f shells. The giant descriptive for these magnetostrictive materials originates from the high strain values they possess. For instance, terbium (Tb) and dysprosium (Dy) show a strain of almost 1% (10,000 ppm) when compared to 40 to 70 ppm room temperature strains of transition metals such as Ni, Co, and Fe. However, this magnetostriction exists in the elements at cryogenic temperatures and reduces to zero at room temperature due to their low Curie points [23].

In 1970's it was discovered that the alloy $TbFe_2$, called Terfenol, possess the highest room temperature strain among other RFe_2 (R= rare earth elements) compounds as shown in Figure 2.9. However, Terfenol has high magnetic anisotropy which necessitates higher fields to induce magnetostriction. During the studies on Terfenol, Dy was found to be the most effective rare earth element in lowering the magnetization anisotropy while producing a minimal reduction in strain [23]. This development gave the alloy Terfenol-D. It was discovered first in Naval Ordnance Laboratory. Its name was derived from its constituent, 'Ter' for terbium, 'fe' for iron, 'nol' for Naval Ordnance Laboratory and '-D' for dysprosium and is shown with the formula of $Tb_{1-x}Dy_xFe_2$, x in the formula is generally 0.3.

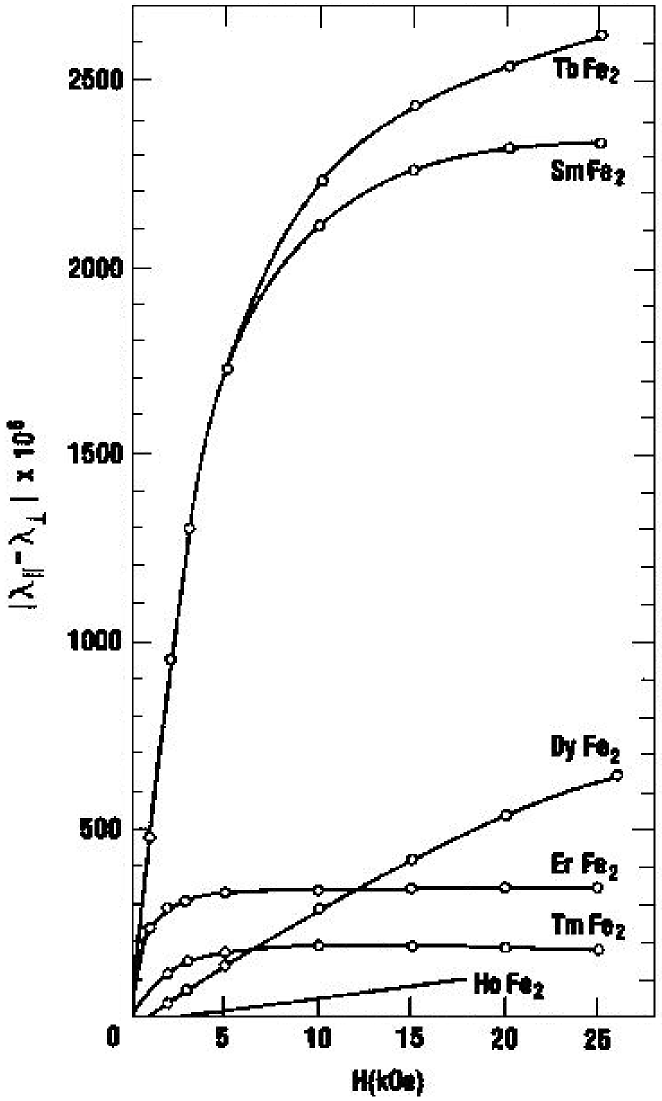

Figure 2.9 Room-temperature magnetostriction, λ(//)-λ(⊥), of rare earth-Fe_2 polycrystals vs magnetic field [23].

Terfenol-D possess currently known highest room temperature strain in the level of 2400 ppm [23].

2.10.3 Initial Magnetic Permeability, μ_i

The ratio between the induction and the magnetic field is called the permeability and is shown as $\mu = B/H$. Permeability is a function of the field H. When field is low enough, however, the permeability is a constant, that means it is independent of the field, and is called initial permeability, μ_i. [24].

In a ferromagnetic substance, the initial magnetic permeability can be due to simultaneous spin rotation in each Weiss domain and reversible displacement or bulging of domain walls [21]. μ_i is a microstructure sensitive property [24]. It depends closely on the preparation method, composition and density of the specimen, size and distribution of pores and average size of the crystallites within the specimen. Hence, in the same ceramic material sintered under different conditions the permeability may vary in a wide range.

In order to observe high initial magnetic permeabilities from polycrystalline materials, it is mandatory for materials to have small magnetic anisotropies. Moreover, it is also necessary for the specimen to have sufficiently large crystallite size and minimum amount of porosity [21].

2.10.4 Electrical Properties, DC-resistivity

The Eddy current loss is an important parameter especially in high frequency applications. Eddy currents are generated by the alternating magnetic fields produced by many devices and are minimized in ferrites owing to their high resistivities [18].

The DC-resistivity of ferrites depends on various parameters such as Fe^{2+} ion concentration, grain size (grain to grain boundary ratio), composition stoichiometry, microstructural homogeneity and density (porosity) [25].

Many spinel compositions contain ions that are capable of taking up two or more different valence states [26]. This results in polaron hopping between the multivalent cations of the same atom, which has a detrimental effect on resistivities. For instance in ferrites, electron is transferred between ferrous (Fe^{2+}) and ferric (Fe^{3+}) ions when they are on the same sublattice according to the relationship given below.

$$Fe^{3+} + e^- \leftrightarrow Fe^{2+}$$

Large numbers of such hopping electrons would be present in the lattice under the influence of an applied electric field [26]. Thus, in order to have high electrical resistivity, attention should be paid on cations exhibiting multivalent character. The room temperature resistivity of ferrites can vary between 10^{-2} to higher than 10^{11} ohm-cm, depending on the chemical composition, microstructure and firing conditions. It has long been known that ferrites have low resistivities due to the simultaneous presence of ferrous and ferric ions on equivalent lattice sites, particularly in the octahedral sublattice [21, 22].

A number of processing techniques may be needed to control the Fe^{2+} formation. Resistivity can be increased to higher than 10^{6} ohm-cm when ferrite is produced iron deficient and sintered in a sufficiently oxidizing atmosphere yielding no ferrous ions in the structure [21]. Moreover cooling rate of the furnace during production plays an important role in Fe^{2+} cation production. At high temperatures Fe^{2+} is favored and is quenched in the structure when it is rapidly cooled. During slow cooling however, reoxidation can occur. This lowers Fe^{2+} content and hence restricts the opportunity for electron hoping [22]. In addition, if rate of cooling is arranged, grain boundaries oxidize preferentially due to higher oxygen diffusivity along them. The resulting structure is the semiconducting grains surrounded by highly resistive grain boundaries as shown in Figure 2.10.

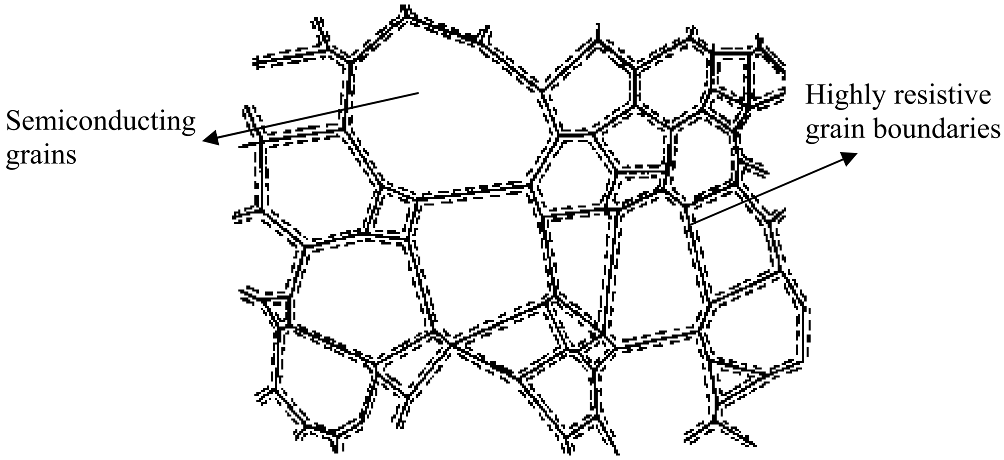

Figure 2.10 Schematic diagram of a ferrite with semiconducting grains surrounded by insulating grain boundaries [22].

Due to their high resistivity, existence of grain boundaries plays an important role and so does their fraction within the structure. According to a model developed by Mendelson [27] on the assumption of log-normal grain size distribution for a ceramic consisting of tetrakaidecahedral grains as shown in Figure 2.11, grain boundary surface area per unit volume, S_V, is inversely proportional to the average grain size, $\overline{D}$, in relation to:

$$S_V = \frac{7.1025}{\overline{D}}(\exp - 2.5\ln^2\sigma) \tag{2.9}$$

where lnσ is the standard deviation of the log-normal distribution. If volume fraction of grain boundaries in a fully dense ceramic is in proportion to the S_V, it can be concluded that resistivity of ferrites decreases as the grain size increases.

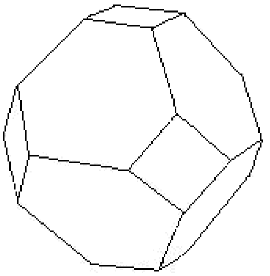

Figure 2.11 A tetrakaidecahedral grain.

2.11 Compositional Modifications and Previous Studies on Nickel Ferrite

Uitert [28] studied the effects of minor manganese and cobalt additions on the DC-resistivity of nickel ferrite compositions. In his study samples were sintered by soaking at 1200, 1250, 1300, and 1350 ºC for 10 h. He showed that DC-resistivity of the nickel ferrite increased from 10^4 ohm-cm to 10^{10} ohm-cm for $NiFe_{1.9}Mn_{0.02}O_4$ and to 10^{11} ohm-cm for $NiFe_{1.9}Co_{0.02}O_4$ when sintered at 1250 ºC. The increase was attributed to the replacement of conduction mechanisms Fe^{2+}-Fe^{3+} and/or Ni^{2+}- Ni^{3+} by more difficult ones.

Smit and Wijn [21] noted that nickel ferrite attained resistivity greater than 10^{10} ohm-cm with iron deficiency and replacement of iron with small portions of cobalt.

Lupeiko et al. [29] selected the ferrite composition of $NiCo_{0.02}Fe_{1.9}O_{4-\delta}$, as the magnetostrictive constituent in the production of ME ceramic composites, due to its high resistivity and magnetostriction. They stated that Co addition was assigned to increase magnetostrictive parameters by compensating magnetoscrystalline anisotropy. Small amount of copper oxide was added into the composition in order to decrease sintering temperature and to improve the magnetostrictive parameters. Also, iron was partly replaced by manganese for higher resistivity. The composite comprised of the ferrite phase with the composition $NiCo_{0.02}Cu_{0.02}Mn_{0.10}Fe_{1.8}O_{4-\delta}$ showed the highest ME performance.

In general, ferrite ceramics have low density especially when sintered at low temperatures and for short durations. In order to improve the densification behavior of ferrites, researchers used sintering aids, one of which was Bi_2O_3. Kumar et al. [30] studied the effect of Bi_2O_3 addition on electrical and magnetic properties of $Ni_{0.8}Zn_{0.2}Fe_2O_4$. Ferrites, modified by 1, 2, 4, and 6 wt% Bi_2O_3, were soaked at 1100 ºC for 10 h. Their results are listed in Table 2.4. As revealed from the table, the average grain size of the ferrites increased and porosity decreased with bismuth concentration. The resistivity of the samples increased two orders of magnitude for 1 wt% Bi_2O_3 addition. The improvement was attributed to the presence of high resistive Bi_2O_3 at the grain boundaries. Initial magnetic permeability of the samples attained twice the value of the bismuth free samples when 1 wt% Bi_2O_3 was added. The reason of this improvement was the increased grain size and hereby contribution of the domain wall motion to the permeability. Further additions led to a decline in μ_i due to the existence of excess non-magnetic phase at the grain boundaries.

Table 2.4 Average grain size, porosity, room temperature electrical resistivity and initial magnetic permeability (at 5 MHz) of $Ni_{0.8}Zn_{0.2}Fe_2O_4$ with different Bi_2O_3 concentrations [30].

Sample	**B0**	**B1**	**B2**	**B4**	**B6**
Bi_2O_3 doping (wt%)	0	1	2	4	6
Average grain size (μm)	~0.3	~3	~3	~3	~3
Porosity (%)	13	9.7	6.5	5.8	5.4
Resistivity (ohm-cm)	3.5×10^6	6.7×10^8	5.2×10^8	4×10^8	3.5×10^8
Initial magnetic permeability	37	75	70	64	48

Mürbe and Töpfer [31] studied the effect of Bi_2O_3 addition on the microstructure and permeability of Ni-Cu-Zn ferrite. Samples were soaked at 900 ºC in the presence of 0.25, 0.375, 0.5, 0.75, and 1 wt% Bi_2O_3. The grain size of the sintered samples increased slightly with 0.25 wt% Bi_2O_3 when compared to bismuth free samples. A bimodal grain growth was observed for the samples having 0.3- 0.5 wt% Bi_2O_3, in which small grains with the size of 1 μm were located in regions between large grains of 20-30 μm size. When Bi_2O_3 concentration exceeded 0.5 wt%, ceramics attained a homogeneous structure with coarse grains. The permeability increased for small Bi_2O_3 concentrations, but decreased when the Bi_2O_3 content was more than 0.5 wt%. Higher permeabilities were attributed to the increase in grain size.

2.12 Magnetoelectric (ME) Effect

Magnetoelectric (ME) effect is an induced dielectric polarization of a material under the applied magnetic field, $(ME)_H$, and/or an induced magnetization under an external electric field, $(ME)_E$ [4]. This effect makes the conversion of electric energy into magnetic energy, or vice versa, possible [4, 32, 33]. The important parameter in the ME effect is the magnetoelectric voltage coefficient, α_E, which can be expressed as

$$\alpha_E = \frac{\partial E}{\partial H} = \frac{\text{output voltage}/\text{thickness}}{\text{a.c. magnetic field}} \qquad (2.10)$$

where E and H are the electric and magnetic fields, respectively [5]. ME coefficient, α, on the other hand, is equal to $\alpha = \varepsilon_o \cdot \varepsilon_r \cdot \alpha_E$ where ε_o and ε_r are permittivity of vacuum and relative permittivity, respectively [33].

The historical development of ME composites were reviewed in two separate papers published by Suryanarayana [2] and Ryu et al. [5]. According to the information provided in these papers, ME effect was found first by Curie in 1894. Curie pointed out that a body with asymmetric molecules gets electrically polarized when placed in a magnetic field according to the symmetry conditions. In 1957, Landau and Lifshitz concluded that ME effect can principally exit in magnetically ordered crystals. In 1960, Dzyaloshinskii theoretically predicted the existence of ME effect in antiferromagnetic Cr_2O_3. This prediction was experimentally confirmed by Astrov, in 1960, and by Rado and Folen, in 1961.

The ME phenomenon has been observed in several single phase materials and composites. Single phase materials exhibiting this property have a simultaneous electric and magnetic ordering in their structure. They show combination properties of ferroelectricity and antiferroelectricity with ferromagnetism, ferrimagnetism and antiferromagnetism [2]. ME effect has been reported in single-phase materials having perovskite structure, rare earth manganates, $BaMF_4$ (M= Mn, Fe, Co, Ni), and inverted spinels [34]. Later, this effect was observed in $BiFeO_3$ and in boracites [5].

The magnitude of ME voltage coefficient of the single phase materials are quite low, in the range of 1 to 20 mV/cm·Oe. For example, best single phase material is Cr_2O_3 with ME voltage coefficient of 20 mV/cm·Oe [35]. Moreover, single phase materials have low Curie or Neel points so they can operate only at low temperatures [4, 5]. These problems were solved with the development of composites.

ME composites are composed of piezoelectric and magnetostrictive constituent phases and show this effect by making use of the product property which was proposed by Van Suchtelen in 1972 [36]. The product property states that if one phase in a composite exhibits a property A→B and the second phase exhibits a property B→C, then the composite will have the property A→C, which is absent in both of the individual phases. Based on these statements, in an ME composite, an applied magnetic field would induce strain in the magnetostrictive phase, which, in turn, produces a stress on the piezoelectric phase giving rise to voltage outputs [2, 4]. ME effect is absent in either of the constituent phases. Product property in ME composites can be formulated as follows [3]

$$\text{ME Effect} = \left(\frac{\text{mechanical}}{\text{magnetic}}\right) * \left(\frac{\text{electrical}}{\text{mechanical}}\right)$$

$$\text{ME Effect} = \left(\frac{\text{strain induced}}{\text{magnetic field}}\right)_{\text{ferrite}} * \left(\frac{\text{electric voltage}}{\text{stress induced}}\right)_{\text{ferroelectric}}$$

In order to obtain higher ME outputs from the composites, conceptual points outlined by Boomgaard were as follows [35]

i. Two individual phases must be in equilibrium.
ii. Mechanical contact between grains should be perfect.
iii. The magnitude of the piezoelectric coefficient of the piezoelectric phase and the magnitude of the magnetostriction coefficient of the magnetostrictive (piezomagnetic) phase must be high.
iv. The accumulated charges must not leak through the magnetostrictive (piezomagnetic) phase. This phenomenon necessitates higher resistivity values.
v. Proper poling strategy should be determined.

2.13 Types of ME Composites

There are mainly three types of ME composites: in situ grown composites, bulk (or particulate) composites, and laminated (or layered) composites.

In situ grown composites were produced by Boomgaard et al. [37] through the unidirectional solidification of a eutectic melt in a Fe-Co-Ti-Ba-O quinary system, which resulted in a structure having aligned piezoelectric and magnetostrictive phases. The well defined crystal orientation of the two phases with respect to the growth direction and with respect to each other was the major advantage of these two phase composites [38]. The problems associated in the production of in situ grown ME composites were the complicated reaction kinetics, thermodynamic constraints and all kinds of possible random diffusions [39].

Preparation of bulk composites is much easier and cheaper when compared to unidirectional solidification. Bulk composites offer free choice of mole ratio of constituent phases and sintering temperatures and independent choice of grain size of each phase. Moreover, the existence of eutectic point or a eutectoid phase is not a prerequisite for them [35]. The procedure in the production of bulk composites included mixing the powders of constituents thoroughly in different portions and sintering the mixture at different temperatures [7, 40-42]. In the previous studies on bulk ME composites [5, 32, 43], it was stated that one of the problems in this type of composites was the possible chemical reactions that could take place between the constituents. Another problem was the low resistivity of the magnetostrictive phase or induced eddy currents in the conducting phase under the applied ac field, which resulted in charge leakage and consequently difficulties in poling treatment for maximum piezoelectric activity. Moreover existence of mechanical defects had a detrimental effect on ME outputs.

The bulk and in situ ME composites showed higher ME outputs when compared to single phase materials, however they still have problems in reliability and reproducibility. The problems encountered during the preparation of these composites may be overcome by laminated composites. Laminated composites manufactured in the study of Ryu and coworkers [5, 44] had a very simple structure and relatively easy fabrication method. Component ceramics were prepared separately and composites were produced by stacking and bonding a piezoelectric ceramic between two magnetostrictive discs with silver epoxy. This method prevented the possible chemical reactions and dispersions between the constituent phases.

Another way of laminated composite production was shown in the work of Srinivasan et al. [33]. Magnetostrictive and piezoelectric layers (tapes) were separately fabricated through doctor blade technique. Multilayer composites were obtained by laminating *n* layers of piezoelectric tapes with *n+1* layers of magnetostrictive tapes under high pressure and temperature followed by sintering at specific temperatures.

2.14 Previous Studies on ME Composites

So far, in the production of ME composites various compositions including Ni(Co,Mn)Fe_2O_4–$BaTiO_3$, $CoFe_2O_4$–$BaTiO_3$, $CoFe_2O_4$–PZT, $NiFe_2O_4$–PZT, Terfenol-D–PZT, Terfenol-D–PMN-PT and $CuFe_2O_4$–$BaTiO_3$ have been reported in the literature. The results obtained in some of these studies are given in Table 2.5.

Boomgaard and Born [35] studied bulk ME composites comprising $BaTiO_3$ and $Ni_{0.97}Co_{0.03}Mn_{0.1}Fe_{1.9}O_4$ as the piezoelectric and the magnetostrictive phases, respectively. Maximum ME output was detected, from the composite having 60 mol% ferrite, as 80 mV/cm˙Oe. In their study, effects of crystallite size, composition, excess TiO_2, cooling rate after sintering, and poling procedure on the ME conversion were also evaluated. They concluded that small fluctuations in these parameters would have significant influence in the ME conversion.

Ryu et al. [44] studied the ME effect on the laminated composites that were manufactured by stacking and bonding a PZT4 disc between two magnetostrictive Terfenol-D discs. The observed ME output was 5.90 V/cm˙Oe. This high value was assigned to the high piezoelectric voltage coefficient of the piezoelectric phase, optimum thickness ratio between PZT and Terfenol-D discs, and magnetostriction being along the radial direction in Terfenol-D discs.

Srinivasan et al. [45] studied ME effect in $CoFe_2O_4$–PZT, $NiFe_2O_4$–PZT and manganite–PZT laminated composites. $CoFe_2O_4$ was selected as the magnetostrictive phase due to its high magnetostriction coefficient. Despite this advantage, however, ME output was lower than that of $NiFe_2O_4$–PZT composite. This was attributed to the poor ME coupling between two constituent phases. They noted that magnetomechanical coupling were controlled by magnetization mechanisms such as domain rotation and domain wall movement, which are favored by low anisotropy. Therefore they pointed out that due to its low anisotropy and high initial magnetic permeability soft ferrite $NiFe_2O_4$ would be a good candidate in the production of ME composites.

Table 2.5 Various types of ME composites with different compositions.
The symbols are: $T_{sintering}$: sintering temperature, $t_{sintering}$: sintering time, α_E: magnetoelectric voltage coefficient.

Authors	**Type of Composite**	**Magnetostrictive Powder** **Piezoelectric Powder**	$\mathbf{T_{sintering}}$ $\mathbf{t_{sintering}}$	$\boldsymbol{\alpha_E}$
Srinavasan et al., 2001 [33]	Laminated Composite (doctor blade technique)	$NiFe_2O_4$ PZT5	1127-1227 °C	1500 mV/cm·Oe
Srinavasan et al., 2004 [45]	Laminated Composite (doctor blade technique)	$CoFe_2O_4$ PZT	927-1227 °C	55 mV/cm·Oe
Ryu et al., 2001 [44]	Laminated Composite (stacking and bonding)	Terfenol-D PZT4		5.90 V/cm·Oe
Ryu et al., 2002 [46]	Laminated Composite (stacking and bonding)	Terfenol-D PMN-PT single crystal		10.30 V/cm·Oe
Boomgard et al., 1974 [37]	In situ Grown Composite	Fe_2O_3-CoO-TiO_2-BaO quinary system		130 mV/cm·Oe
Mazumder et al., 2003 [39]	In situ Grown Composite	Fe_2O_3-CoO-TiO_2-BaO quinary system	1000-1200 °C 3 h	3-5.59 mV/cm·Oe
Patankar et al., 2001 [47]	Bulk Composite	$xCuFe_2O_4$ $(1-x)Ba_{0.8}Pb_{0.2}TiO_3$	950 °C 1.5 h	230 µV/cm·Oe at x=30 mol%

Table 2.5 (Continued)

Authors	**Type of Composite**	**Magnetostrictive Powder** **Piezoelectric Powder**	**$T_{sintering}$** **$t_{sintering}$**	**α_E**
Ryu et al., 2001 [40]	Bulk Composite	xNiCo$_{0.02}$Cu$_{0.02}$Mn$_{0.1}$Fe$_{1.8}$O$_{4-k}$ $(1-x)$PZT4	1100-1300 °C 2 h	115 mV/cm·Oe at x=20 wt%
Mahajan et al., 2002 [48]	Bulk Composite	xCoFe$_2$O$_4$ $(1-x)$BaTiO$_3$	1200 °C 12 h	140 µV/cm·Oe at x=25 mol%
Patankar et al., 2003 [41]	Bulk Composite	xNi$_{0.25}$Co$_{0.75}$Fe$_2$O$_4$ $(1-x)$Ba$_{0.8}$Pb$_{0.2}$TiO$_3$	1100 °C 24 h	420 µV/cm·Oe at x=15 mol%
Zhai et al., 2004 [32]	Bulk Composite	xNiFe$_2$O$_4$ $(1-x)$PbZr$_{0.57}$Ti$_{0.43}$O$_3$	1150 °C 2 h	80 mV/cm·Oe at x=32 vol%
Kulkarni et al., 2005 [7]	Bulk Composite	xNi$_{0.8}$Co$_{0.1}$Cu$_{0.1}$Fe$_2$O$_4$ $(1-x)$PbZr$_{0.8}$Ti$_{0.2}$O$_3$	1000 °C 12 h	375 µV/cm·Oe at x=25 mol%
Li et al., 2006 [4]	Bulk Composite	$(1-x)$Ni$_{0.8}$Zn$_{0.2}$Fe$_2$O$_4$ xSr$_{0.5}$Ba$_{0.5}$Nb$_2$O$_6$	1200-1275 °C 3 h	26.6 mV/cm·Oe at x=70 mol%
Chougule et al., 2007 [42]	Bulk Composite	xNi$_{0.8}$Zn$_{0.2}$Fe$_2$O$_4$ $(1-x)$PbZr$_{0.52}$Ti$_{0.48}$O$_3$	1200 °C 5 h	769 µV/cm·Oe at x=15 mol%

CHAPTER 3

EXPERIMENTAL PROCEDURE

3.1 General

In the present study, the piezoelectric and magnetostrictive ceramic powders were prepared in the laboratory by using the mixed oxide technique. Ceramics were manufactured by pressing the powders into compacts of various shapes (thin discs for piezoelectric samples, discs and toroids for magnetostrictive samples) and then sintering the compacts with an appropriate heating schedule. Piezoelectric ceramics were electroded and then poled for dielectric and piezoelectric characterization. Disc type magnetostrictive ceramics were used for measurement of electrical properties. Toroids of magnetostrictive ceramics were used for magnetic characterization. Phase and microstructural analysis of the powders and sintered ceramics were done by using X-ray diffraction (XRD) and Scanning Electron Microscope (SEM) analyses.

ME composites were manufactured from powders as well as sintered discs of magnetostrictive and piezoelectric constituents. The performance of the bulk and laminated composites were evaluated in terms of voltage generated by the composite in response to the applied magnetic field.

3.2 Details

3.2.1 Chemical Compositions of Ceramic Powders

In the literature, numerous piezoelectric and magnetostrictive ceramics have been reported with varying chemical compositions for use as the components of ME ceramic composites. In the present study, the following specific compositions were selected to produce ME composites:

Piezoelectric ceramic: $Pb_{0.95}Sr_{0.05}(Zr_{0.53}Ti_{0.47})O_3$+1wt%$Bi_2O_3$+0.4mol%(=0.11wt%)MnO
Magnetostrictive ceramic: $NiCo_{0.02}Cu_{0.02}Mn_{0.10}Fe_{1.8}O_{4-k}$

The piezoelectric ceramic composition was developed by Çağatay [17] who studied the modification of hard piezoelectric ceramics by selected dopants. It was shown that these dopants could be effective in combining the soft and hard properties of PZT.

Composition for the magnetostrictive ceramic was essentially the same as that of the ferrite phase used in the work of Lupeiko et al. [29]. They noted that iron deficient nickel ferrite doped by a combination of cobalt, copper and manganese had superior magnetic and electrical properties.

Throughout the remaining part of this thesis, the piezoelectric and magnetostictive compositions described hereby have been abbreviated simply as **PSZT** and **NF**, respectively.

3.2.2 Synthesis of Ceramic Powders

Powders of the ceramics having chemical compositions mentioned above were prepared by using conventional mixed oxide technique. This technique is essentially the thermal synthesis of the ceramic compound in question achieved by reacting an intimate mixture of constituent oxides at high temperatures. In the ceramic literature, development of phases with the action of heat from the precursors is referred to as the ‘calcination process’.

3.2.2.1 Piezoelectric Powder

Raw materials used in this study for the preparation of the doped lead zirconate titanate (PSZT) powder are listed below:

PbO: Merck 5658 PbO Powder
ZrO_2: SEPR ZrO_2 Powder
TiO_2: Merck 808 TiO_2 Powder
$SrCO_3$: Merck 6393 $SrCO_3$ Powder

All of these powders were finer than 10 μm and each had a certified purity in excess of 99.5 wt%. Prior to their use, powders were heated at 200 °C for 3 h to remove possible adsorbed moisture.

Summary of the procedure used in PSZT powder preparation is shown in the flow chart given in Figure 3.1. Powders of raw materials were weighed in appropriate quantities for a total of a 30 g PSZT batch, in accordance with the stoichiometric composition of $Pb_{0.95}Sr_{0.05}(Zr_{0.53}Ti_{0.47})O_3$. They were then blended thoroughly in an agate mortar by a grinding action under ethanol for 1.5 h. The slurry was left to dry in air. The dry mixture was then pressed into a cake in a 32 mm stainless steel die. The cake was placed on an alumina plate and heated to 825 °C in a muffle furnace where it was soaked for 5 h. This was the first calcination step of the powder preparation. The calcined cake was crushed in the mortar and sieved through a 150 μm plastic screen. Next, powders were placed in a plastic jar loaded with yttria stabilized zirconia (YSZ) balls and ball milled in ethanol for 4 h. The slurry was left to dry and then heated to 600 °C for the removal of plastics that was picked up from the jar during ball milling. These powders were compacted again in the stainless steel die for the second calcination. This step, conducted at 860 °C for 2 h, was basically a homogenization treatment.

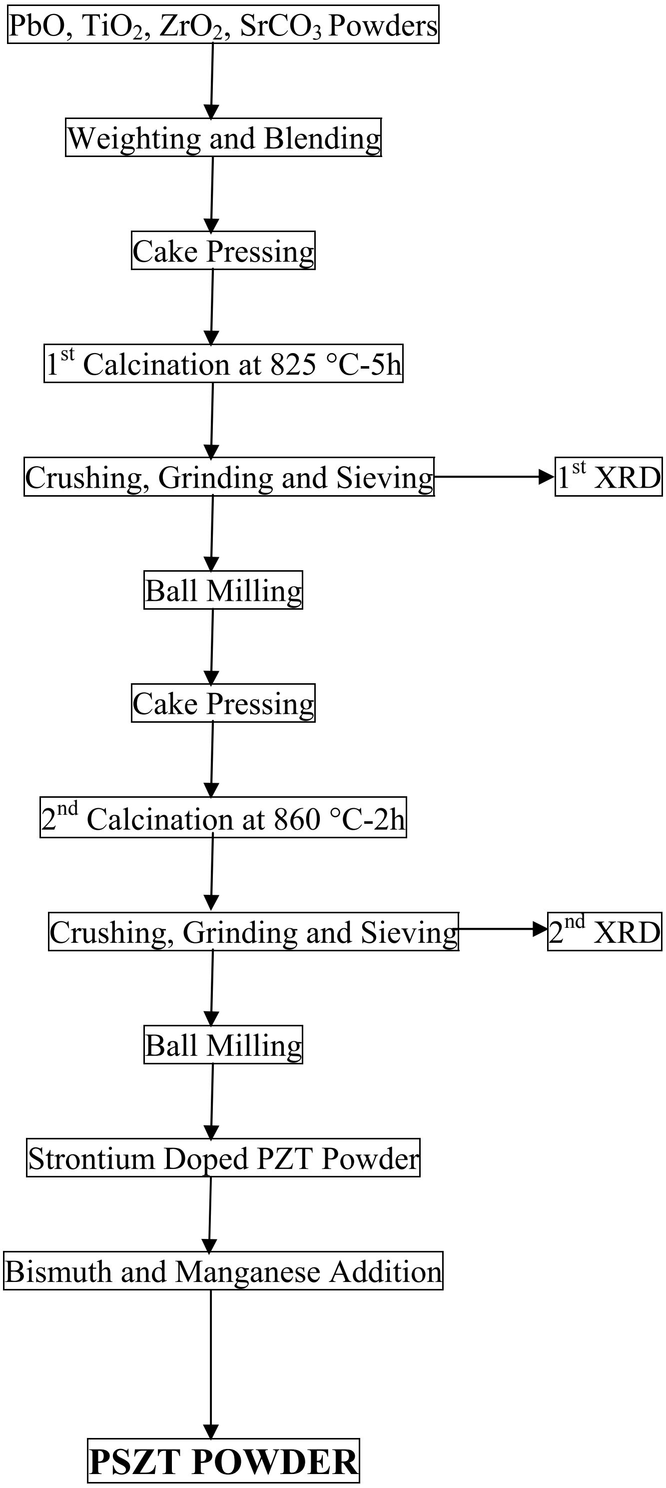

Figure 3.1 Flow chart of the PSZT powder preparation.

The final cake was again crushed in the mortar and sieved through a 150 µm plastic screen. Next, it was ball milled in a plastic jar with YSZ balls in ethanol for 14 h. Dried slurry was again heated to 600 °C for the removal of plastics. This procedure gave the basic strontium doped PZT powder.

During powder production, after each calcination step, powders were analyzed by XRD for phase determination. As revealed by the XRD patterns, shown in Figures 3.2 and 3.3, single phase perovskite structure was obtained even after the first calcination. The milled powders were predominantly sub-micron in size as seen in the SEM image in Figure 3.4.

The modification of the base Sr doped PZT powder with Bi and Mn was done by adding Bi^{3+} and Mn^{2+} ions from their aqueous nitrate solutions. For this purpose, Bi_2O_3 powder (Merck 1889) was dissolved in analar nitric acid (Merck 1518) in the stoichiometric quantity giving 100 mg Bi^{3+} cations per milliliter solution, and manganese nitrate (Merck 5940) was dissolved in deionized water yielding a solution of 5 mg Mn^{2+} cations per milliliter. Both nitrate solutions were acidified slightly with nitric acid, HNO_3, to keep all Bi and Mn in the dissolved state. Effective distribution of the dopants in the PZT powder was ensured by dilution of the powder with alcohol during cation addition. Doped powder was heated in an alumina crucible to 400 °C and kept at this temperature for 4 h for the decomposition of nitrates and removal of the NO_x. This procedure gave the **PSZT** powder used in ceramic manufacture.

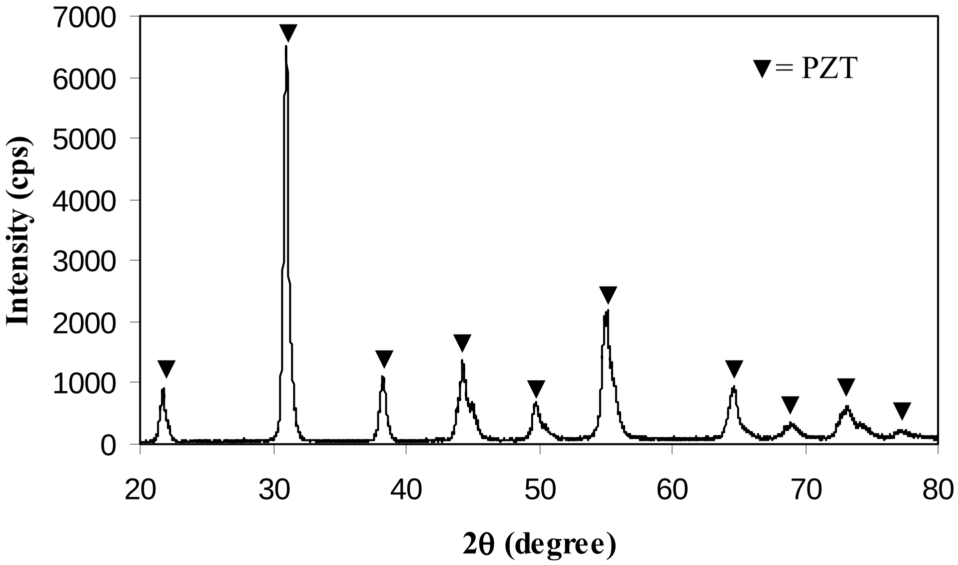

Figure 3.2 XRD pattern of strontium doped PZT powder after first calcination.

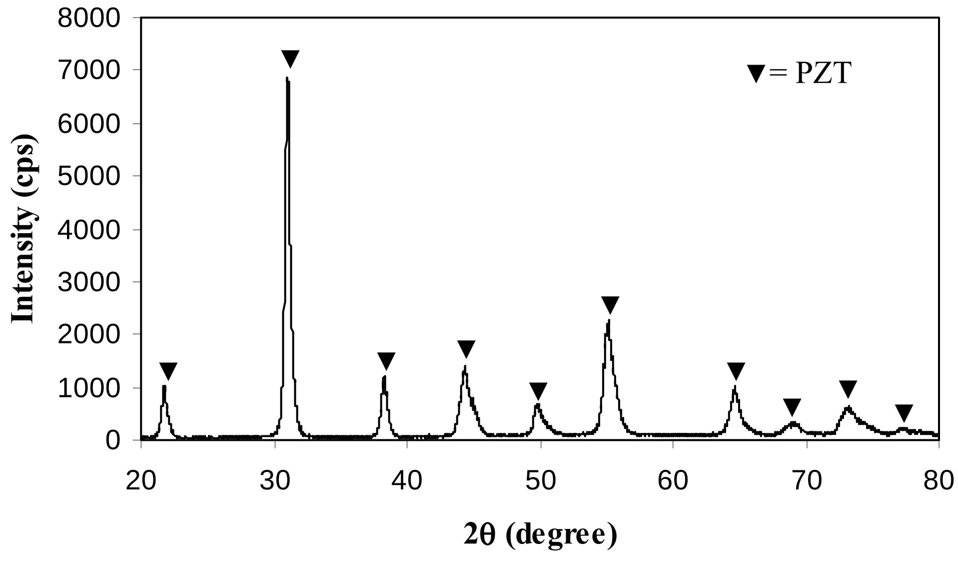

Figure 3.3 XRD pattern of strontium doped PZT powder after second calcination.

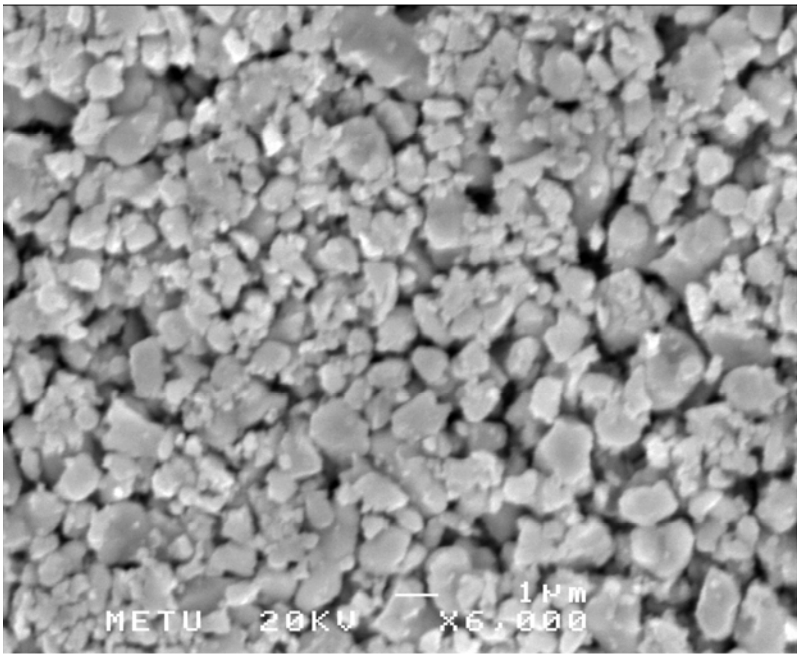

Figure 3.4 SEM image of strontium doped PZT powder after final ball milling. Powder was packed with a small amount of binder.

3.2.2.2 Magnetostrictive Powder

Raw materials used for the preparation of the doped nickel ferrite (NF) powder are as follows:

Ni_2O_3:	Merck 6723 Ni_2O_3 Powder
Fe_2O_3:	Merck 3924 Fe_2O_3 Powder
$MnCO_3$:	STREM $MnCO_3$ Powder

Powders listed above had certified purity in excess of 99.8 wt%.

Prior to synthesis of the NF powder, black Ni_2O_3 was heated in a platinum crucible at 1030 ºC and kept there for 6 h in order to convert all Ni^{3+} cations into Ni^{2+} state. This process yielded the green NiO powder. As received Fe_2O_3 powder was heated in an alumina crucible to 200 °C for 3 h to remove any adsorbed water.

The procedure followed in NF powder synthesis is shown in the flow chart given in Figure 3.5. The powders of NiO, Fe_2O_3 and $MnCO_3$ were weighed in appropriate quantities for a total of a 40 g batch in accordance with the stoichiometric composition $NiCo_{0.02}Cu_{0.02}Mn_{0.10}Fe_{1.8}O_{4-k}$. The batch was blended thoroughly in an agate mortar by a grinding action under ethanol for 1.5 h. After drying in air, mixture was pressed into cakes in the stainless steel die. Cakes were calcined twice in a muffle furnace in order to obtain single phase spinel structure. First calcination was conducted in two steps: soaking at 900 °C for 4 h followed by soaking at 1100 ºC for 10 h. Calcined cakes were crushed and ground to a fine state in a porcelain mortar and pestle. XRD pattern of the product after first calcination revealed traces of unreacted Fe_2O_3 as seen in Figure 3.6.

Cobalt and copper addition were made prior to second calcination. Due to relatively small concentrations of these dopants, addition was done from aqueous nitrate solutions. For this purpose cobalt (II) nitrate hexahydrate salt, $Co(NO_3)_2.6H_2O$, (Merck 2536) was dissolved in deionized water forming a solution with 50 mg Co^{2+} cations per milliliter. Similarly, a nitrate solution of copper with a concentration of 100 mg Cu^{2+} per milliliter was prepared by dissolving copper (II) oxide (Merck 2761) in analar nitric acid. Both nitrate solutions were acidified slightly to keep all Co and Cu in the dissolved state. Homogeneous distribution of the dopants in the ferrite powder was ensured by dilution with ethanol. Doped powder was heated to 400 °C and kept there for 4 h for the decomposition of nitrates and removal of NO_x.

For the second calcination, ferrite powder modified by Co and Cu was compacted again after adding few milliliters of polyethylene glycol (PEG 6000) as a binder. Cakes were kept at 50 ºC overnight for drying. Second calcination was conducted in two steps: soaking at 900 °C for 3 h followed by soaking at 1100 ºC for 3 h. As shown in the XRD pattern in Figure 3.7, small amount of Fe_2O_3 was still present in the product even after this stage. An additional heat treatment, conducted at 1100 ºC for 3 h, yielded phase pure spinel, as seen in the XRD pattern of the powder in Figure 3.8.

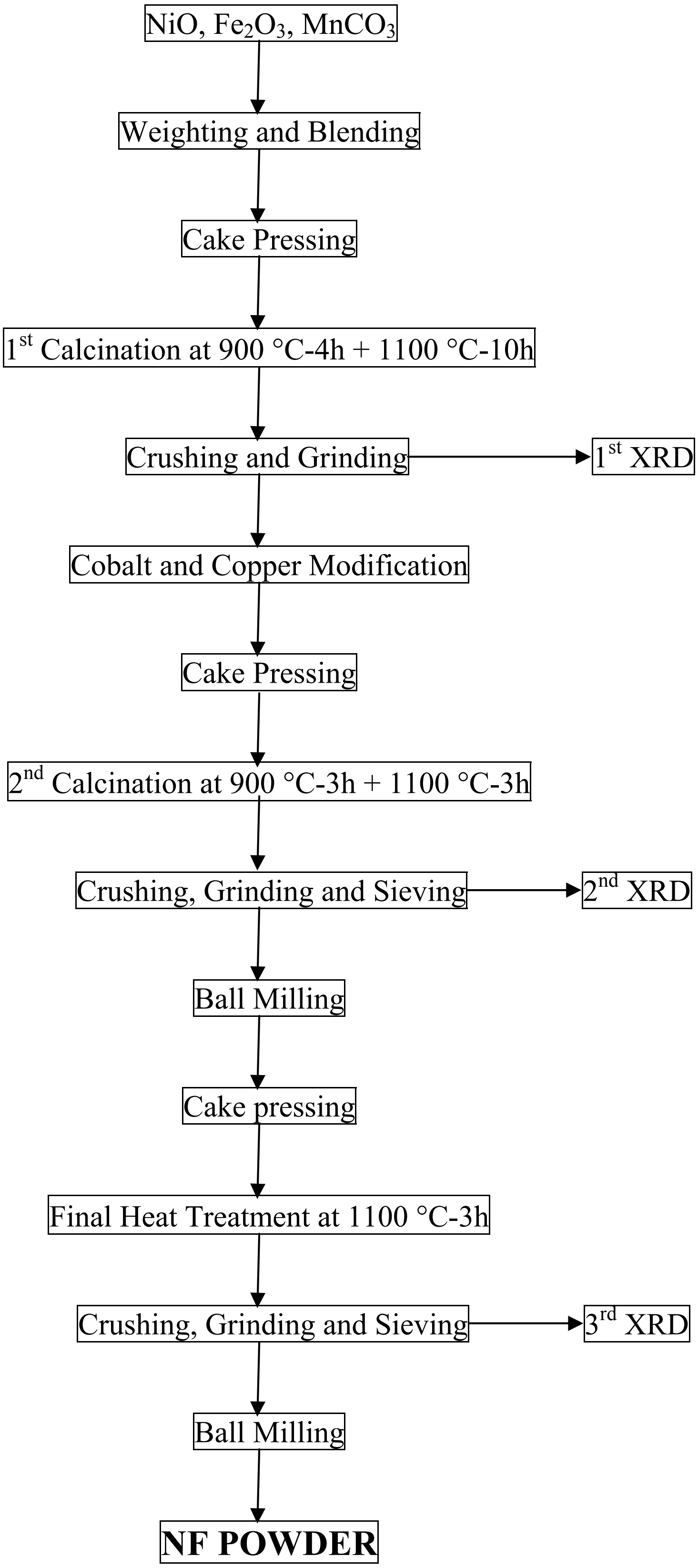

Figure 3.5 Flow chart of the NF powder preparation.

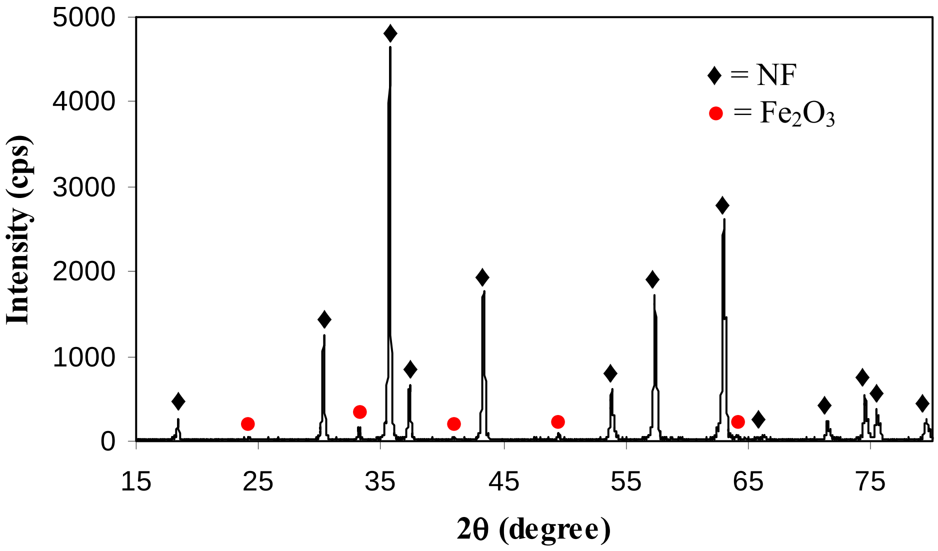

Figure 3.6 XRD pattern of NF powder after first calcination.

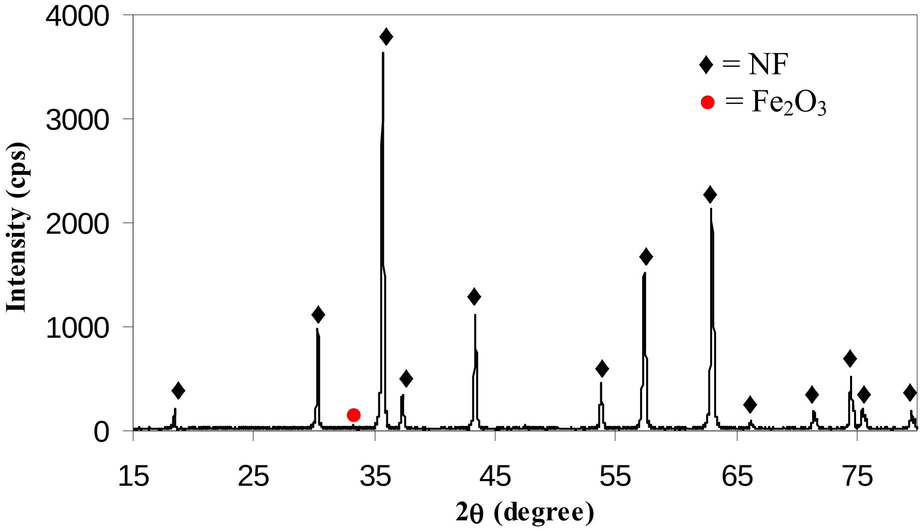

Figure 3.7 XRD pattern of NF powder after second calcination.

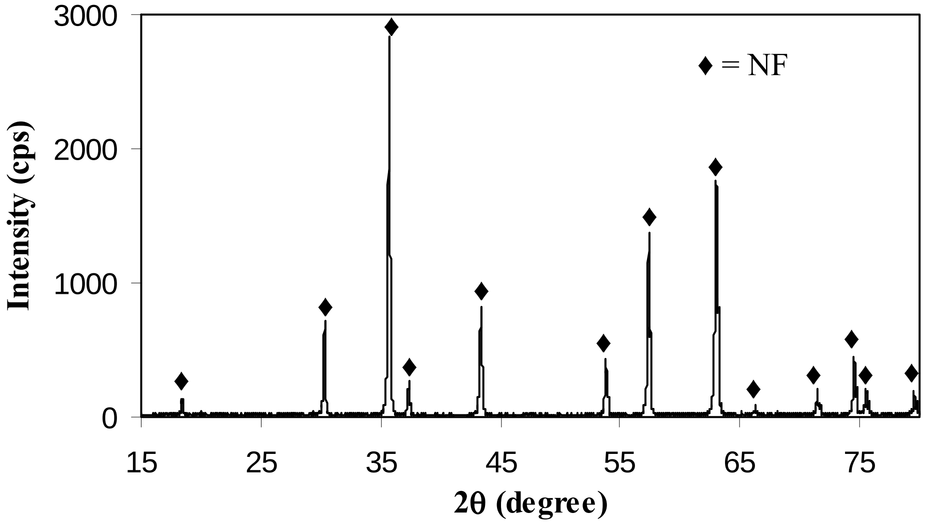

Figure 3.8 XRD pattern of NF powder after final heat treatment.

The communition steps shown in Figure 3.5 comprised a combination of crushing, grinding, sieving and ball milling actions. The duration for ball milling was 6 h in second stage calcination, and 16 h after final heat treatment. Milled powder was dried in oven at 70 ºC. After drying, powder was heated to 600 ºC in an alumina crucible for the removal of plastics. SEM image of the powder, shown in Figure 3.9, revealed that average particle size was about 1 µm.

The ferrite powder synthesized by the procedure described above exhibited rather poor sintering characteristics, as will be mentioned later in Chapter 4. In order to enhance sinterability, small quantities of Bi_2O_3 were introduced into the base NF powder. Bismuth additions were made through the use of the nitrate salt solution prepared earlier for the treatment of the PZT powder.

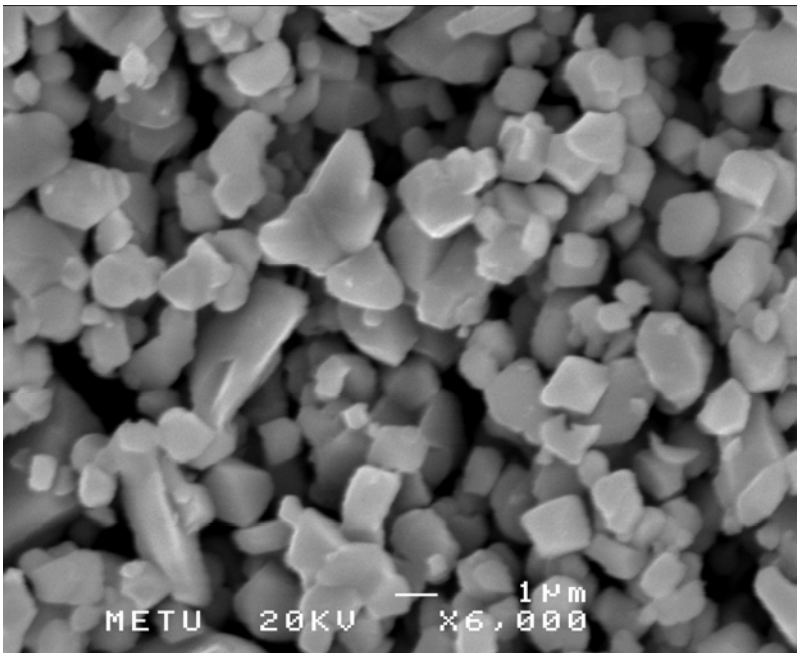

Figure 3.9 SEM image of NF powder after final ball milling. Powder was packed with a small amount of binder.

3.2.3 Preparation of Ceramic Samples

The piezoelectric and magnetostrictive ceramics used throughout this thesis were manufactured in the form of thin sintered circular discs for dielectric, piezoelectric and electrical measurements. Toroids of magnetostrictive ceramics were prepared for magnetic characterization.

In order to produce piezoelectric discs, first the PSZT powder was mixed with 3 wt% PEG 6000 which served as the binder and the plasticizer. Plasticized powder was sieved through a 150 µm plastic screen in order to avoid agglomeration of the granules. Green ceramic discs were obtained by pressing the granules uniaxially in a stainless steel die under 100 MPa. The discs were 13 mm in diameter and 1.5 mm in thickness. Three discs were prepared for each sintering experiment.

NF discs were produced through a similar process. Green ceramic discs were 13 mm in diameter and 3.5 mm in thickness. The toroidal ferrites were obtained by pressing the NF granules in a special hollow die. The dimensions of the green toroids were 20.4 mm in outer diameter, 8.5 mm in inner diameter and 5 mm in thickness. A set consisting of two discs and one toroid were prepared for each sintering experiment.

Sintering studies were conducted in a muffle furnace heated by SiC elements. The furnace was equipped with a Honeywell UDC-2000 temperature monitoring unit which permitted to execute heat treatment schedules comprising up to twelve individual stages.

All ferrite ceramics were sintered in air atmosphere. For this purpose, the green discs and toroids were placed on ceramic setters, inserted into the muffle and then heated to the peak firing temperature at a rate of 4 ºC per min. The selected soak temperatures were 1150, 1175, 1200, 1225, and 1250 ºC. The soak duration was fixed as 2 h. Upon completion of the soak stage, the sintered ceramics were cooled to room temperature at a rate of 4 ºC per min. The sintering schedule included an intermediate hold at 600 ºC for 30 min in order to allow removal of binder. The setters were sintered plates of ferrite manufactured from the NF powder in the form of thin rectangular plates.

Sintering of PSZT discs required special attention due to the increased vaporization tendency of the PbO component at elevated temperatures. Although the sintering schedule and soak temperatures were very much the same as described for the ferrite ceramics, care was taken to depress volatilization of lead during sintering. This was accomplished by using the specially designed enclosure depicted in Figure 3.10. The sintering assembly consisted of the PZT saggars containing the green piezoelectric ceramic discs and PZT chunks so that an atmosphere rich in PbO was generated in the space covered by the inverted and sealed aluminum crucible. The saggar and the chunk were made from PZT having the same composition of the piezoelectric discs. The enclosure described was effective in minimizing the PbO loss from piezoelectric discs; weight measurements indicated that the loss was confined to less than 0.3 wt% at the highest sintering temperature of 1250 ºC.

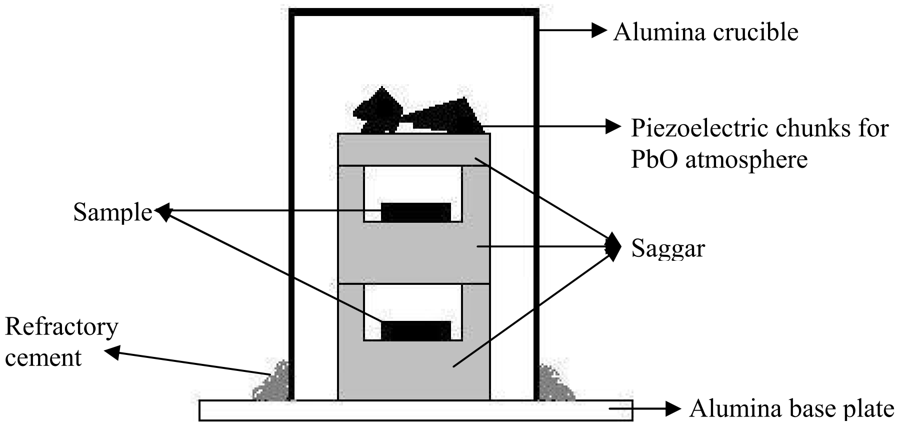

Figure 3.10 Saggar configuration used for sintering of PSZT ceramics.

The procedure followed in the sintering PSZT ceramics involved a binder removal in air at 600 ºC for 30 min before placing the discs in the sintering enclosure. During the ramp stage, the firing schedule had a hold step at 860 ºC for 30 min as suggested by Saha and Agrawal [49].

The appearance of PSZT and NF ceramics manufactured for measurements are shown in Figures 3.11 and 3.12, respectively.

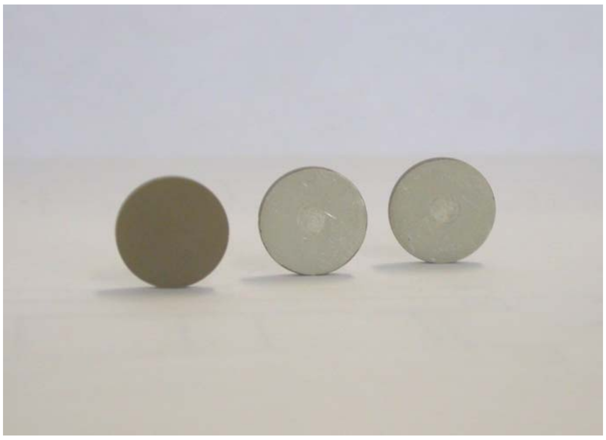

Figure 3.11 PSZT samples prepared for measurements.

Figure 3.12 NF samples prepared for measurements.

3.2.4 Preparation of ME Composites

In the present study, two different types of ME composites were manufactured: bulk composites and laminated composites. The former was produced by sintering the mixture of piezoelectric and magnetostrictive powders in the form of thin discs whereas the latter was prepared by mechanically bonding the sintered piezoelectric and magnetostrictive disc ceramics. Details of both manufacturing processes are provided in the following parts.

3.2.4.1 Preparation of Bulk ME Composites

For composite production, powder mixtures were prepared by blending 10, 15, and 20 wt% NF powder with 90, 85, and 80 wt% PSZT powder, respectively. Mixing was conducted in a plastic jar with YSZ balls in ethanol for effective distribution of NF powder in PSZT matrix. Slurry was then left to dry in air. Composite ceramics were prepared by following the procedure described in Section 3.2.3. Nominal dimensions of the green composite discs were 13 mm in diameter and 1.5 mm in thickness.

Prior to sintering, the discs were placed in a muffle furnace at 600 ºC for 2 h in order to remove binder in them. Composite discs were sintered in saggar configuration to prevent PbO losses in the piezoelectric constituent as mentioned in Section 3.2.3. Soaking temperatures were 1150, 1175, 1200, and 1225 ºC for composites having 10 wt% NF powder. The soak duration was fixed as 2 h. At the end of 1225 °C soaking, fusion of composites to the saggars was observed; therefore further sintering experiments were performed at lower temperatures. Bulk composites with 15 and 20 wt% NF powder were soaked at 1175 ºC for 2 h.

For each experiment three discs were produced. In order to observe ME effect, bulk composites were electroded and poled, as will be mentioned in the following parts. Later, brass plates were adhered to the parallel surfaces of the composites. A conductive silver epoxy adhesive Elecolit 325 A and B was used for this purpose. Copper wires were then soldered to the ends of the brass plates to have electrical output from the composite.

The appearance of bulk ME composites prepared for measurements is shown in Figure 3.13.

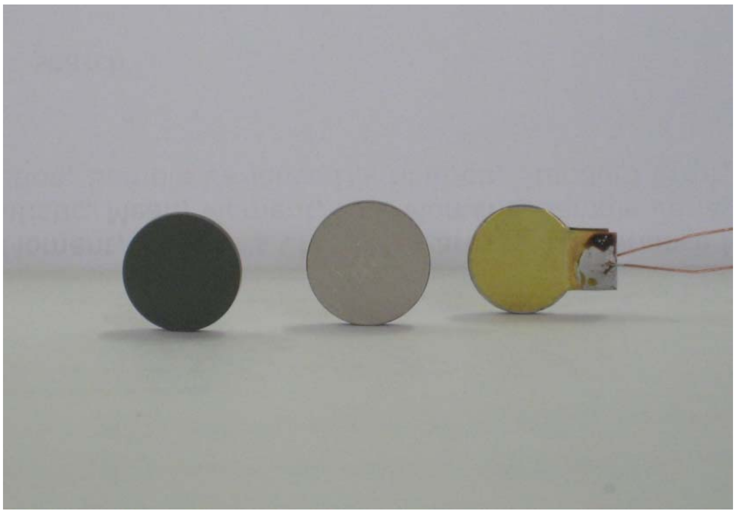

Figure 3.13 Bulk ME composite ceramics prepared for measurements.

3.2.4.2 Preparation of Laminated ME Composites

Piezoelectric and magnetostrictive components of the laminated composite were prepared separately. PSZT powder and Bi doped NF powder were used in manufacturing component ceramics according to the procedures described in Section 3.2.3. Sintered PSZT ceramic discs were electroded and poled according to piezoelectric characterization necessities as will be mentioned in the following parts. Parallel surfaces of NF discs were lapped on 800 grid emery paper as a surface preparation. The laminated composite was manufactured by sandwiching a PSZT disc between two NF discs.

Component discs were assembled together by using a room temperature curable conductive silver epoxy adhesive Elecolit 325 A and B. Brass plates were used in between component ceramics. Prior to handwork, surfaces of both PSZT and NF discs were cleaned with alcohol. A thin layer of silver adhesive was applied on all interfaces between the components and brass plates. Assembly was squeezed until epoxy curing. Copper wire was soldered to the ends of brass plates in order to have electrical output from piezoelectric component.

The appearance of the laminated ME composite manufactured for measurements is shown in Figure 3.14.

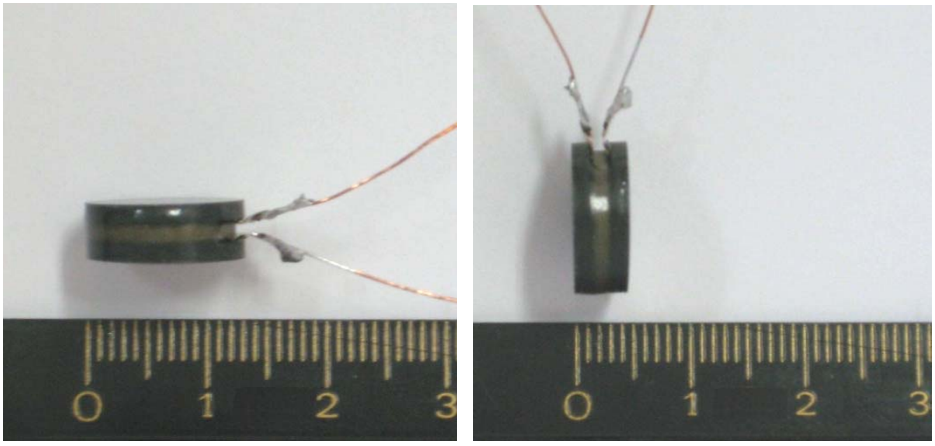

Figure 3.14 The laminated ME composite utilized in the study.

The short-hand designations used in the present study for the piezoelectric, magnetostrictive and bulk composite ceramics are tabulated in Table 3.1. Ceramics were soaked for a fixed duration of 2 h at all soaking temperatures.

Table 3.1 Designations of the sintered ceramics manufactured for the present study.

SAMPLES	T (ºC)	Sample Designation
Piezoelectric Samples		
$Pb_{0.95}Sr_{0.05}(Zr_{0.53}Ti_{0.47})O_3$+1 wt% Bi_2O_3+0.4 mol% MnO	1150	PSZT-1150
$Pb_{0.95}Sr_{0.05}(Zr_{0.53}Ti_{0.47})O_3$+1 wt% Bi_2O_3+0.4 mol% MnO	1175	PSZT-1175
$Pb_{0.95}Sr_{0.05}(Zr_{0.53}Ti_{0.47})O_3$+1 wt% Bi_2O_3+0.4 mol% MnO	1200	PSZT-1200
$Pb_{0.95}Sr_{0.05}(Zr_{0.53}Ti_{0.47})O_3$+1 wt% Bi_2O_3+0.4 mol% MnO	1225	PSZT-1225
$Pb_{0.95}Sr_{0.05}(Zr_{0.53}Ti_{0.47})O_3$+1 wt% Bi_2O_3+0.4 mol% MnO	1250	PSZT-1250
Magnetostrictive Samples		
$NiCo_{0.02}Cu_{0.02}Mn_{0.10}Fe_{1.8}O_{4-k}$	1150	NF-1150
$NiCo_{0.02}Cu_{0.02}Mn_{0.10}Fe_{1.8}O_{4-k}$	1175	NF-1175
$NiCo_{0.02}Cu_{0.02}Mn_{0.10}Fe_{1.8}O_{4-k}$	1200	NF-1200
$NiCo_{0.02}Cu_{0.02}Mn_{0.10}Fe_{1.8}O_{4-k}$	1225	NF-1225
$NiCo_{0.02}Cu_{0.02}Mn_{0.10}Fe_{1.8}O_{4-k}$	1250	NF-1250
$NiCo_{0.02}Cu_{0.02}Mn_{0.10}Fe_{1.8}O_{4-k}$ + 0.5 wt% Bi_2O_3	1250	NF+0.5 Bi_2O_3
$NiCo_{0.02}Cu_{0.02}Mn_{0.10}Fe_{1.8}O_{4-k}$ + 1 wt% Bi_2O_3	1250	NF+1 Bi_2O_3
$NiCo_{0.02}Cu_{0.02}Mn_{0.10}Fe_{1.8}O_{4-k}$ + 2 wt% Bi_2O_3	1250	NF+2 Bi_2O_3
$NiCo_{0.02}Cu_{0.02}Mn_{0.10}Fe_{1.8}O_{4-k}$ + 3 wt% Bi_2O_3	1250	NF+3 Bi_2O_3
Bulk ME Composites		
10 wt% NF mixed with 90 wt% PSZT	1150	10N-90P-1150
10 wt% NF mixed with 90 wt% PSZT	1175	10N-90P-1175
10 wt% NF mixed with 90 wt% PSZT	1200	10N-90P-1200
15 wt% NF mixed with 85 wt% PSZT	1175	15N-85P-1175
20 wt% NF mixed with 80 wt% PSZT	1175	20N-80P-1175

3.3 Characterization

3.3.1 X-Ray Diffraction, XRD

For the identification of the phases in the ceramic powders and in the sintered ceramics, XRD analyses were performed by using a computerized Rigaku DMAX-B unit with Cu-K_α radiation. Lattice parameters of the powders and sintered ceramics were calculated from the XRD patterns obtained during the analyses. The range of 2θ was 20° to 80° and 15° to 80° with 0.02° steps in PSZT and NF studies, respectively. Phase determinations in the bulk ME composite ceramics were also performed by XRD work.

3.3.2 Microstructural Examinations

Microstructural features in the ceramic powders and in the sintered ceramics were analyzed by examining the fractured surfaces under Scanning Electron Microscope, SEM. For this purpose a JEOL JSM 6400 SEM equipped with a Semafor Digitizer and NORAN X-Ray Microanalysis system was employed. Prior to SEM studies, ceramic surfaces were coated with about 250 Å thick layer of Au-Pd alloy to obtain a continuous conducting layer on the fracture surfaces.

3.3.3 Density Measurements

Density of the sintered ceramics was determined by using Archimedes' principle. Xylene (Merck 8685) was selected as the immersion medium. A Sartorius Model CP224S-0CE electronic balance equipped with a density determination kit was utilized for weight measurements.

The procedure involved in the determination of the density of a sintered ceramic sample was as follows: The flat surfaces of the sample were polished with 800 grid emery paper. The sample was then kept in an oven at 150 ºC for 2 h to obtain dry weight. Next, the sample was immersed in Xylene and kept there for 48 h until full saturation. Weight of the saturated sample was recorded while it was suspended in Xylene on the density kit as suspended weight. Afterwards, the sample was taken out of Xylene, excess liquid was wiped out immediately from the surface and then the sample was weighted in air; this was recorded as saturated weight.

Bulk densities of the sintered ceramics were calculated according to the following formula:

$$\rho_{\text{bulk}} = \frac{W_{\text{dry}} \cdot \rho_{\text{Xylene}}}{W_{\text{sat}} - W_{\text{susp}}} \quad (\text{g/cm}^3) \tag{3.1}$$

where ρ_{dry}: bulk density of the sintered ceramic, g/cm^3
W_{dry}: dry weight of the sintered ceramic, g
ρ_{Xylene}: density of Xylene = 0.86 g/cm^3
W_{sat}: saturated weight of the sintered ceramic, g
W_{susp}: suspended weight of the sintered ceramic, g

3.3.4 Dielectric and Piezoelectric Measurements

The dielectric and piezoelectric properties of PSZT and bulk ME composite ceramics were determined by measurements on the discs which were metallized first on the parallel surfaces and then poled under a high dc field. The metallization process (electroding) started by lapping the flat surfaces on 800 grid emery paper until the thickness was reduced to 1 mm. Diameter and thickness were recorded prior to metallization. For metallization, parallel surfaces were painted with a fired-on conductive silver paste, a product of Gwent Company sold as brand C71208R3. The silver paste was fixed on the surface by heating the ceramic to 600 °C and holding there for 15 min.

Electroded samples were poled in a silicon oil bath at 125 °C under a dc-electrical field. During poling, the field was increased gradually by 250 V steps while ceramics were kept for 15 min at each step. The ultimate field strength was 3 kV/mm for PSZT ceramics whereas it was between 1.25 to 2 kV/mm for bulk ME composites. The development of piezoelectric activity in the PSZT ceramic was followed by measuring the piezoelectric strain coefficient, d_{33}. IRE Standards [50] were used for characterization of dielectric and piezoelectric properties of poled ceramics.

3.3.4.1 Piezoelectric Strain Coefficient, d_{33}

The piezoelectric strain coefficients of the poled ceramics were determined by a Berlincourt D_{33}-piezometer. In principle, this device applies a cyclic stress to the ceramic sample and in turn measures the density of the developed charge across the flat surfaces of the ceramic. This phenomenon can be formulated as:

$$d_{33} = \frac{Q/A}{F/A} = \frac{Q}{F} \quad \text{(C/N)} \tag{3.2}$$

3.3.4.2 Impedance Spectra

The characteristic impedance spectrum of a poled piezoelectric ceramic is given in Figure 3.15. The spectrum was obtained by running a PSZT ceramic in a HP 4194A Impedance and Gain Phase Analyzer between 1 kHz to 1 MHz frequencies in the impedance mode of the device.

The resonance frequency, f_r, and anti-resonance frequency, f_a, in the impedance spectra of the piezoelectric ceramic were used for mechanical quality factor and planar coupling coefficient determinations.

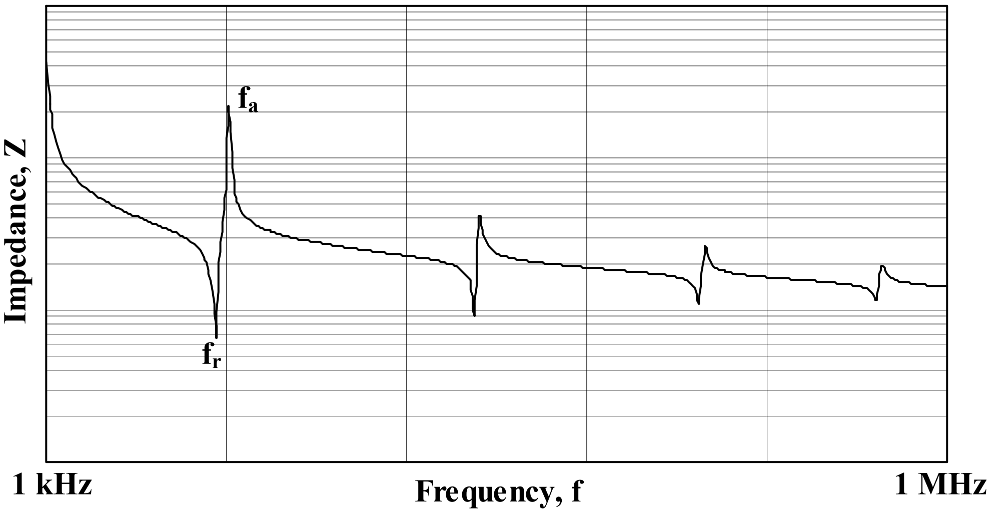

Figure 3.15 An impedance spectrum of a poled PSZT ceramic.

3.3.4.3 Electromechanical Coupling Factor, k

In the present study, planar coupling coefficient, k_p, was used since PSZT and bulk ME composite ceramics were manufactured in the form of thin circular discs.

The planar coupling factor is a function of resonance and antiresonance frequencies according to the Jakobian type expression given below:

$$\frac{k_p^2}{1-k_p^2} = f\left[J_o, J_1, \sigma^E \frac{f_a - f_r}{f_r}\right] \tag{3.3}$$

where k_p: planar coupling coefficient

J_o: first kind and zero order Bessel function

J_1: first kind and first order Bessel function

σ^E: Poisson's ratio

f_a: anti-resonance frequency

f_r: resonance frequency

The plot of this expression, shown in Figure 3.16, has been used as an alternative way for k_p determination [8]. It should be emphasized that this plot is valid only for disc ceramics having diameter to thickness ratio greater than 10.

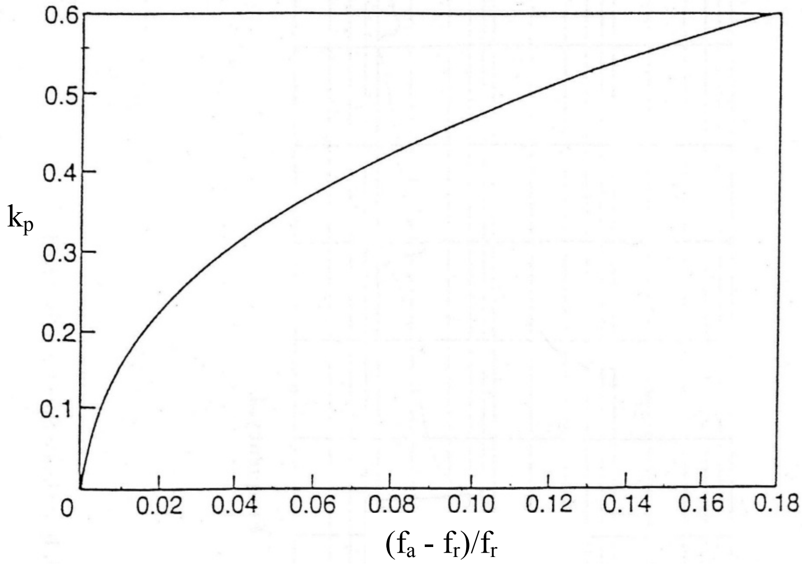

Figure 3.16 Graphical representation of planar coupling coefficient for thin dics.

3.3.4.4 Mechanical Quality Factor, Q_m

The resistor and capacitor elements in the mechanical branch of the equivalent circuit of a piezoelectric ceramic were evaluated in the equivalent circuit mode of HP 4194A Impedance and Gain Phase Analyzer. Mechanical quality factor of the poled PSZT and bulk ME composite ceramics was then determined from:

$$Q_m = \frac{1}{2 \cdot \pi \cdot f_r \cdot R \cdot C_a} \tag{3.4}$$

where Q_m: mechanical quality factor, unitless

f_r: resonance frequency at first harmonic, Hz

R: resistance in the mechanical portion of the equivalent circuit, Ohm

C_a: capacitance in the mechanical portion of the equivalent circuit, Farad

3.3.4.5 Dielectric Constant, K^T and Loss Tangent, tanδ

Capacitance data of the poled PSZT and bulk ME composite ceramics were collected by utilizing a HP4194A Impedance and Gain Phase Analyzer at a frequency of 1 kHz in the capacitance mode. The capacitance at this frequency is referred to as 'free capacitance' and represented with C^T. Dielectric constants of the poled ceramics were calculated from:

$$C^T = K^T \cdot \varepsilon_o \cdot \frac{A}{t} \tag{3.5}$$

where C^T: capacitance of the ceramic at 1 kHz, Farad
K^T: relative dielectric constant, unitless
ε_o: permittivity of vacuum, 8.85×10^{-12} F/m
A: cross-sectional area of the ceramic, m^2
t: thickness of the ceramic, m

Loss tangent, tanδ, of poled PSZT and bulk ME composite ceramics was obtained by employing a HP 4194A Impedance and Gain Phase Analyzer in loss tangent mode at 1 kHz frequency.

3.3.4.6 Curie Point, T_C

For T_C determinations, contacts from parallel surfaces of a ceramic were connected to the terminals of a HP 4194A Impedance and Gain Phase Analyzer, which operated in capacitance mode at 1 kHz. During the experiment, ceramic was heated in a tubular furnace with a rate of 5 °C per min. Capacitance of the ceramic was recorded for every 2 °C interval until the peak point was observed in the T-C plot.

3.3.5 Electrical and Magnetic Measurements

3.3.5.1 Electrical Resistivity, ρ

Prior to the electrical measurement, one of the NF ceramic discs was lapped on 800 grid emery paper until thickness was reduced to 3 mm. Diameter and thickness of the disc was then recorded. Clean and parallel surfaces of the NF disc was painted with Gwent C71208R3 silver paste and then fired at 600 °C for 15 min in order to obtain metallized surfaces.

Electrical resistance of the electroded ceramic was evaluated by using a HP4140B picoammeter available in the laboratory. The NF ceramic was placed in between probes of the device. The device applied dc voltage on the ceramic and measured the current passing through it simultaneously. Experiment was performed at room temperature.

Electrical resistance values were calculated according to the Ohm's Law:

$$V = I \cdot R \tag{3.6}$$

where V: potential difference between two probes, Volts
I: current passing through the ceramic, Amperes
R: resistance of the ceramic, Ohm

DC-resistivities of the ceramics were obtained from the following formula:

$$\rho = R \cdot \frac{A}{t} \tag{3.7}$$

where ρ: DC-resistivity of the ceramic, ohm-cm
A: area of the metallic electrode of the ceramic, cm^2
t: thickness of the ceramic, cm

3.3.5.2 Initial Magnetic Permeability, μ_i

Initial magnetic permeability measurements were carried out on toroid NF ceramics. Prior to measurements, rough surfaces of the toroids were lapped on 800 grid emery paper and sharp edges were smoothed. After recording outer diameter, inner diameter and thickness, toroids were wound with ~50 turns of enameled copper wire of 0.35 mm diameter.

After removing the surrounding enamel of the copper wire, ends of the wire were directly connected to the terminals of a HP 4194A Impedance Gain and Phase Analyzer. μ_i measurements were performed in inductance mode of the device at 1 MHz frequency. Low excitation voltages of 0.01 V and 0.02 V were used in measurements.

The initial magnetic permeability of the NF ceramics was calculated from [20]:

$$\mu_i = \frac{L_o \cdot \pi \cdot (D_o + D_i)}{N^2 \cdot \mu_o \cdot t \cdot (D_o - D_i)} \tag{3.8}$$

where μ_i: initial magnetic permeability

L_o: inductance at zero applied field, H

D_o: outer diameter of the toroid, cm

D_i: inner diameter of the toroid, cm

N: number of turns

μ_o: permeability constant = $4\pi \cdot 10^{-9}$ H/cm

t: thickness of the toroid, cm

Inductance at zero applied field, L_o, was determined by extrapolating the inductance values obtained at 0.01 and 0.02 V to zero volt condition.

3.3.5.3 Magnetostriction, λ

In order to measure the dimensional changes of the NF and bulk ME composite ceramics under the applied magnetic field, magnetic strain gauges of Vishay Company Model H06A-AC1-125-700 were utilized. Prior to magnetostriction measurements, parallel surfaces of the ceramics were lapped with 400 grid emery paper and cleaned with alcohol. Gauge was installed on one of the surface of the ceramic with glue. After installation, a cable was soldered to the end of the gauge. Gauge installed ceramic was then placed in a foam cage in order to prevent any displacement during application of the magnetic field. The gauge installed NF ceramic is illustrated in Figure 3.17.

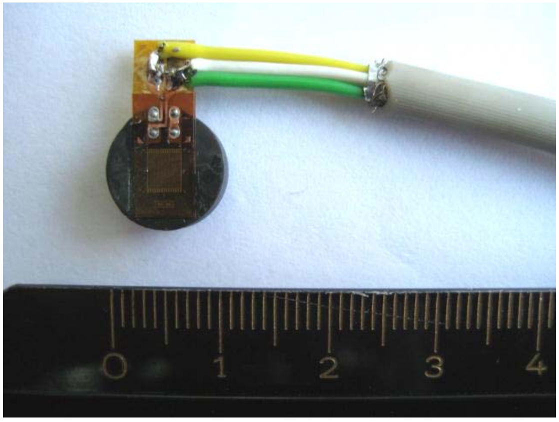

Figure 3.17 Magnetic strain gauge installed NF ceramic.

Foam assembly was next placed between the poles of the LakeShore Model637 DC-Magnet. A Magnet Physik FH 51 gaussmeter was used to measure the magnetic field strength. Strain values observed in response to the magnetic field were recorded in the data acquisition system and evaluated in the computer. Magnetic field was applied to the ceramic until reaching saturation strain. Measurements were conducted under two conditions:

(1) direction of the applied field was parallel to the direction of strain measurement.

(2) direction of the applied field was perpendicular to the direction of strain measurement.

A photograph and schematic drawing of the magnetostriction set up is represented in Figure 3.18.

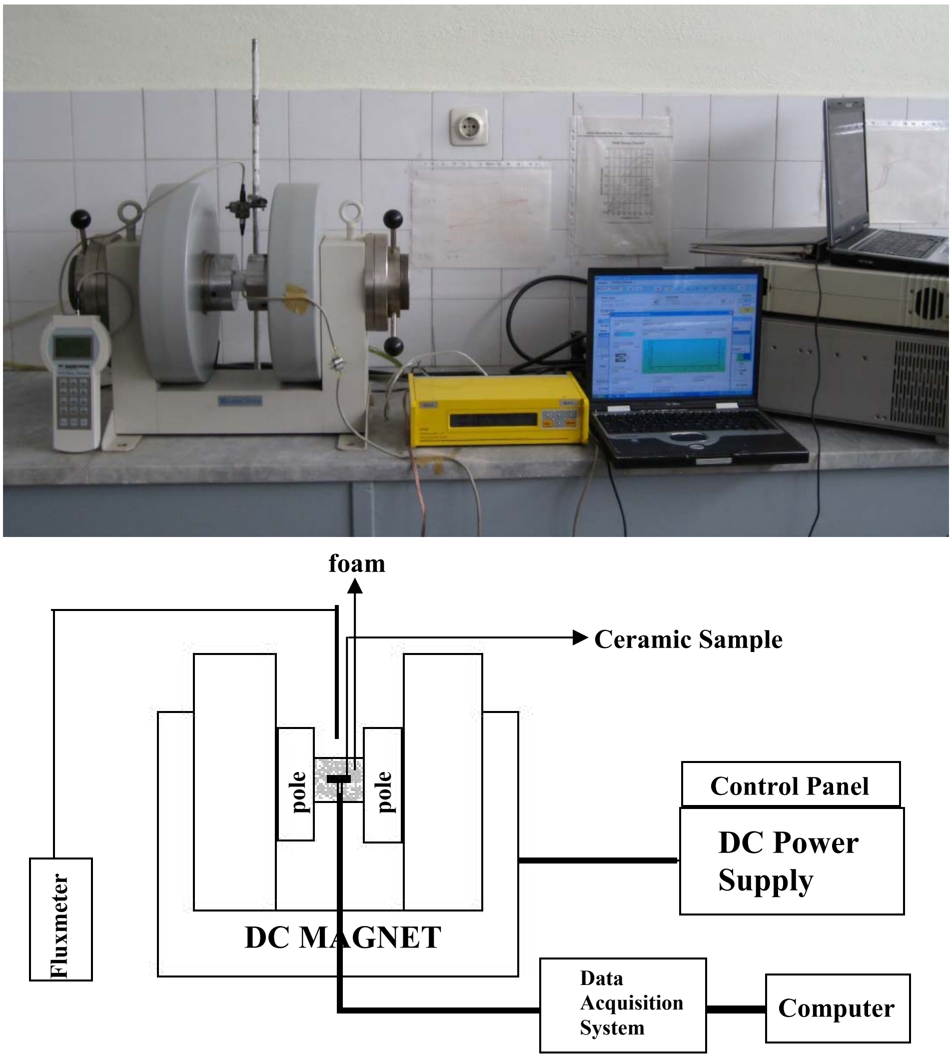

Figure 3.18 The magnetostriction setup used in the study.

3.3.6 ME Effect

It was stated that the ME effect is induced by a weak ac field applied in the presence of a strong dc field bias [1, 5]. In many of the previous studies on ME composites [32, 40, 44, 45], an electromagnet was used to provide a dc field (up to 10 kOe) and the low ac field (up to 10 Oe) was superimposed on the dc field by utilizing Helmholtz coils. The generated charge in the piezoelectric constituent was measured and converted into a proportional output voltage through a charge amplifier (V=Q/C) and the output voltage was evaluated by a digital oscilloscope. The ME voltage coefficient of the samples was determined by dividing the output voltage to the thickness of the PZT layer and ac magnetic field. In the present study, however, due to lack of Helmholtz coils, an alternative measurement technique was used.

ME composites were assembled within a foam cage in order to prevent their displacement under the applied magnetic field. The assembly was placed between the poles of a LakeShore Model637 DC Magnet. Magnetic field strength was measured by utilizing a Magnet Physik FH 51 gaussmeter. Wires from the ends of the brass plates of composites were connected to the terminals of a HP 54645A oscilloscope. The induced voltage due to the piezoelectric component in the ME composites was observed as a peak in the screen of the oscilloscope when field was applied. Screen images of the oscilloscope were transferred to the computer. During the measurements, magnetic field was increased with a rate of 90 A/sec until saturation point. Schematic representation of the setup is shown in Figure 3.19. ME outputs were calculated by taking the ratio of the voltage peak height to the magnitude of applied magnetic field.

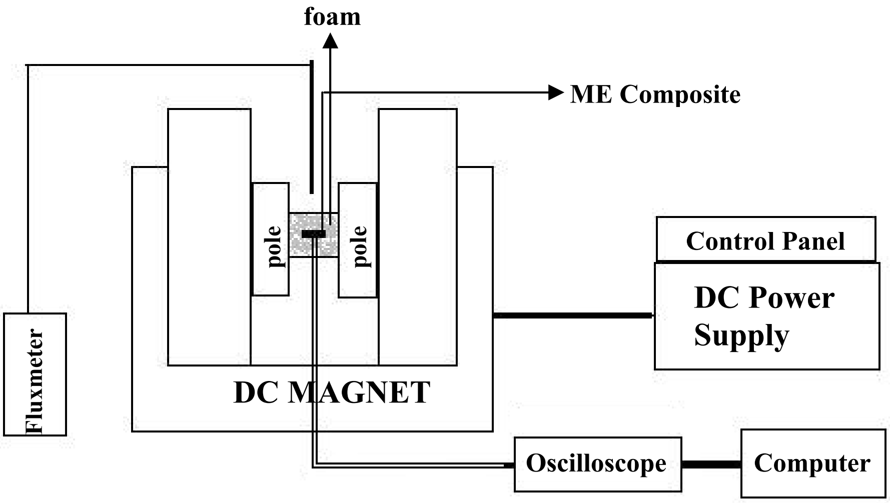

Figure 3.19 Schematic representation of the setup used for ME effect.

CHAPTER 4

DATA AND RESULTS

4.1 General

The characterization of piezoelectric and magnetostrictive ceramics was performed in accordance with the methods described in the previous chapter. Microstructural examinations, XRD analyses and the results based on the data obtained throughout the measurements on the sintered ceramics are presented in this chapter. Studies on the bulk and laminated ME composites are as well included in the following sections.

4.2 Data and Results on Piezoelectric Ceramics

4.2.1 XRD of Sintered PSZT Ceramics

XRD patterns of PSZT ceramics soaked at 1150, 1175, 1200, 1225, and 1250 ºC are shown in Figure 4.1. The splitting in the diffraction peaks of (100), (200), (201), and (211) planes revealed that PSZT ceramics had tetragonal crystal structure. Lattice parameters of sintered PSZT ceramics were calculated as a = 4.037 Å and c = 4.115 Å. Degree of tetragonality, c/a, was 1.0193.

Theoretical density of sintered PSZT ceramics was determined as 7.957 g/cm^3 from lattice parameters according to the following relationship:

$$\rho_{th} = \frac{M}{N \cdot V} \tag{4.1}$$

where ρ_{th}: theoretical density, g/cm^3

M: molecular weight of the ceramic, g

N: Avagadro's number = 6.02×10^{23} molecules/mole

V: volume of the unit cell = $a^2 \times c$, cm^3

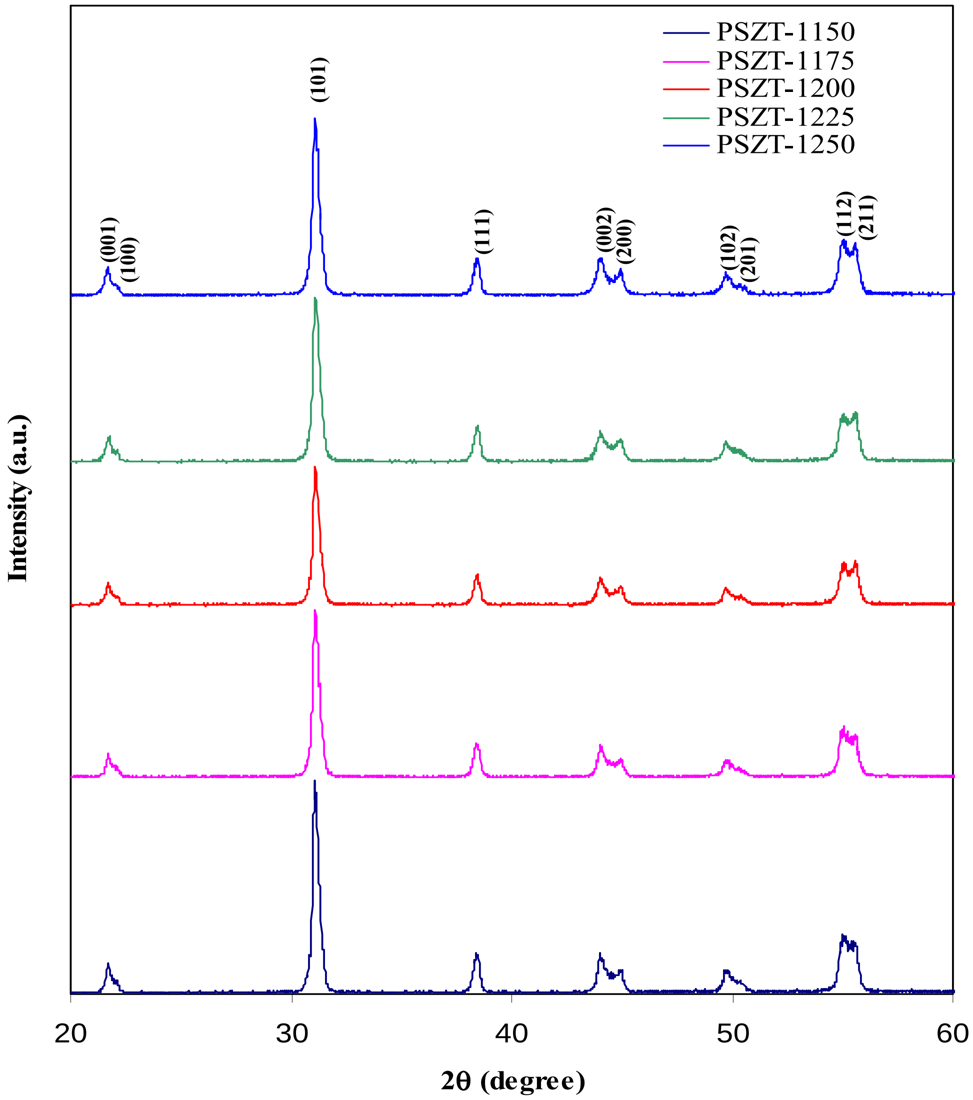

Figure 4.1 XRD patterns of PSZT ceramics sintered at different temperatures.

4.2.2 Sintered Density

Data on the density of PSZT ceramics sintered at temperatures in the interval 1150 ºC to 1250 ºC are given in Table 4.1. These data were converted into percentage theoretical density, %TD, with the help of the following expression:

$$\%TD = \frac{\rho_{exp}}{\rho_{th}} \cdot 100 \tag{4.2}$$

where ρ_{exp}: density measured by Archimedes' method, g/cm^3

ρ_{th}: theoretical density =7.957 g/cm^3

Table 4.1 Experimental and %TD densities of sintered PSZT ceramics.

Sample Designation	ρ_{exp} (g/cm^3)	%TD
PSZT-1150	7.365	92.56
PSZT-1175	7.375	92.69
PSZT-1200	7.404	93.05
PSZT-1225	7.384	92.80
PSZT-1250	7.385	92.81

As seen in Table 4.1, at all sintering temperatures the densification was around 93 %TD.

4.2.3 Microstructural Features

In order to obtain information about grain morphology, fractured surfaces of the sintered ceramics were examined by SEM. Representative images of the microstructures are shown in Figures 4.2 and 4.3.

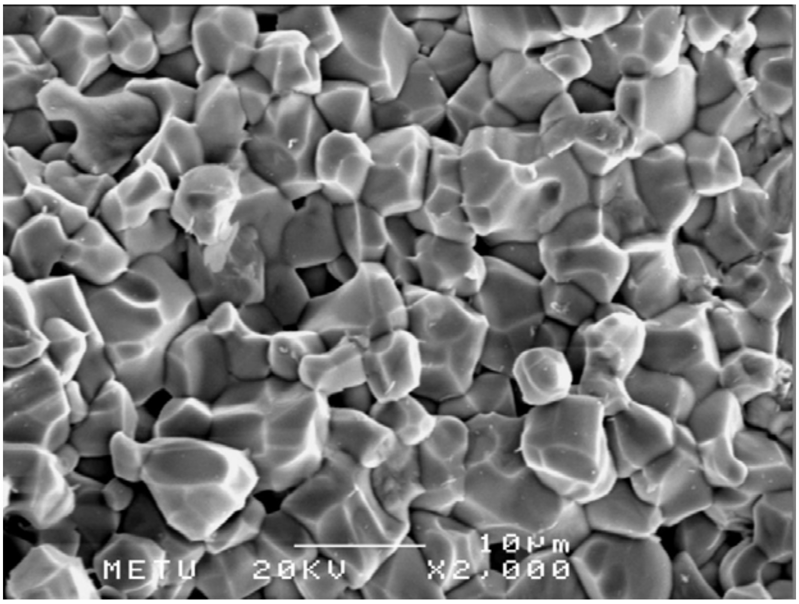

Figure 4.2 SEM fractograph of the PSZT ceramic sintered at 1150 °C for 2 h.

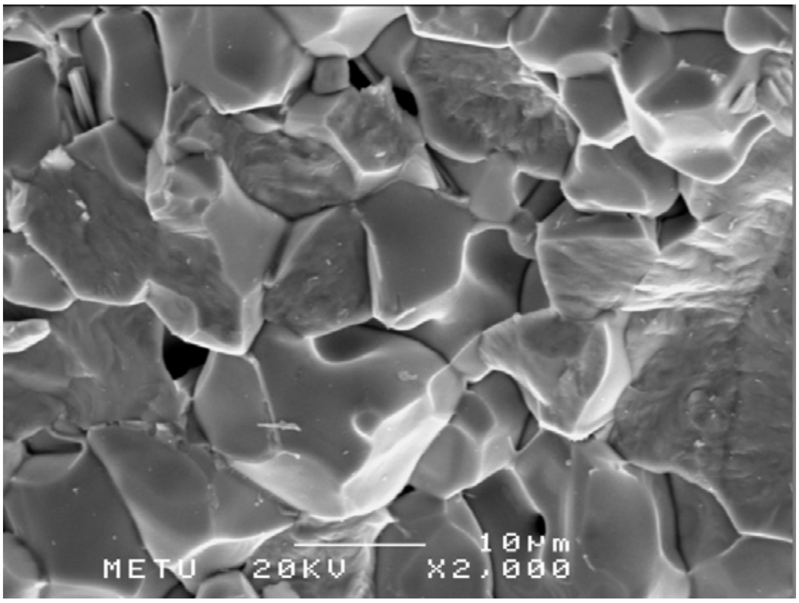

Figure 4.3 SEM fractograph of the PSZT ceramic sintered at 1250 °C for 2 h.

As expected, grain size increased gradually as the sintering temperature was raised from 1150 ºC to 1250 ºC. Homogeneous structure with equiaxed grains was observed at all soaking temperatures. From the fractographs shown in Figures 4.2 and 4.3 the average grain size of the PSZT-1150 and PSZT-1250 ceramics was estimated as 5 µm and 12 µm, respectively.

At lower firing temperatures, sintering was inferior. Porosity was observed in all PSZT ceramics. Pores were essentially closed type.

4.2.4 Dielectric and Piezoelectric Properties

Dielectric and piezoelectric characterization of PSZT ceramics were performed according to the IRE standards mentioned in Section 3.3.4. For each sintering experiment two ceramic samples were evaluated. Properties of the ceramics were measured twice; that is 24 h after the poling process and a week later. The average of these two values was taken into account to get reliable data.

4.2.4.1 Dielectric Constant, K^T and Loss Tangent, tanδ

Dielectric constants of PSZT ceramics were calculated from Equation 3.5 by using the dimensional parameters and capacitance values listed in Table 4.2. The variation in the dielectric constant with temperature is displayed in Figure 4.4. The rise in K^T values implied that PSZT ceramics attained increased polarization tendency at higher sintering temperatures.

Table 4.2 Values of diameter (D), thickness (t), capacitance (C), dielectric constant (K^T), loss tangent (tanδ), piezoelectric strain coefficient (d_{33}), anti-resonance frequency (f_a), resonance frequency (f_r), planar coupling coefficient (k_p), resistance (R) and capacitance (C_a) elements of the equivalent circuit and mechanical quality factor (Q_m) of PSZT ceramics. Dielectric properties were measured at 1 kHz frequency.

Sample Designation	D (mm)	t (mm)	C (nF)	K^T	tanδ	d_{33} (pC/N)	f_a (Hz)	f_r (Hz)	$\Delta f/f_r$	k_p	R (Ω)	C_a (pF)	Q_m
PSZT-1150	10.92	1	0.94	1133	0.010	337	205437	190651	0.078	0.42	57.92	98.16	149
PSZT-1150	10.98	1	1.00	1193	0.010	402	200877	184653	0.088	0.45	40.97	141.37	158
PSZT-1175	10.98	1	1.04	1242	0.008	412	202313	185071	0.093	0.46	32.39	156.50	179
PSZT-1175	10.93	1	1.00	1205	0.010	370	205127	189262	0.084	0.43	45.31	121.70	154
PSZT-1200	10.98	1	1.08	1285	0.009	396	203909	185743	0.098	0.47	35.25	175.35	141
PSZT-1200	10.98	1	1.07	1278	0.009	414	203379	185657	0.095	0.46	35.56	144.96	176
PSZT-1225	10.95	1	1.10	1321	0.009	416	204615	186707	0.096	0.46	32.78	162.46	164
PSZT-1225	10.97	1	1.07	1280	0.009	406	205495	187278	0.097	0.46	34.86	157.07	157
PSZT-1250	10.98	1	1.10	1308	0.009	422	203608	185033	0.100	0.47	32.47	174.93	157
PSZT-1250	11.01	1	1.12	1333	0.007	446	203030	183880	0.104	0.48	27.89	188.09	169

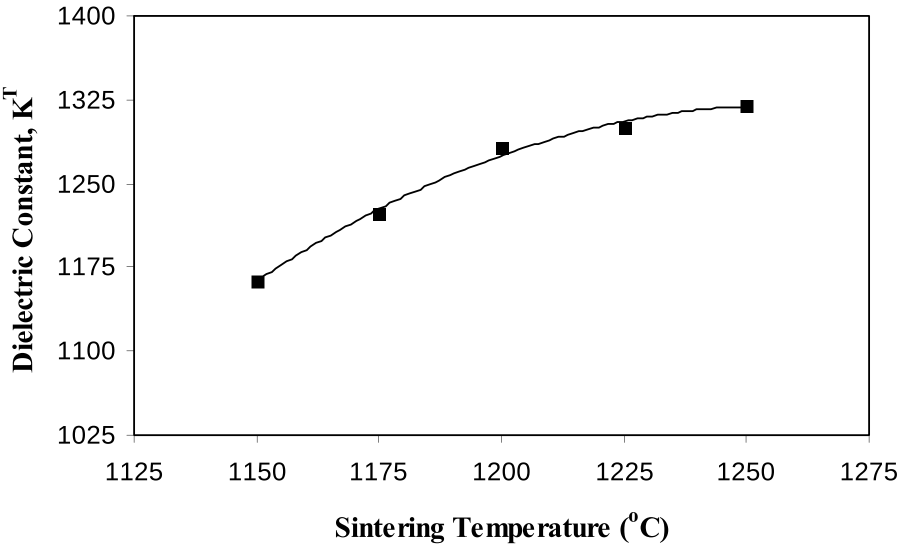

Figure 4.4 Variation in dielectric constant with sintering temperature.

The variation in tanδ with soaking temperature is shown in Figure 4.5. As observed from the graph, loss tangent decreased with sintering temperature. The declining trend in tanδ could be attributed to the enlargement in grain size at higher sintering temperatures.

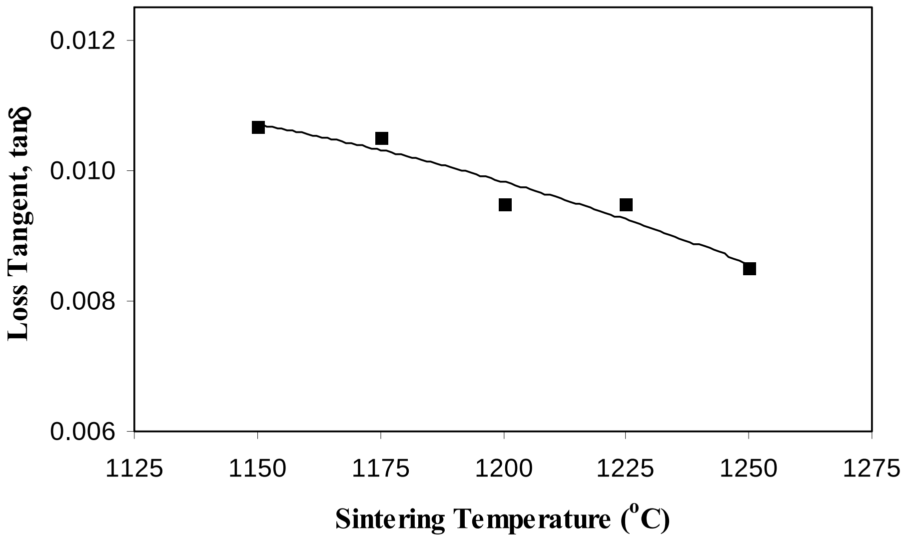

Figure 4.5 Variation in loss tangent with sintering temperature.

4.2.4.2 Piezoelectric Strain Coefficient, d_{33}

The piezoelectric strain coefficient, d_{33}, is the principal parameter for expressing degree of piezoelectric activity. The data on the piezoelectric strain coefficient of PSZT ceramics are tabulated in Table 4.2. Variation in d_{33} with sintering temperature is shown in Figure 4.6.

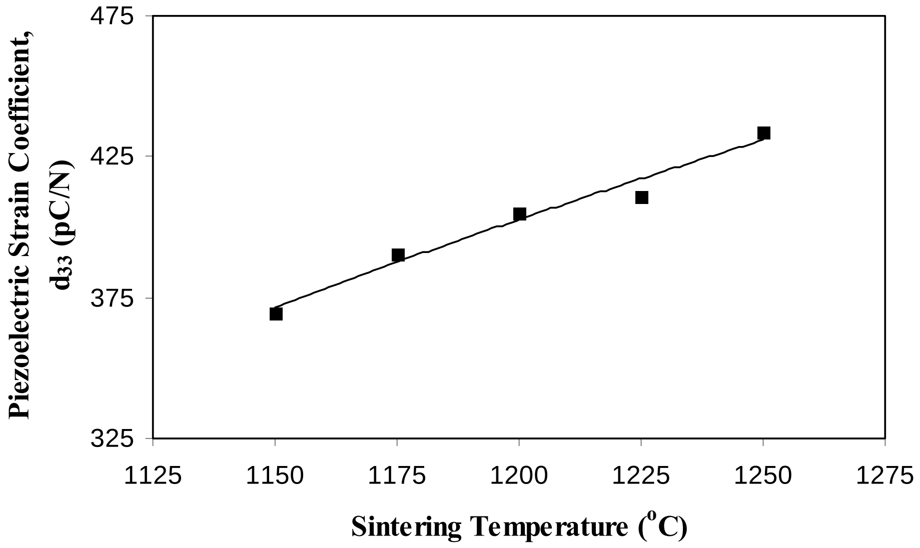

Figure 4.6 Variation in piezoelectric strain coefficient with sintering temperature.

As seen from the graph, the piezoelectric strain coefficient of PSZT ceramics increased steadily with increasing sintering temperature.

4.2.4.3 Electromechanical Coupling Factor, k_p

Planar coupling coefficient of PSZT ceramics were estimated from the graph in Figure 3.16 by making use of the resonance frequencies in the impedance spectra. The data on f_a, f_r and k_p are listed in Table 4.2. Variation in k_p with sintering temperature is represented graphically in Figure 4.7. As revealed from the graph, the planar coupling coefficient increased with increasing sintering temperature. This implied that the ceramics sintered at higher temperature would exhibit higher energy conversion capability.

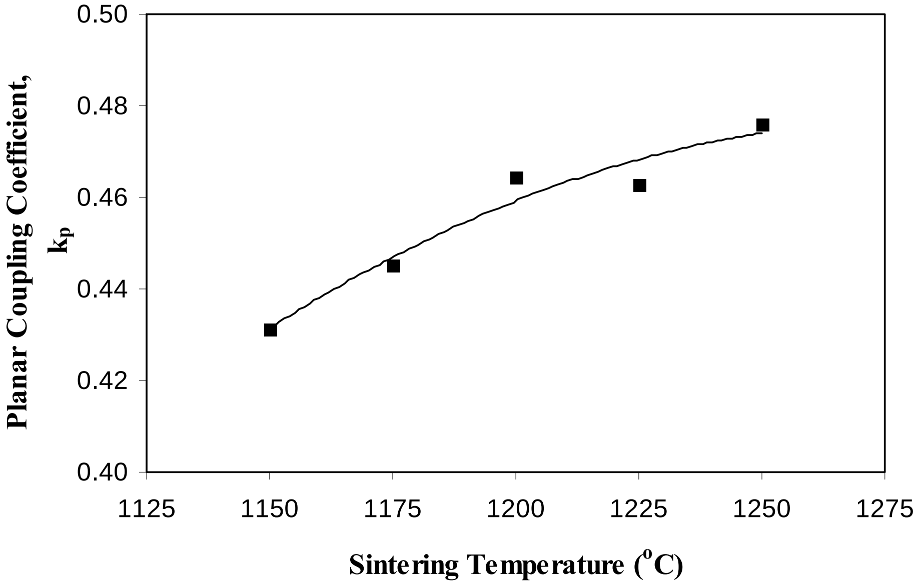

Figure 4.7 Variation in planar coupling coefficient with sintering temperature.

4.2.4.4 Mechanical Quality Factor, Q_m

The data on the resistance and capacitance elements of the equivalent circuit and the resonant frequency were used to calculate the mechanical quality factor of PSZT ceramics by using Equation 3.4. The values of Q_m listed in Table 4.2 were used to construct the curve in Figure 4.8 for displaying the variation in Q_m with sintering temperature. Q_m values indicated that PSZT ceramics were basically soft in nature. Q_m values varied only slightly with increasing sintering temperature as seen from the graph.

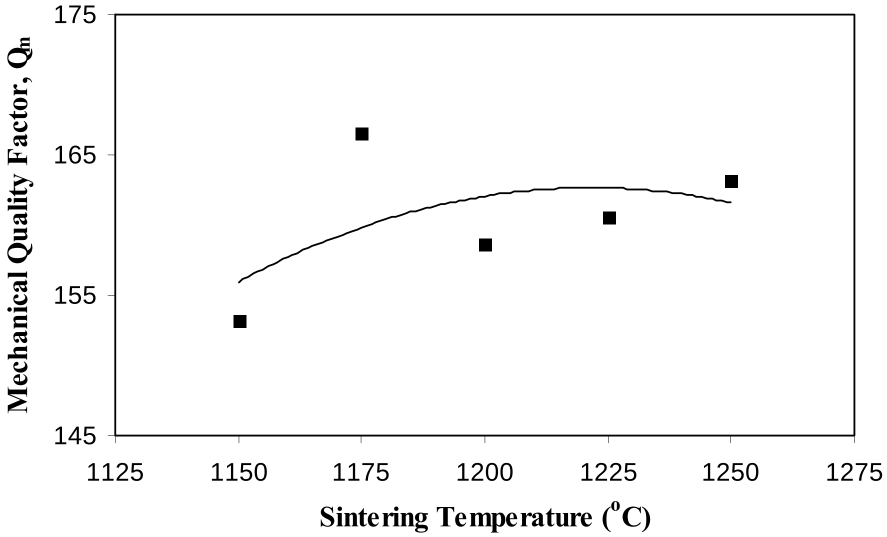

Figure 4.8 Variation in mechanical quality factor with sintering temperature.

4.2.4.5 Curie Point, T_C

The curves in Figure 4.9 have been constructed to show the variation in the dielectric constant with service temperature. The peak in each curve represented the Curie point corresponding to tetragonal to cubic transition in the ceramic. The curves indicated that, within limits of experimental error, the Curie point of PSZT ceramics were not affected greatly by changes in the sintering temperature.

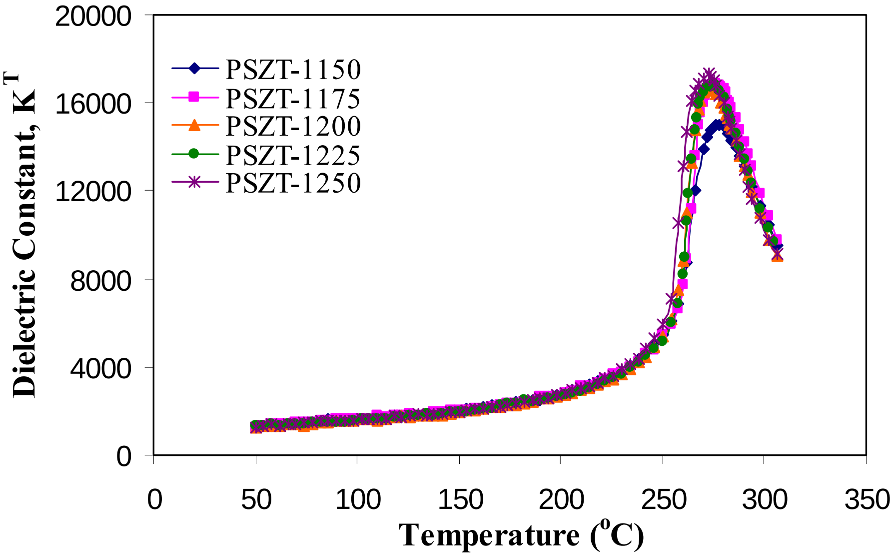

Figure 4.9 Variation in dielectric constant with service temperature.

4.3 Data and Results on Magnetostrictive Ceramics

4.3.1 XRD of Sintered NF Ceramics

XRD patterns of magnetostrictive ceramics sintered at temperatures 1150, 1175, 1200, 1225, and 1250 ºC are depicted in Figure 4.10. Diffraction planes are also indicated on the patterns. All diffraction peaks were representative of the phase-pure nickel ferrite according to JCPDS-ICDD 2002 PDF-2 data base number 10-0325. Slight shift in peaks were due to the presence of dopants in the nickel ferrite lattice. Lattice parameter of sintered NF ceramics was determined as a = 8.331 Å from XRD patterns.

Theoretical density of sintered NF ceramics was calculated as 5.313 g/cm^3 according to the following relationship [21]:

$$\rho_{th} = \frac{8 \cdot M}{N \cdot V} \tag{4.3}$$

where ρ_{th}: theoretical density, g/cm^3

M: molecular weight of the ceramic, g

N: Avagadro's number = 6.02 x 10^{23} molecules/mole

V: volume of the unit cell = a^3, cm^3

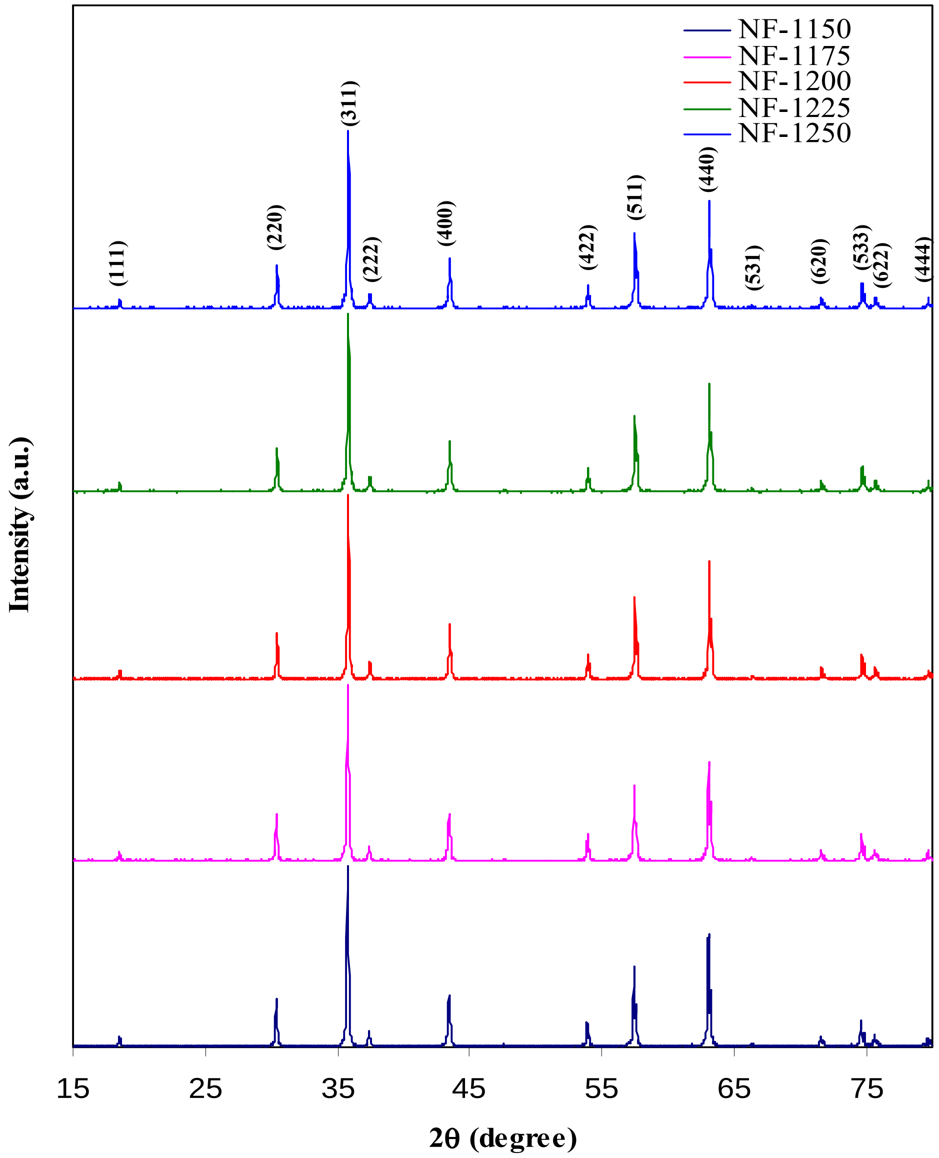

Figure 4.10 XRD patterns of NF ceramics soaked at different temperatures.

4.3.2 Sintered Density

Density of the sintered NF ceramics as determined by Archimedes' principle are listed in Table 4.3. In the last column of the table the sintered densities are expressed in terms of percentage densification with respect to the theoretical density of NF ceramics. %TD values were obtained with the help of Equation 4.2.

Table 4.3 Experimental and %TD densities of sintered NF ceramics.

Sample Designation	**ρ_{exp} (g/cm^3)**	**%TD**
NF-1150	3.738	70.36
NF-1175	3.855	72.56
NF-1200	4.013	75.53
NF-1225	4.146	78.04
NF-1250	4.305	81.03

As seen from the data in Table 4.3, NF ceramics had considerably poor densification even after sintering at 1250 °C. Densification of NF ceramics was improved by the addition of a sintering aid, Bi_2O_3, as will be discussed in the following sections.

4.3.3 Microstructural Features

Magnetostrictive ceramics based on nickel ferrite were sintered by soaking between 1150 to 1250 ºC for 2 h. SEM fractographs were used to assess the effect of sintering temperature on the microstructural features of sintered ceramics.

Intergranular fracture occurred in all NF ceramics as revealed from SEM images in Figures 4.11 and 4.12. The reason for this type of fracture mechanism could be assigned to the partial formation of the intergranular contacts due to inadequate soaking temperature or time. Average grain size of the sintered NF ceramics showed a slight increase with soaking temperature. Grain size was estimated as 2 µm and 4 µm for NF-1150 and NF-1250 ceramics, respectively. These values were slightly larger than the average particle size of the NF powder. Amount of porosity decreased with increasing soaking temperature, meanwhile considerable amount of open and closed pores were present in all sintered NF ceramics.

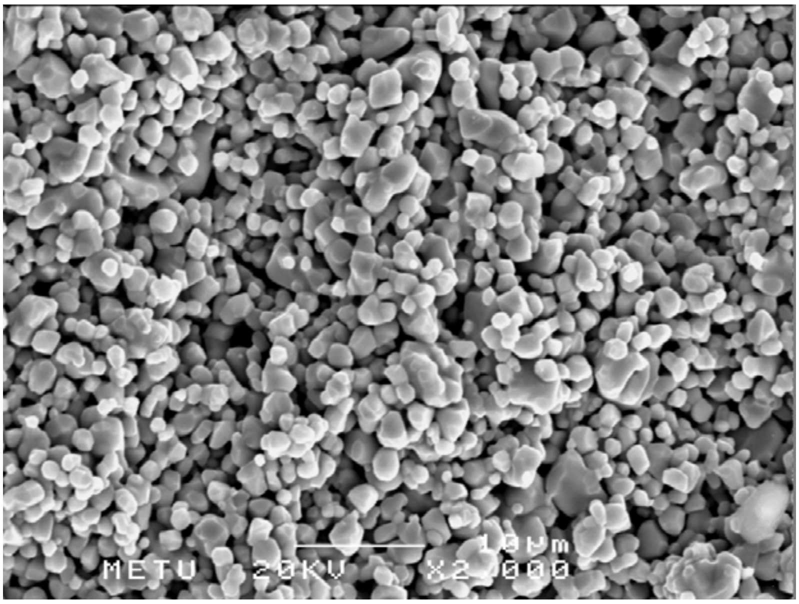

Figure 4.11 SEM fractograph of the NF ceramic sintered at 1150 °C for 2 h.

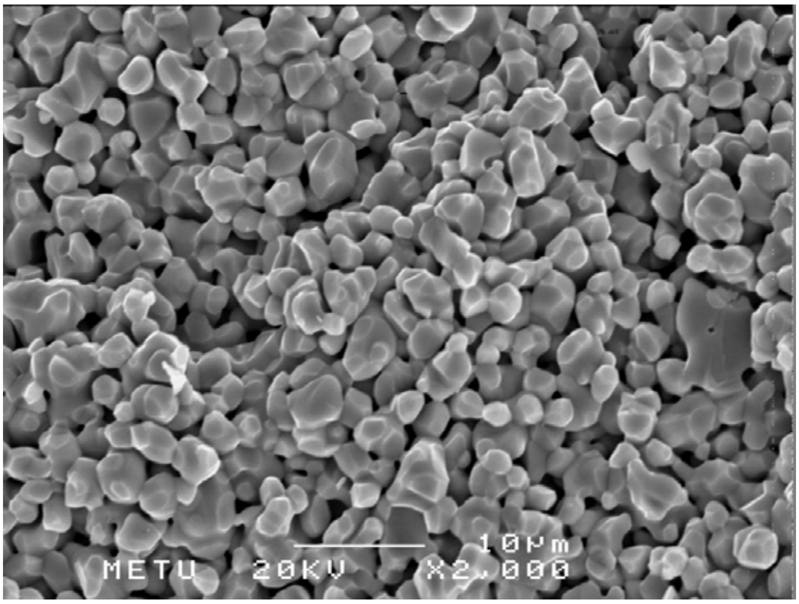

Figure 4.12 SEM fractograph of the NF ceramic sintered at 1250 °C for 2 h.

4.3.4 Electrical and Magnetic Properties

4.3.4.1 Electrical Resistivity, ρ_{DC}

Electrical resistivities of NF ceramics were determined by following the procedure outlined in Section 3.3.5.1. DC-resistivities of NF ceramics were calculated from Equations 3.6 and 3.7 by making use of the voltage-current data. Dimensional parameters of NF ceramics together with data on resistance and DC-resistivity are tabulated in Table 4.4.

Table 4.4. Values of diameter (D), thickness (t), resistance (R), and DC-resistivity (ρ_{DC}) of NF ceramics.

Sample Designation	D (mm)	t (mm)	R (ohm)	ρ_{DC} (ohm-cm)
NF-1150	12.30	3	4.40×10^{6}	1.74×10^{7}
NF-1175	12.15	3	2.38×10^{6}	9.19×10^{6}
NF-1200	12.05	3	2.51×10^{6}	9.52×10^{6}
NF-1225	11.90	3	2.43×10^{6}	9.00×10^{6}
NF-1250	11.70	3	3.45×10^{6}	1.24×10^{7}

Variation in the DC-resistivity with sintering temperature is displayed in Figure 4.13. The graph shows that, DC-resistivity varied mildly with temperature, exhibiting a plateau of minima in the range from 1175 °C to 1225 °C. Initial reduction in ρ_{DC} would be assigned to the increase in grain size with increasing soaking temperature. The reason for the rise in ρ_{DC} at higher temperatures could be attributed to the reduction of open pores with an increase in densification. Details will be mentioned in the following chapter.

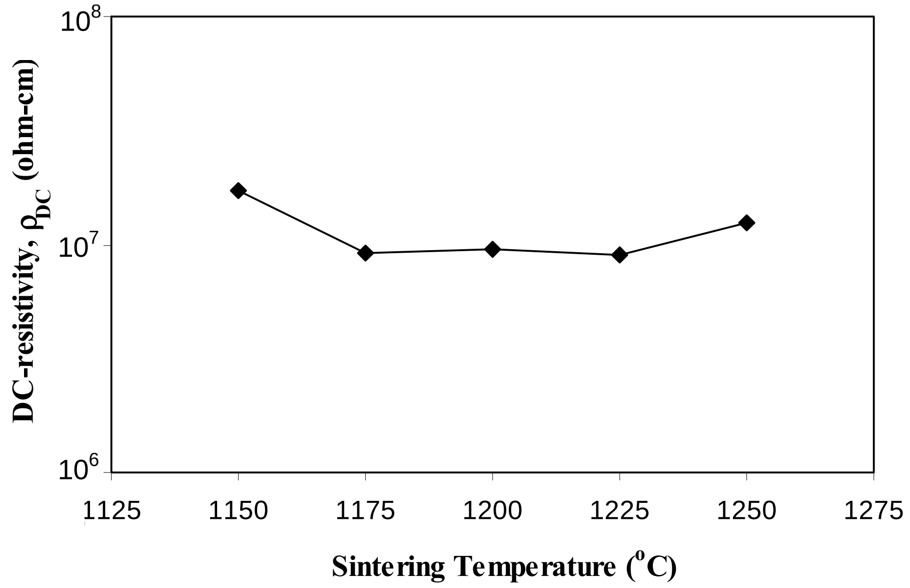

Figure 4.13 Variation in DC-resistivity with sintering temperature.

4.3.4.2 Initial Magnetic Permeability, μ_i

Measurements on initial magnetic permeability were performed on toroid ceramics according to the procedure as described in Section 3.3.5.2. μ_i was determined from Equation 3.8 by using the data presented in Table 4.5. The variation in μ_i with peak sintering temperature is shown in Figure 4.14. As seen from the graph, μ_i increased slightly with increasing sintering temperature.

Table 4.5 Outer diameter (D_{out}), inner diameter (D_{in}), thickness (t) and initial magnetic permeability (μ_i) of NF toroids.

Sample Designation	D_{out} (mm)	D_{in} (mm)	t (mm)	μ_i
NF-1150	19.53	8.09	5.00	9.68
NF-1175	19.32	7.95	4.95	9.73
NF-1200	19.12	7.92	4.85	10.34
NF-1225	18.88	7.76	4.40	10.23
NF-1250	18.64	7.73	4.57	10.95

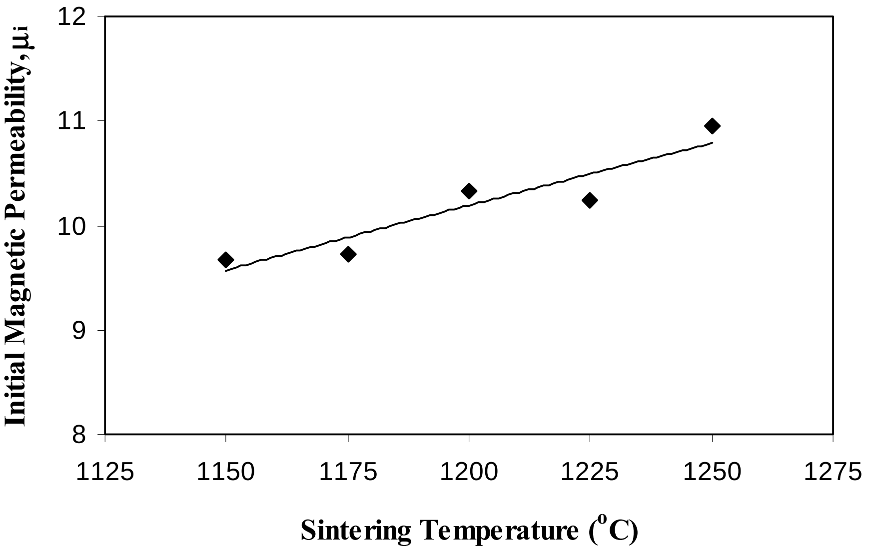

Figure 4.14 Variation in initial magnetic permeability with sintering temperature.

4.3.4.3 Magnetostriction, λ

Magnetostriction measurements were performed by following the procedure as described in Section 3.3.5.3. These measurements were based on determination of dimensional change in the sintered ferrites as a function of the externally applied magnetic field. The data on displacements are listed in Appendix A. Table A.1 involves transverse displacements, whereas Table A.2 summarizes the data on longitudinal magnetostriction. It is also worthy to mention that the strain values obtained through the mentioned procedure had an experimental error of ±0.5 ppm strain.

The change in longitudinal and transverse magnetostriction of NF ceramics with applied field strength is displayed in Figure 4.15. As noticed from the figure, ceramics attained saturation strain at a field of 1250 Oe. Negative values of longitudinal magnetostriction implied contraction of nickel ferrite ceramics in the direction of the applied field.

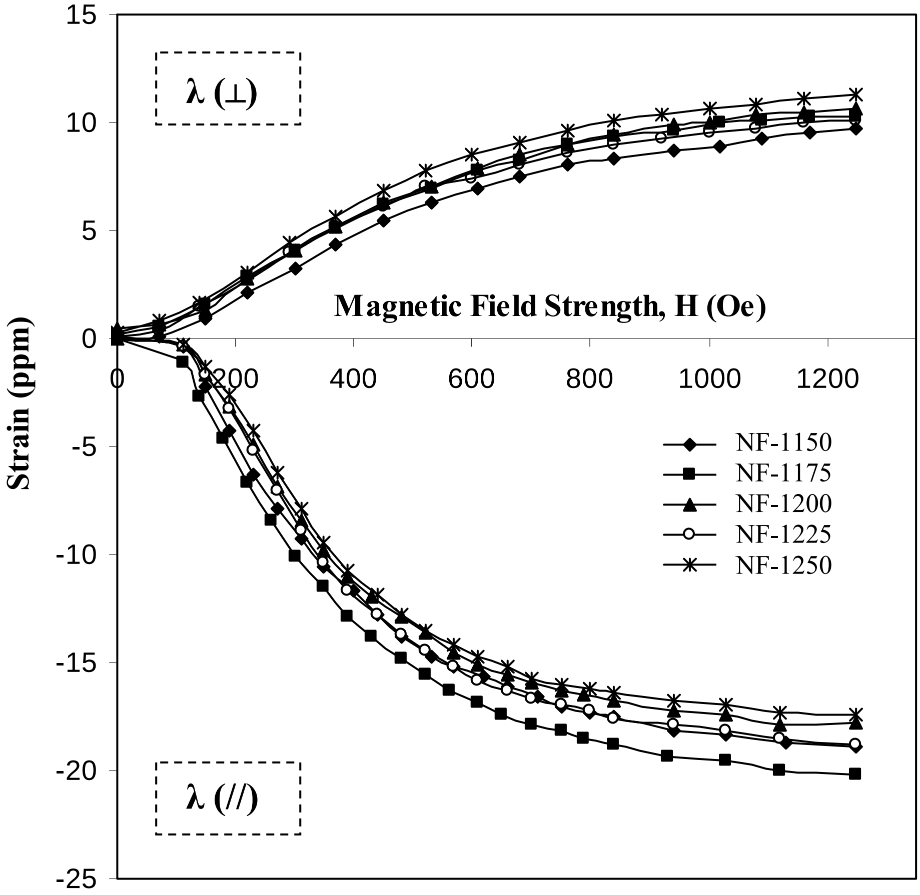

Figure 4.15 Variation in longitudinal magnetostriction, λ(//), and transverse magnetostriction, λ(⊥), with magnetic field strength for NF ceramics soaked at various temperatures.

4.3.5 Effects of Bismuth Addition

In order to improve densification in magnetostrictive ceramics, the NF powder was doped with Bi_2O_3 which served as a sintering aid. Amount of Bi_2O_3 was selected as 0.5, 1, 2, and 3 wt%. Bismuth doped ceramics were sintered only at a soaking temperature of 1250 °C for 2 h.

Modification of magnetostrictive ceramics with Bi_2O_3 not only improved the densification characteristics of NF ceramics but also enhanced electrical and magnetic properties as will be discussed in the following sections.

4.3.5.1 XRD of Bismuth Modified NF Ceramics

XRD patterns of NF ceramics sintered in the presence of Bi_2O_3 are displayed in Figure 4.16. All diffraction peaks were representative of the nickel ferrite compound. No second phase formation was detected, implying the complete dissolution of bismuth in the spinel lattice. Bi_2O_3 modification did not cause a measurable shift in the main XRD peak positions.

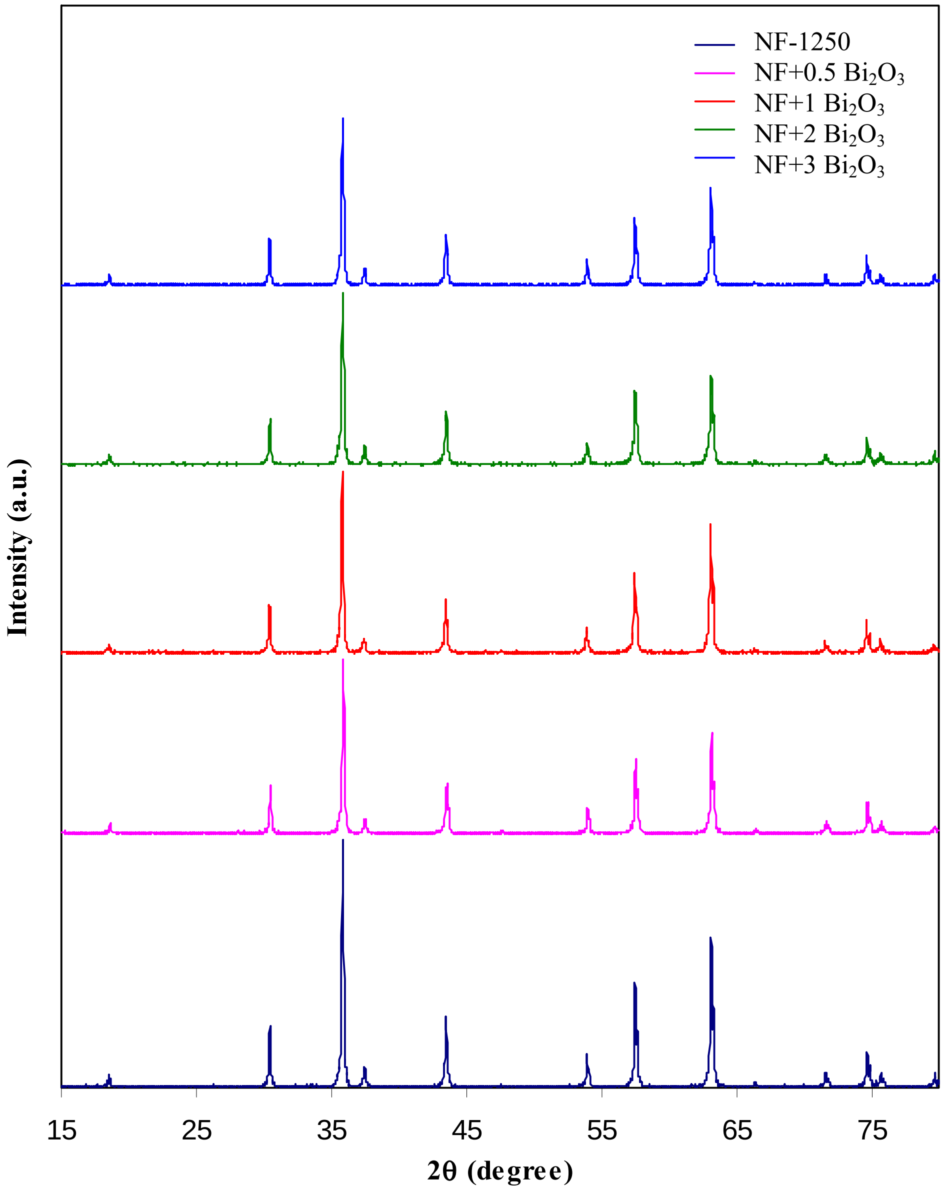

Figure 4.16 XRD patterns of NF ceramics modified with Bi_2O_3. Ceramics were soaked at 1250 °C for 2 h.

4.3.5.2 Sintered Density

Data on sintered density of NF ceramics modified with Bi_2O_3 are given in Table 4.6. The last column in the table is included to show the improvement attained in the level of densification by Bi_2O_3 addition. In the calculation of %TD values, theoretical density was taken as that of the pure NF ceramic, i.e., 5.313 g/cm^3.

Table 4.6 Experimental and %TD densities of NF ceramics modified by Bi_2O_3.

Sample Designation	ρ_{exp} (g/cm^3)	%TD
NF-1250	4.305	80.95
NF+0.5 Bi_2O_3	5.098	95.81
NF+1 Bi_2O_3	5.176	97.49
NF+2 Bi_2O_3	5.183	97.50
NF+3 Bi_2O_3	5.159	97.06

All NF ceramics containing bismuth sintered to almost theoretical density, as revealed from the table.

4.3.5.3 Microstructural Features

Presence of bismuth had a significant effect on microstructures of NF ceramics as noticed in the SEM images illustrated in Figures 4.17 and 4.18. Average grain size of NF ceramics increased from 4 µm to 12 µm with the addition of 0.5 wt% Bi_2O_3. Grains enlarged gradually with bismuth concentration. Average size was estimated as 18 µm when ceramics were modified with 3 wt% Bi_2O_3. Evidently, the amount of porosity decreased with increasing grain size.

The dopant bismuth was distributed homogeneously throughout the microstructure according to the EDS X-ray mapping in Figure 4.19. It was also located at grain boundaries and at triple junctions in the microstructure as observed from the back scattered electron (BSE) image and the supplementary EDS pattern in Figure 4.20.

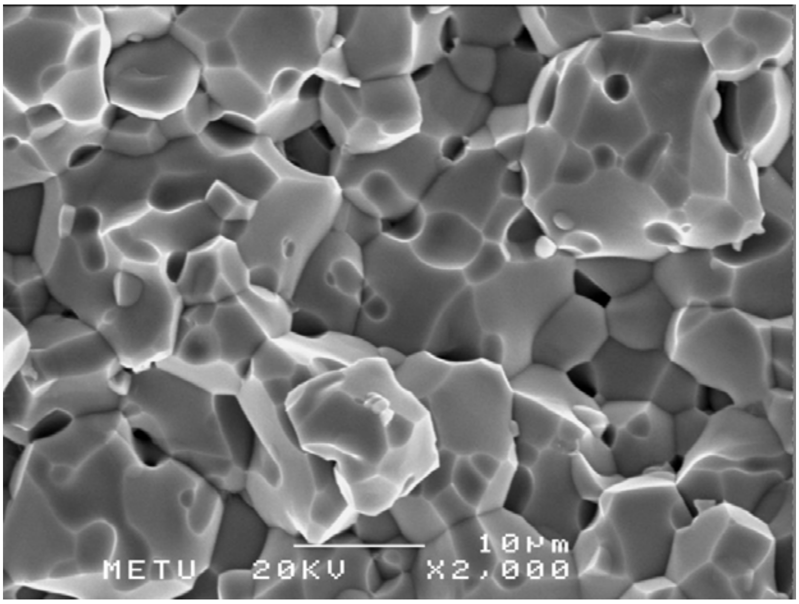

Figure 4.17 SEM fractograph of the NF ceramic modified with 0.5 wt% Bi_2O_3. Ceramic was soaked at 1250 °C for 2 h.

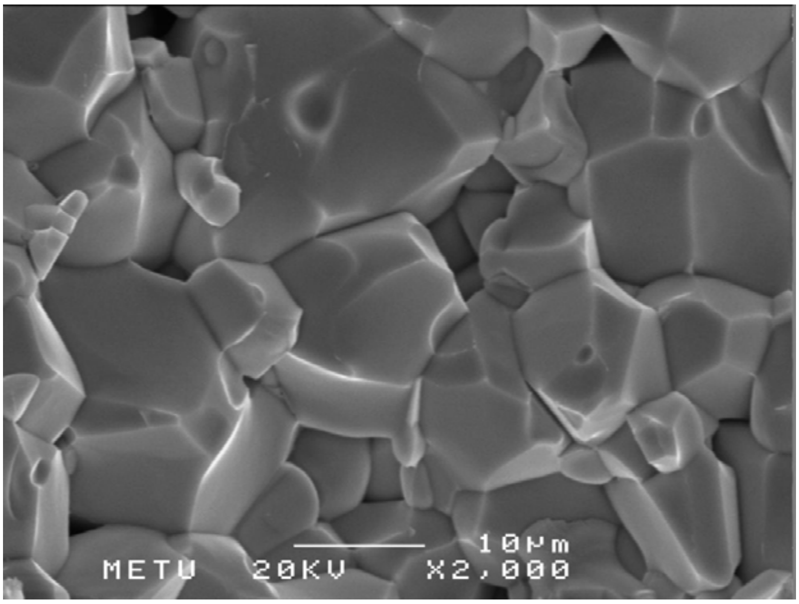

Figure 4.18 SEM fractograph of the NF ceramic modified with 3 wt% Bi_2O_3. Ceramic was soaked at 1250 °C for 2 h.

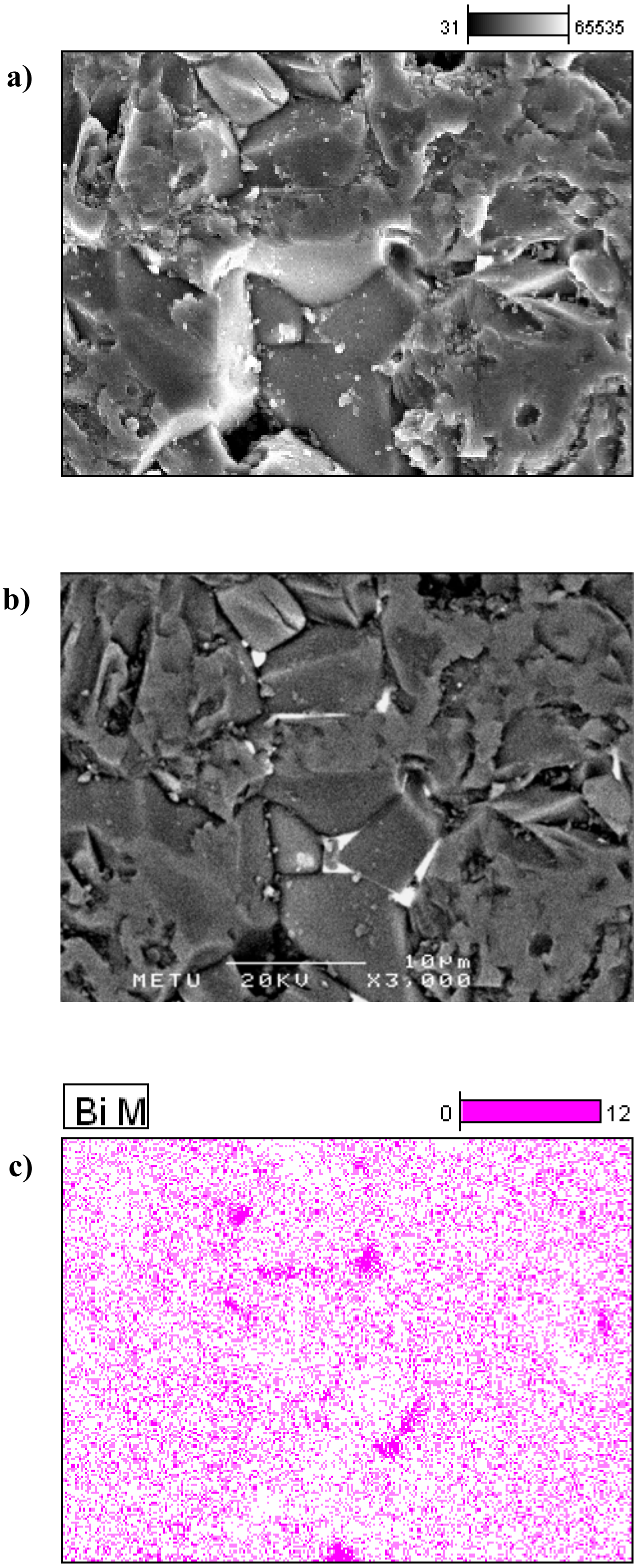

Figure 4.19 a) Secondary electron image in EDS X-Ray mapping, b) BSE image, and c) Bi distribution throughout the microstructure in EDS X-Ray mapping of the NF ceramic modified with 3 wt% Bi_2O_3.

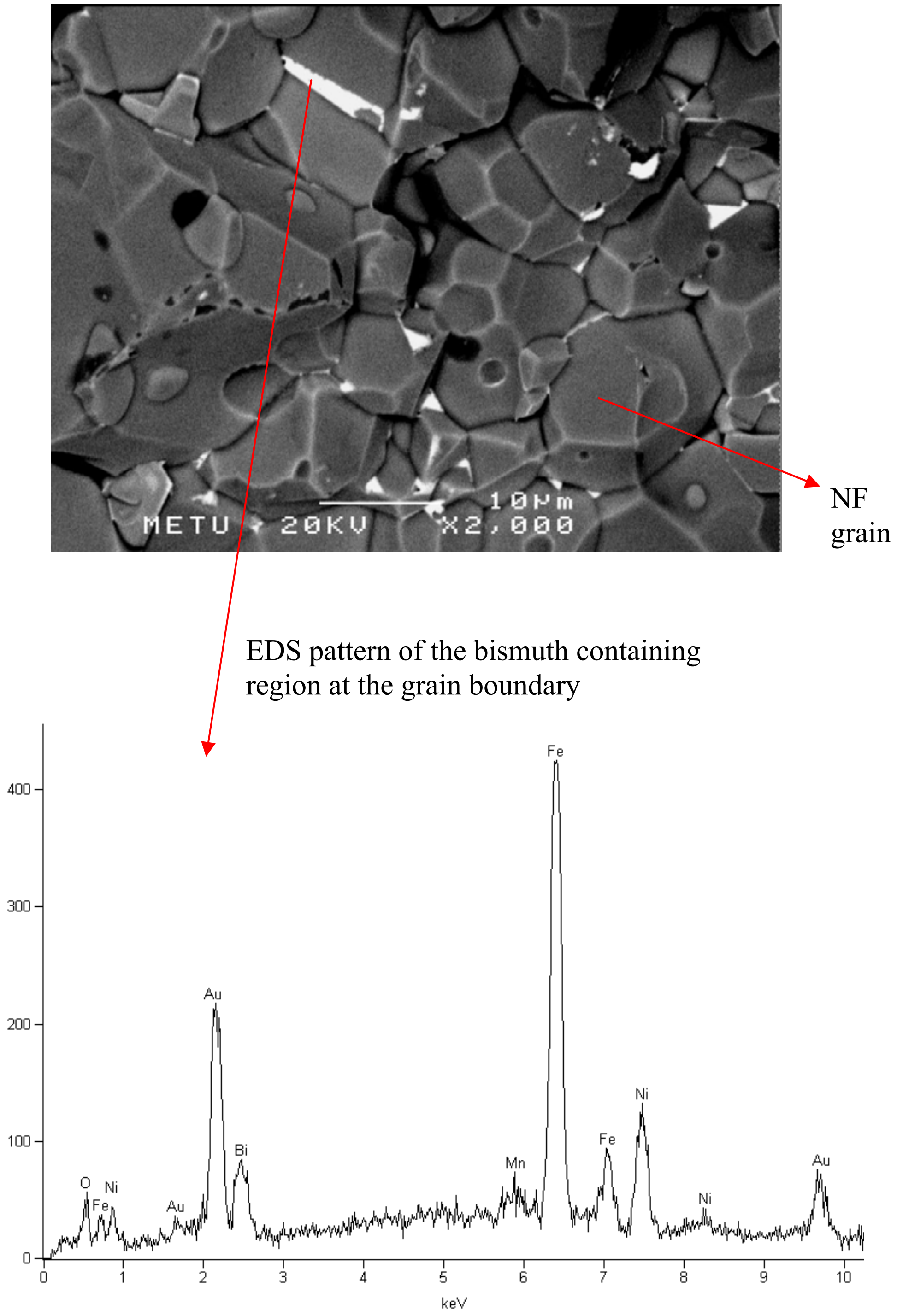

Figure 4.20 BSE image of the NF ceramic modified with 3 wt% Bi_2O_3 and the EDS pattern of the bismuth containing region at the grain boundary.

4.3.5.4 Electrical and Magnetic Properties

4.3.5.4.1 Electrical Resistivity, ρ_{DC}

The data regarding dimensional parameters, electrical resistance and DC-resistivities of Bi_2O_3 modified NF ceramics are tabulated in Table 4.7.

Table 4.7 Values of diameter (D), thickness (t), resistance (R), and DC-resistivity (ρ_{DC}) of Bi_2O_3 modified NF ceramics. Ceramics were soaked at 1250 °C for 2 h.

Sample Designation	**D (mm)**	**t (mm)**	**R (ohm)**	**ρ (ohm-cm)**
NF+0.5 Bi_2O_3	11.21	3	1.94×10^7	6.59×10^7
NF+1 Bi_2O_3	11.04	3	3.47×10^7	1.15×10^8
NF+2 Bi_2O_3	11.00	3	1.16×10^7	3.81×10^7
NF+3 Bi_2O_3	10.93	3	6.02×10^6	1.95×10^7

The variation in the DC-resistivity with Bi_2O_3 concentration is represented graphically in Figure 4.21. As revealed from the graph, ρ_{DC} increased an order of magnitude when 1 wt% Bi_2O_3 was added. The reason of this increase would be attributed to the highly resistive Bi_2O_3 at the grain boundaries. ρ_{DC} decreased with further Bi_2O_3 addition. The reduction would be due to increased grain size and oxidation tendency of Bi^{3+} ions to Bi^{5+} ions which promotes the formation of Fe^{2+} ions, as will be discussed in the following chapter.

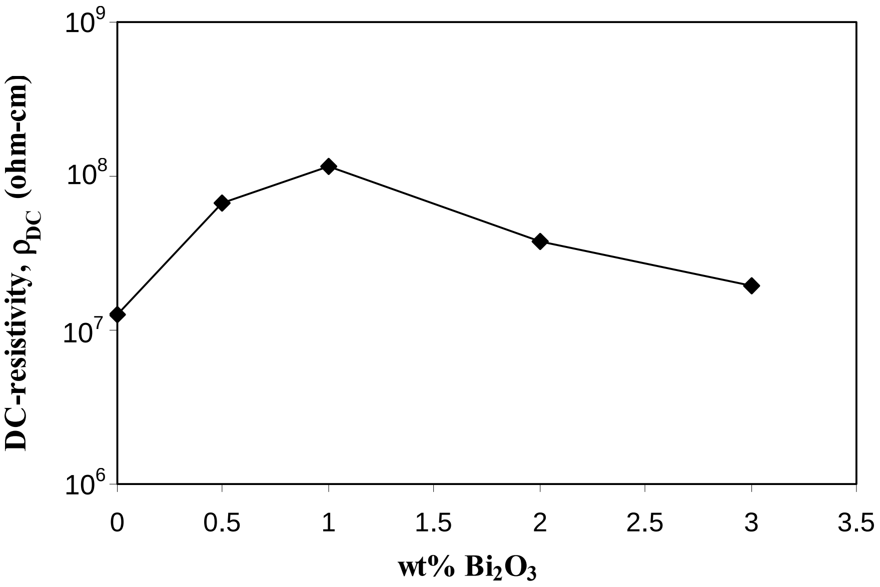

Figure 4.21 Variation in DC-resistivity with Bi_2O_3 concentration. Ceramics were soaked at 1250 °C for 2 h.

4.3.5.4.2 Initial Magnetic Permeability, μ_i

Data obtained throughout the measurements on initial magnetic permeability of ferrites doped with bismuth are tabulated in Table 4.8.

Table 4.8 Outer diameter (D_{out}), inner diameter (D_{in}), thickness (t) and initial magnetic permeability (μ_i) of Bi_2O_3 modified NF toroids.

Sample Designation	D_{out} (mm)	D_{in} (mm)	t (mm)	μ_i
NF+0.5 Bi_2O_3	17.62	7.30	4.70	20.57
NF+1 Bi_2O_3	17.53	7.25	4.34	21.99
NF+2 Bi_2O_3	17.53	7.20	4.59	20.50
NF+3 Bi_2O_3	17.30	7.10	4.79	18.79

Variation in initial magnetic permeability with Bi_2O_3 concentration is displayed in Figure 4.22. As seen from the graph, μ_i increased to twice of its value in the pure

NF ceramic. Maximum permeability was attained at 1 wt% Bi_2O_3 addition. Enhancement in μ_i values was assigned to the increase in grain size. μ_i decreased slightly when ceramics were modified with 2 and 3 wt% Bi_2O_3 due to the increased concentration of non-magnetic phase in the structure.

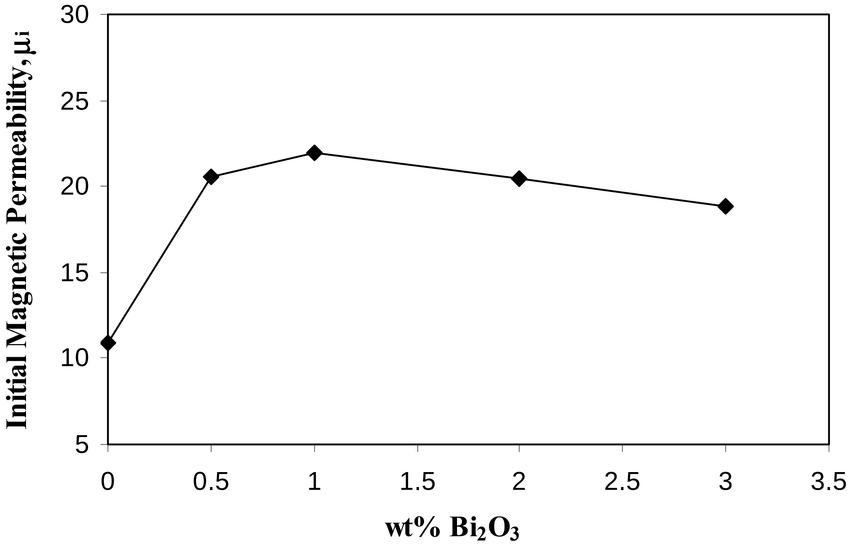

Figure 4.22 Variation in initial magnetic permeability with Bi_2O_3 concentration.

4.3.5.4.3 Magnetostriction, λ

Transverse and longitudinal magnetostriction data obtained throughout the measurements are tabulated in Table A.3 and Table A.4 of Appendix A, respectively. Variation in magnetostriction with magnetic field strength for different levels of Bi_2O_3 addition is displayed in Figure 4.23. Ceramics attained almost full magnetic saturation in a field of 1250 Oe, just like pure NF ceramics. As noticed from the graph, NF ceramics sintered in the presence of Bi_2O_3 exhibited larger magnetostriction when compared to bismuth free ceramics. Highest longitudinal and transverse magnetostriction was attained in ceramics having 1 wt% Bi_2O_3. Magnetostriction decreased upon further Bi_2O_3 additions.

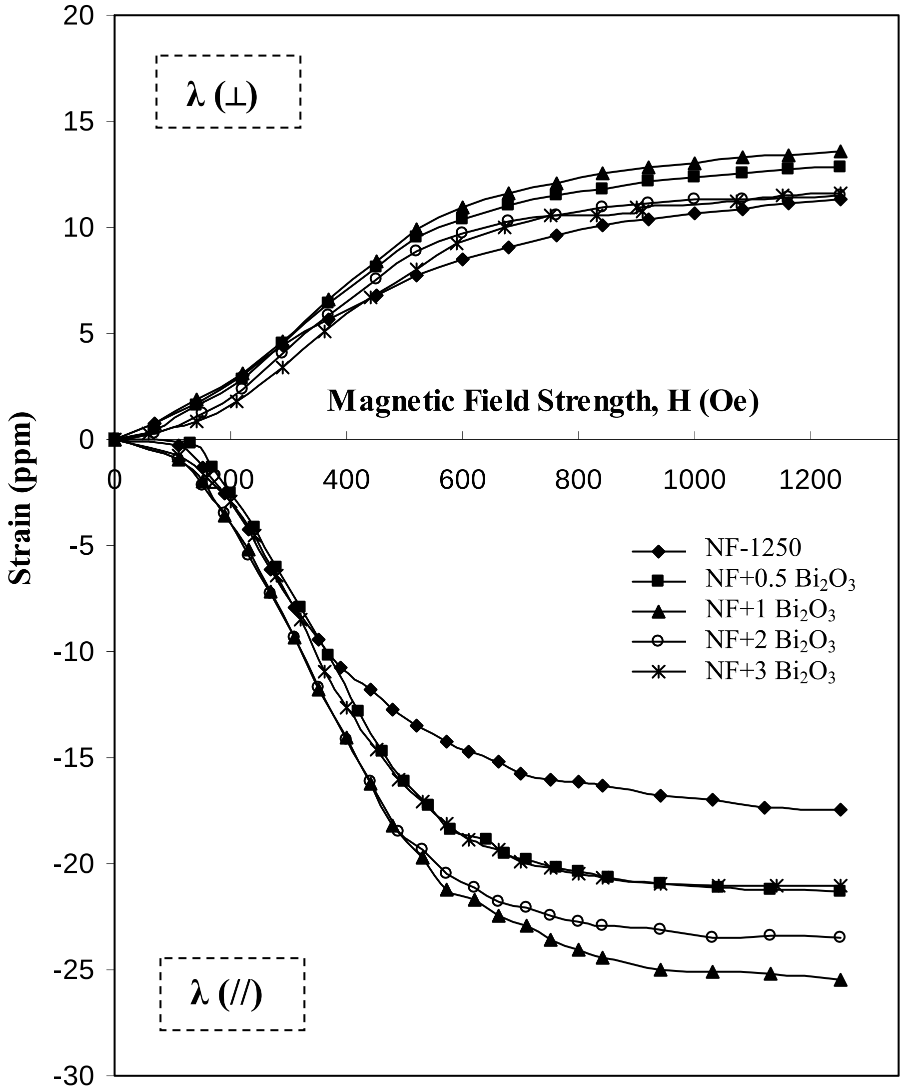

Figure 4.23 Variation in longitudinal magnetostriction, λ(//), and transverse magnetostriction, λ(⊥), with magnetic field strength for bismuth modified NF ceramics.

4.4 Data and Results on Bulk ME Composites

4.4.1 XRD of Sintered Bulk ME Composites

Phases within the bulk ME composites were evaluated by XRD studies. XRD patterns of bulk ME composites comprised of 10 wt% NF and 90 wt% PSZT are displayed in Figure 4.24. Diffraction peaks of constituent piezoelectric and magnetostrictive phases are labeled on the patterns. No extraneous phase was detected in the patterns. The peaks of the NF phase were rather shallow due to the smaller concentration of NF in the composite. When NF concentration in the composite was increased from 10 to 20 wt%, number of diffraction peaks belonging to the NF phase and intensity of the peaks increased, as revealed from Figure 4.25.

Theoretical density of bulk ME composites were calculated from the rule of mixture expressed by the following relationship:

$$\frac{1}{\rho_c} = \frac{M_{f,PSZT}}{\rho_{PSZT}} + \frac{M_{f,NF}}{\rho_{NF}} \tag{4.4}$$

where ρ_c: theoretical density of the composite ceramic, g/cm^3

$M_{f,PSZT}$: mass fraction of the PSZT powder

ρ_{PSZT}: theoretical density of the PSZT phase, g/cm^3

$M_{f,NF}$: mass fraction of the NF powder

ρ_{NF}: theoretical density of the NF phase, g/cm^3

Lattice parameters of the constituent phases were essentially the same with those in their pure forms. Therefore, theoretical density of PSZT and NF phases within the composite were taken as 7.957 g/cm^3 and 5.313 g/cm^3, respectively.

Theoretical density of the composite ceramics designated as 10N-90P, 15N-85P and 20N-80P were calculated from Equation 4.4 as 7.579 g/cm^3, 7.404 g/cm^3 and 7.237 g/cm^3, respectively.

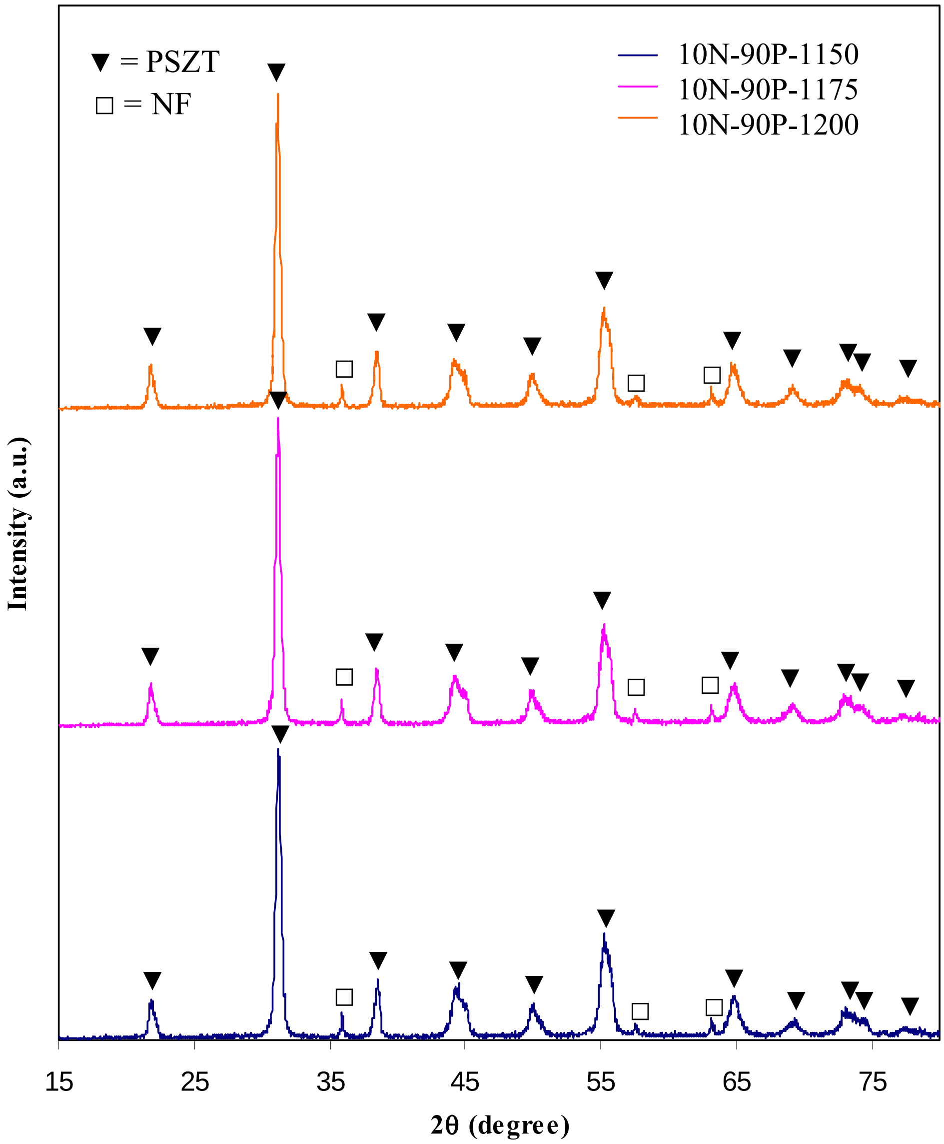

Figure 4.24 XRD patterns of 10N-90P bulk ME composites ceramics. Ceramics were soaked between 1150 to 1200 °C for 2 h.

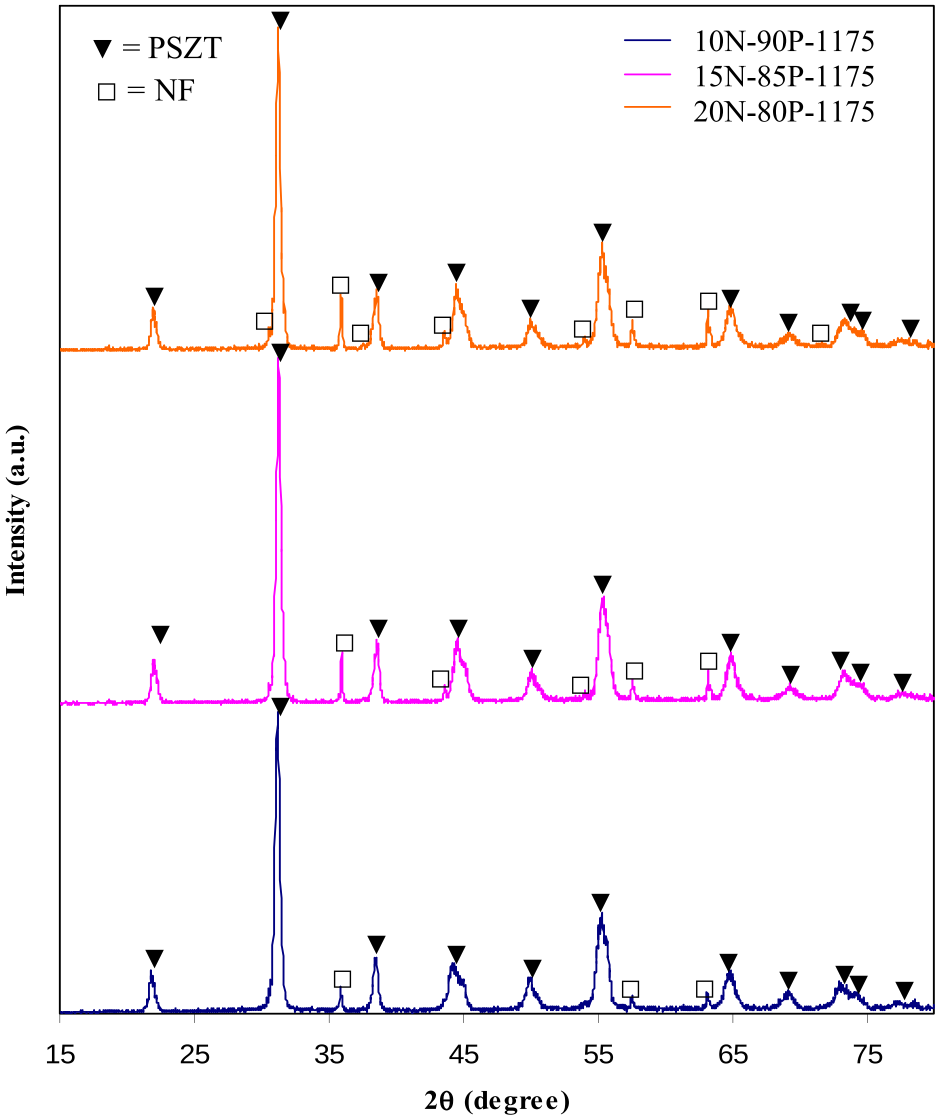

Figure 4.25 XRD patterns of bulk ME composites having different compositions. Ceramics were soaked at 1175 °C for 2 h.

4.4.2 Sintered Density

Density of sintered bulk ME composites are listed in Table 4.9. The composite consisting of 10 wt% NF and 90 wt% PSZT was densified more than its individual components.

Table 4.9 Experimental and %TD densities of bulk ME composites.

Sample Designation	**ρ_{exp} (g/cm^3)**	**%TD**
10N-90P-1150	6.774	89.38
10N-90P-1175	7.255	95.73
10N-90P-1200	7.373	97.28
15N-85P-1175	5.293	71.50
20N-80P-1175	5.141	71.03

The increase in %TD values of the composites was attributed to the liquid phase formation during sintering. Apparently, the liquid phase was developed by the dissolution of NF in PSZT. In fact, the composite sintered at 1225 °C fused to the saggar due to melt formation.

The composites containing higher proportions of NF were sintered at 1175 °C in order to avoid or minimize liquid phase formation. But, at this sintering temperature, a considerable decrease in densification was observed upon increasing the NF content of the composite. The sintered density of bulk ME composites containing 15 or 20 wt% NF was only about 71 % of the theoretical.

4.4.3 Microstructural Features

Microstructural analyses were performed by examining the fractured surfaces. BSE images were instrumental in observing the distribution of NF particles within the PSZT matrix. SEM fractographs and BSE images are presented in Figures 4.26 through 4.35.

Figure 4.26 shows the SEM fractograph taken from the green (unfired) 10N-90P composite. As seen in the BSE image shown in Figure 4.27, the NF particles were surrounded by PSZT particles. Uniform distribution of constituent phases was attained as a result of mixing in the ball mill.

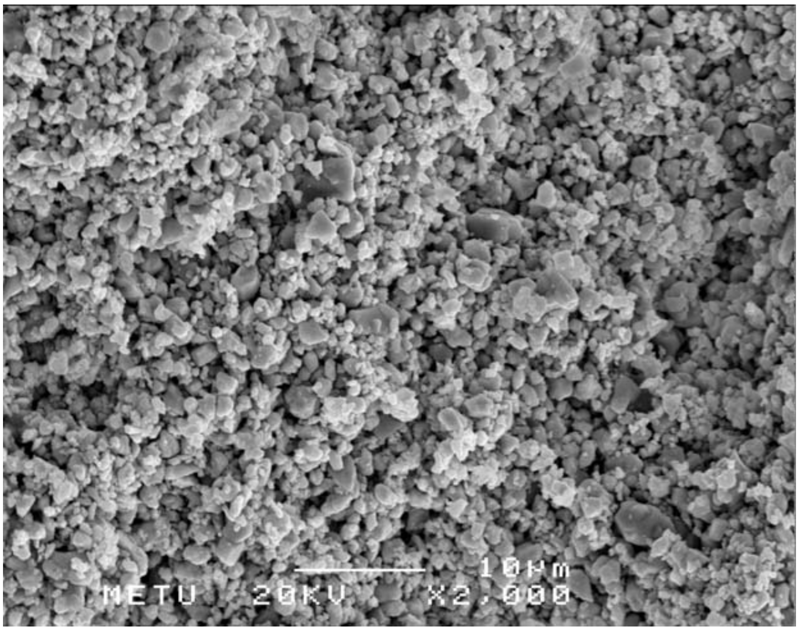

Figure 4.26 SEM fractograph of the 10N-90P green bulk ME composite.

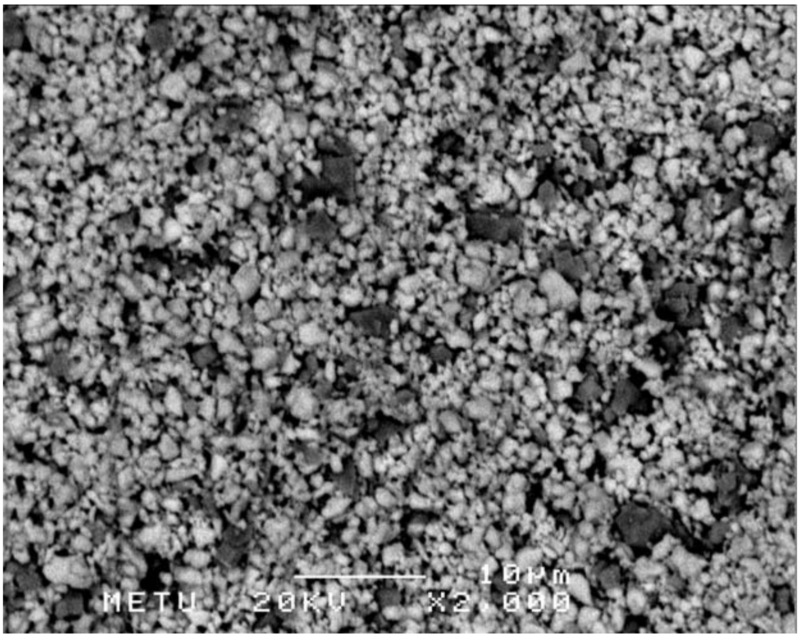

Figure 4.27 BSE image of the 10N-90P green bulk ME composite.

Figure 4.28 displays the microstructure of the 10N-90P composite sintered at 1150 °C for 2 h. The BSE image of the same section is shown in Figure 4.29. These images revealed that, NF, both in fine and coarse form, was dispersed in the PSZT matrix. The coarse NF particles preserved their cubic spinel structure.

Porosity in sintered composites diminished due to enhanced sintering activity at higher soaking temperatures. Figures 4.30 and 4.31 are SEM images belonging to the 10N-90P composite sintered at 1175 °C. The broken surface yielded a chonchoidal outlook due to increased bonding between particles of the PSZT phase.

SEM image of the composite sintered at 1200 °C is shown in Figure 4.32. The sintered density was quite high evidenced by the low level of porosity. In the BSE image of the same section as shown in Figure 4.33, the size of the NF particles became smaller probably due to their partial dissolution in the PSZT matrix.

Examples to the microstructure of a bulk composite prepared with a greater proportion of the ferrite phase but sintered at 1175 °C are shown in Figures 4.34 and 4.35. The poor level of densification was manifested in the grain size of the constituent phases which remained as small as the original particle size in the unfired green form.

BSE images of the bulk ME composites captured at lower magnifications are presented in Figures B.1 through B.6 of Appendix B in order to show distribution of NF particles within the PSZT matrix.

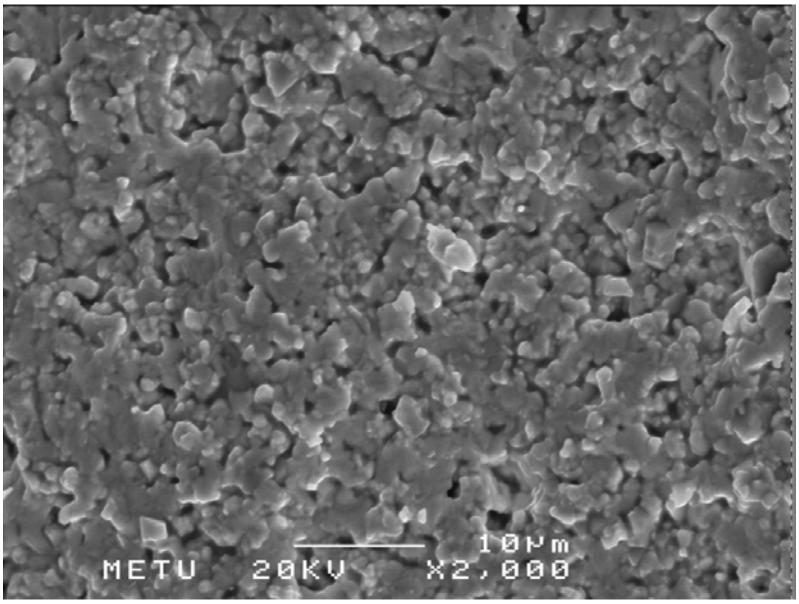

Figure 4.28 SEM fractograph of the 10N-90P ceramic sintered at 1150 ºC for 2 h.

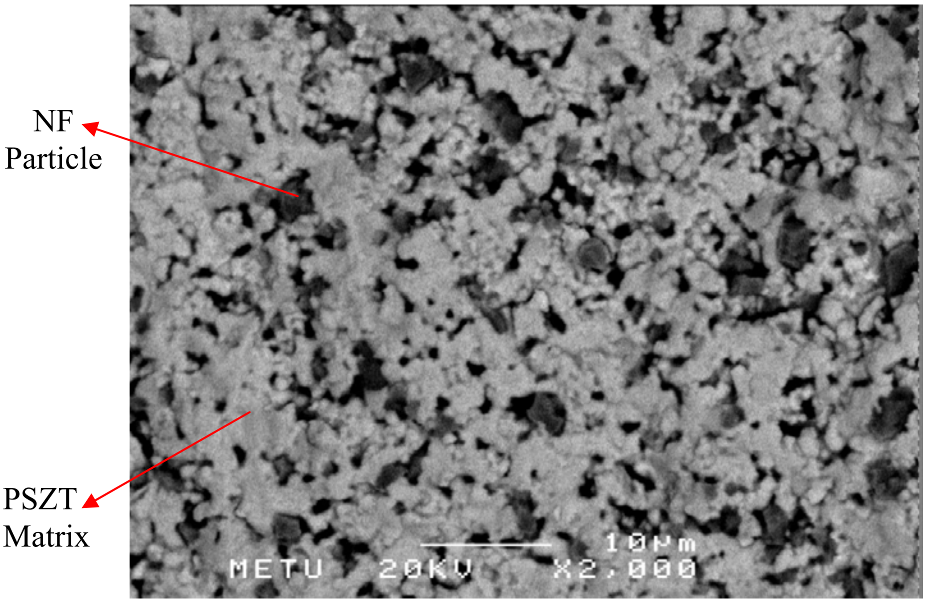

Figure 4.29 BSE image of the 10N-90P ceramic sintered at 1150 ºC for 2 h.

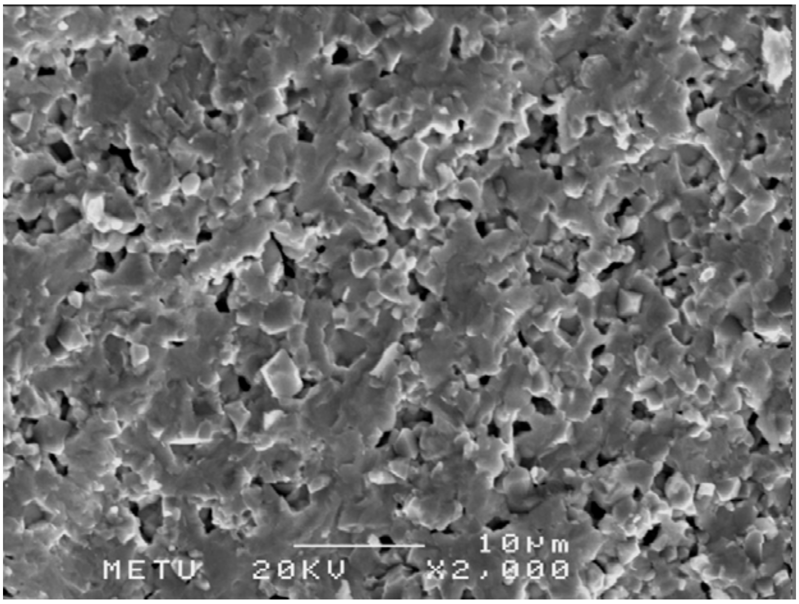

Figure 4.30 SEM fractograph of the 10N-90P ceramic sintered at 1175 ºC for 2 h.

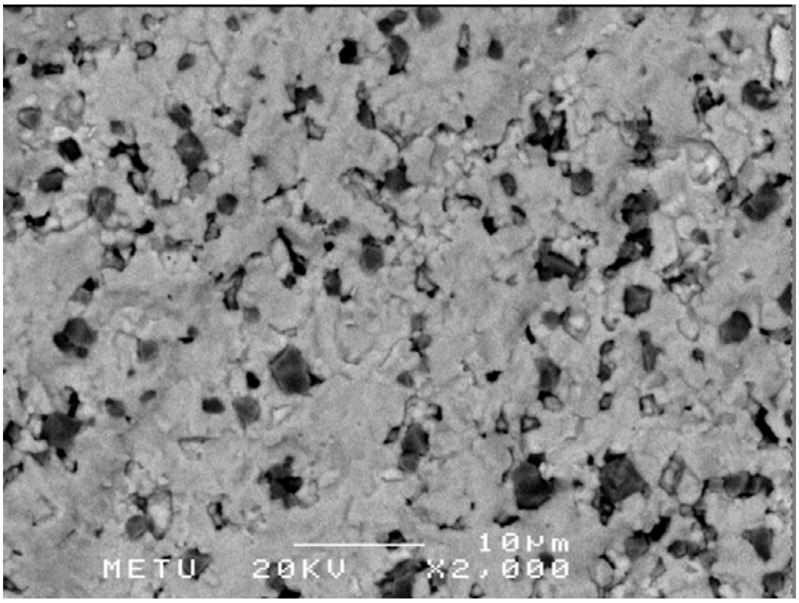

Figure 4.31 BSE image of the 10N-90P ceramic sintered at 1175 ºC for 2 h.

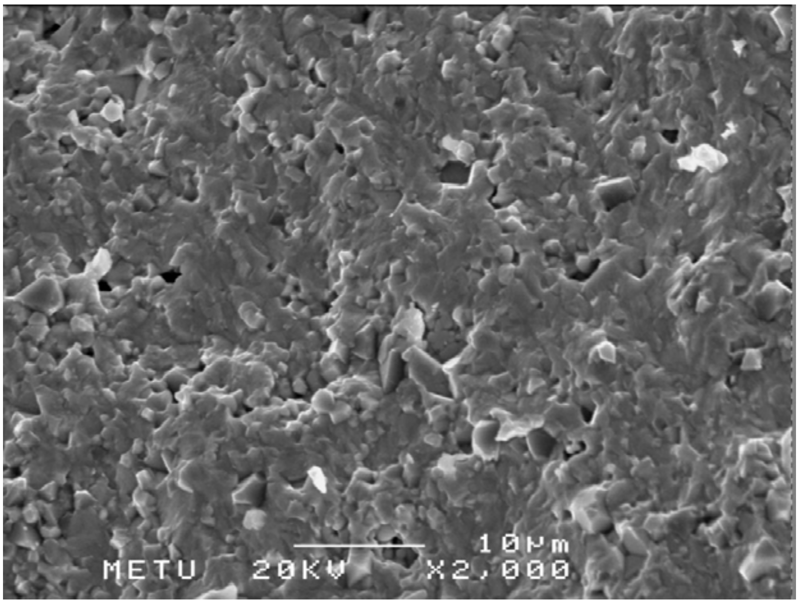

Figure 4.32 SEM fractograph of the 10N-90P ceramic sintered at 1200 ºC for 2 h.

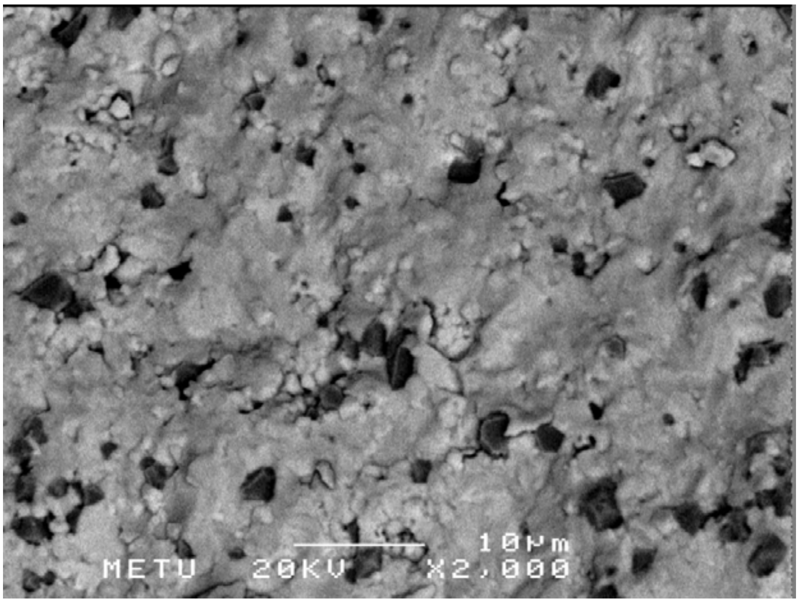

Figure 4.33 BSE image of the 10N-90P ceramic sintered at 1200 ºC for 2 h.

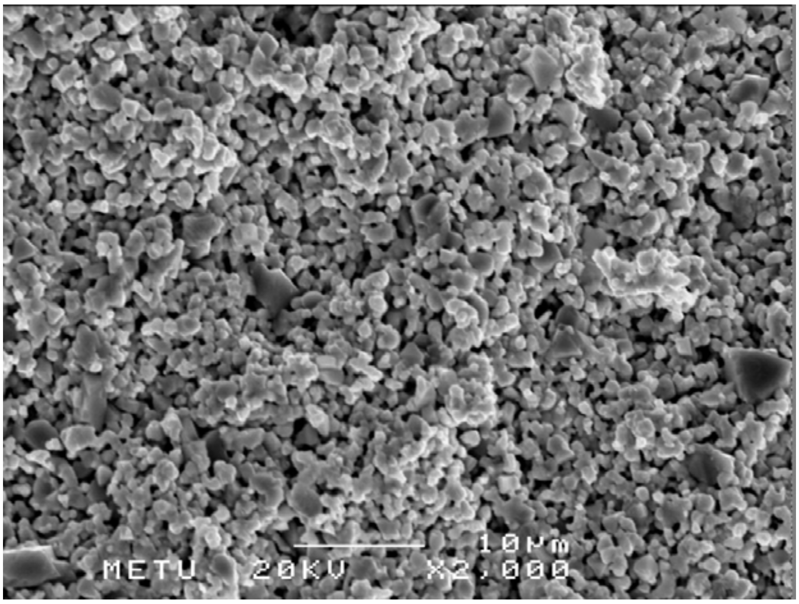

Figure 4.34 SEM fractograph of the 15N-85P ceramic sintered at 1175 ºC for 2 h.

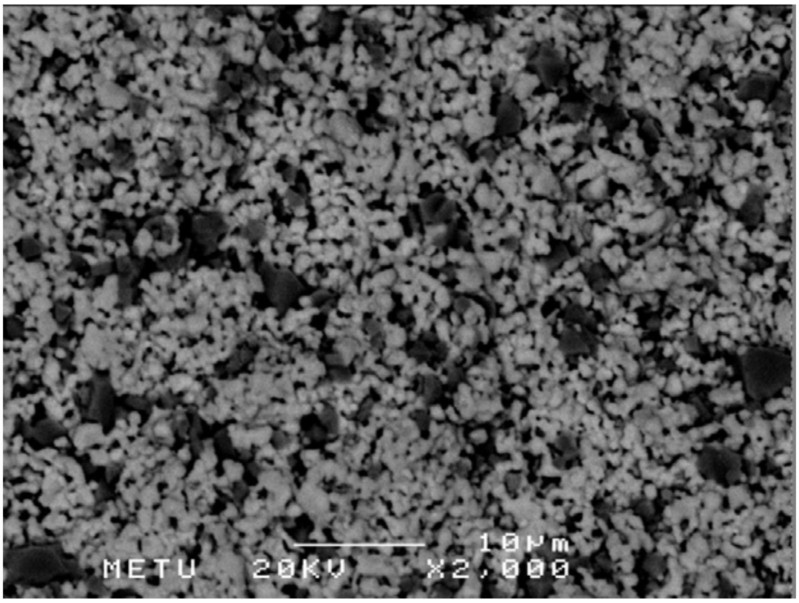

Figure 4.35 BSE image of the 15N-85P ceramic sintered at 1175 ºC for 2 h.

4.4.4 Dielectric and Piezoelectric Properties

Dielectric and piezoelectric properties of bulk ME composites were determined by following the procedure outlined in Section 3.3.4. The data obtained throughout the measurements are given in Table 4.10.

Graphical representations of the piezoelectric data are shown in Figure 4.36. As seen in this graph, the piezoelectric strain coefficient of 10N-90P composite did not vary much with sintering temperature. d_{33} values of the composites were considerably lower than those of the pure PSZT ceramics sintered at the same temperatures. The mechanical quality factor increased upon soaking the composites at higher temperatures. Q_m values of the composites were larger than those of the pure PSZT ceramics. This was an indication that the piezoelectric nature of the PSZT in the composite turned towards the "hard" type. This might be linked to the migration of iron ions from NF to PSZT.

Variation in dielectric constant and loss tangent of 10N-90P composites with sintering temperature are displayed in Figure 4.37. Dielectric constant increased with increasing soaking temperature while loss tangent values decreased. Higher loss values were observed for composites when compared to pure PSZT ceramics. Dielectric constants were lower than those of pure PSZT ceramics.

The presence of ferrite within the PSZT matrix created a low resistivity path, which in turn limited the applied electric field during the poling process to about 2 kV/mm for 10N-90P composites. In 15N-85P and 20N-80P composites, poling was possible only up to 1.25 kV/mm. The piezoelectric strain coefficient of these composites attained a very low value of 0.08 pC/N. This implied that piezoelectric activity could not be developed in bulk ME composites having more than 10 wt% NF.

Table 4.10 Values of diameter (D), thickness (t), capacitance (C), dielectric constant (K^T), loss tangent (tanδ), piezoelectric strain coefficient (d_{33}), anti-resonance frequency (f_a), resonance frequency (f_r), planar coupling coefficient (k_p), resistance (R) and capacitance (C_a) elements of the equivalent circuit and mechanical quality factor (Q_m) of bulk ME composite ceramics. Dielectric properties were measured at 1 kHz frequency.

Sample Designation	**D (mm)**	**t (mm)**	**C (pF)**	**K^T**	**tanδ**	**d_{33} (pC/N)**	**f_a (Hz)**	**f_r (Hz)**	**$\Delta f/f_r$**	**k_p**	**R (Ω)**	**C_a (pF)**	**Q_m**
10N-90P-1150	11.23	1	538.77	615	0.021	132	200696	197983	0.014	-	218.88	13.48	279
10N-90P-1150	11.21	1	559.90	641	0.024	104	202413	200388	0.010	-	318.49	9.69	268
10N-90P -1175	10.92	1	612.90	740	0.017	120	223463	219508	0.018	- -	113.50	20.07	327
10N-90P -1175	10.93	1	607.94	733	0.020	121	224417	220488	0.018	-	120.70	19.87	307
10N-90P -1200	10.85	1	631.74	772	0.014	106	229604	226000	0.016	- -	108.37	18.34	367
10N-90P -1200	11.08	1	611.48	717	0.016	129	227013	222583	0.020	-	104.94	21.41	331

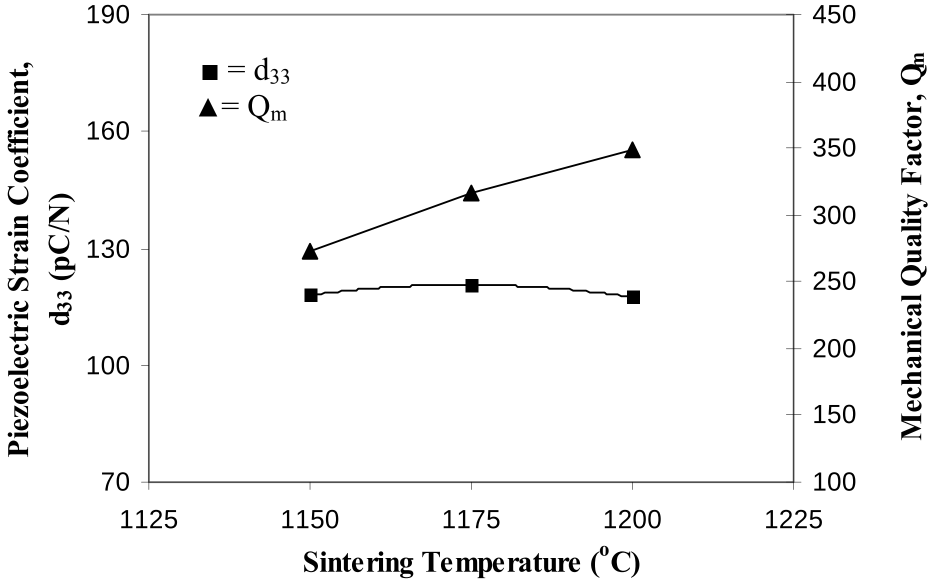

Figure 4.36 Variation in piezoelectric strain coefficient and mechanical quality factor of 10N-90P composites with sintering temperature.

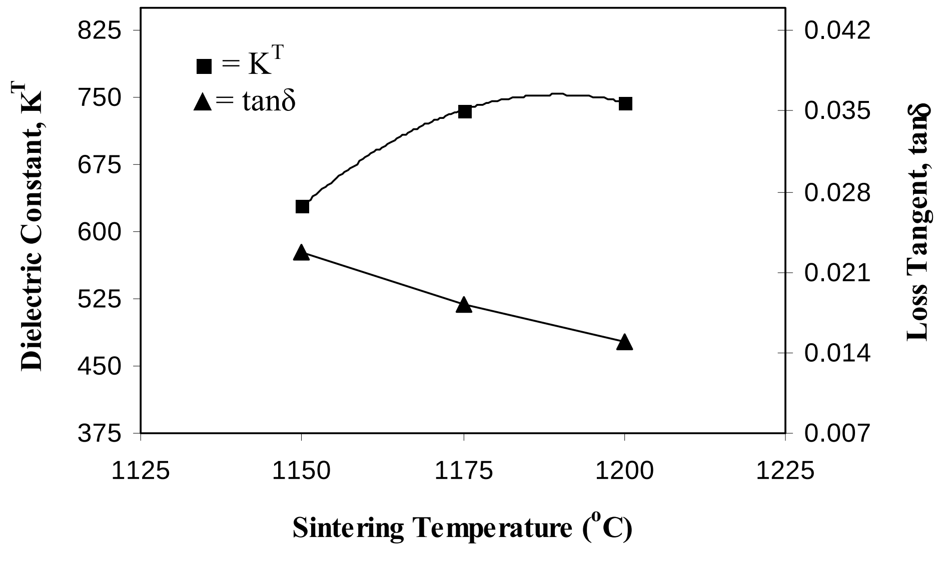

Figure 4.37 Variation in dielectric constant and loss tangent of 10N-90P composites with sintering temperature.

4.4.5 Magnetostriction, λ

Magnetostriction determinations were performed on 10N-90P bulk ME composites soaked at various temperatures. The measurements had an error of ±0.5 ppm strain, thus small differences in the λ values could not be detected. Transverse magnetostriction values of the composites were in the range of 2 ppm. Hence, in Figure 4.38, only the longitudinal magnetostriction data is displayed but transverse data is not shown due to unreliability of values. Longitudinal magnetostriction was accepted as 3.5 - 4 ppm and remained almost unchanged for all 10N-90P composites soaked at various temperatures.

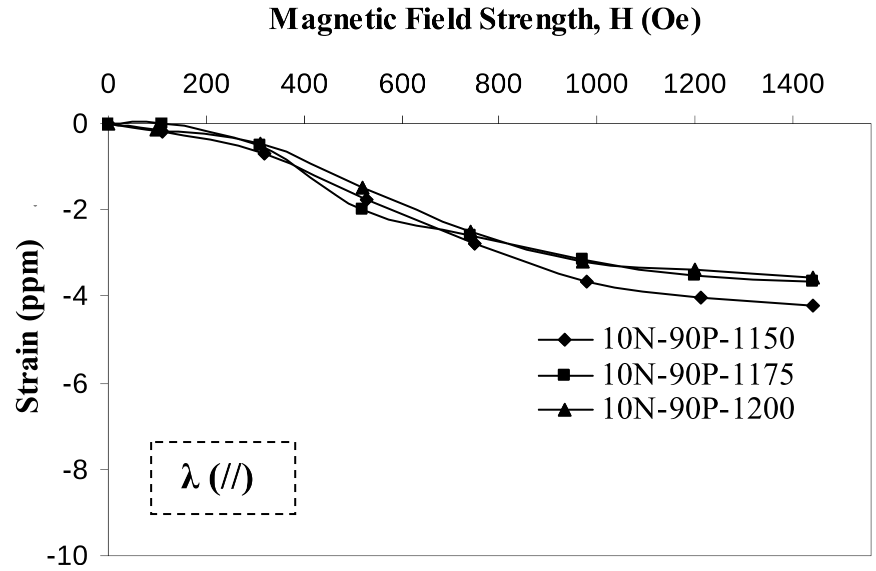

Figure 4.38 Variation in longitudinal magnetostriction, λ(//), with magnetic field strength for 10N-90P composites soaked at various temperatures.

4.4.6 ME Effect

Magnetoelectric output of 10N-90P composites was determined by following the procedure as described in Section 3.5.6. Data collected during measurements are given in Table 4.11. Supplementary oscilloscope screen images obtained as an evidence for electrical output are shown in Figures C.1 through C.3 in Appendix C.

Table 4.11 Values of applied magnetic field (H), voltage output (V) and ME output (dE/dH) of 10N-90P composites.

H (Oe)	**10N-90P-1150**		**10N-90P-1175**		**10N-90P-1200**	
	V (μV)	**dE/dH (μV/cm·Oe)**	**V (μV)**	**dE/dH (μV/cm·Oe)**	**V (μV)**	**dE/dH (μV/cm·Oe)**
800	37500	46.875	40500	50.625	43750	54.688
1030	56250	54.612	62500	60.680	68750	66.748
1280	75000	58.594	81250	63.477	93750	73.242
1520	87500	57.566	93750	61.678	106200	69.868
1750	87500	50.000	93750	53.571	106200	60.686
1990	87500	43.970	93750	47.111	106200	53.367
2230	87500	39.238	93750	42.040	106200	47.623

Variation in magnetoelectric output with applied magnetic field is represented by the curves in Figure 4.39. At a given sintering temperature, dE/dH increased until the applied field reached to 1280 Oe for all composites. Beyond this field, magnetostriction of the ferrite reached saturation and hence constant electric field was produced in the piezoelectric phase. Therefore, dE/dH decreased upon increasing the applied field. This is a typical variation for ME composites seen in the literature. Magnitude of dE/dH increased upon soaking the composites at higher temperatures.

15N-85P and 20N-80P composites showed almost no piezoelectric activity; hence dE/dH variation with applied magnetic field could not be evaluated on those composites.

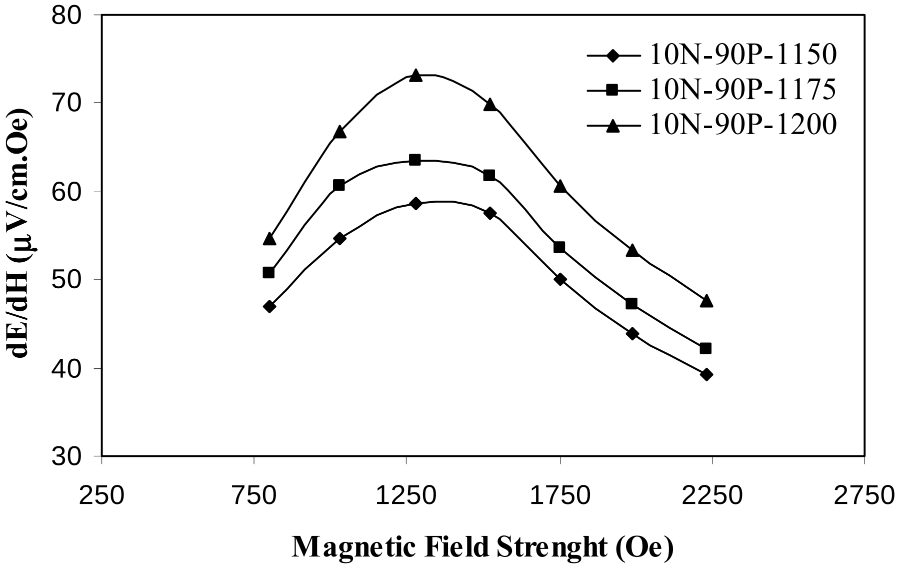

Figure 4.39 Variation in magnetoelectric output (dE/dH) with magnetic field strength for 10N-90P composites soaked at various temperatures.

4.5 Data and Results on Laminated ME Composite

Laminated ME composite was manufactured by sandwiching a PSZT-1250 disc between two NF+1Bi_2O_3 discs since highest piezoelectric strain coefficient was attained after soaking the PSZT ceramics at 1250 ºC and highest magnetostriction was observed in the NF ceramic modified with 1 wt% Bi_2O_3, according to the studies on piezoelectric and magnetostrictive ceramics in the present thesis work.

The data obtained throughout the measurement of magnetoelectric effect for the laminated ME composite is listed in Table 4.12. Supplementary oscilloscope screen images observed as a result of electrical output are shown in Figure C.4 in Appendix C.

Table 4.12 Values of applied magnetic field (H), voltage output (V) and ME output (dE/dH) of laminated ME composite.

Laminated ME Composite					
H (Oe)	**V (µV)**	**dE/dH (µV/cm·Oe)**	**H (Oe)**	**V (µV)**	**dE/dH (µV/cm·Oe)**
800	93750	117.188	2460	687500	279.472
1030	175000	169.903	2700	712500	263.889
1280	275000	214.844	2930	712500	243.174
1520	387500	254.934	3170	712500	224.763
1750	443700	253.543	3400	712500	209.559
1990	506200	254.372	3640	712500	195.742
2230	593800	266.278	3870	712500	184.109

The data is displayed in Figure 4.40. As noticed from the graph, dE/dH ratio varied in a similar trend with those of bulk ME composites. ME output of the laminated composite was greater than that of bulk composites.

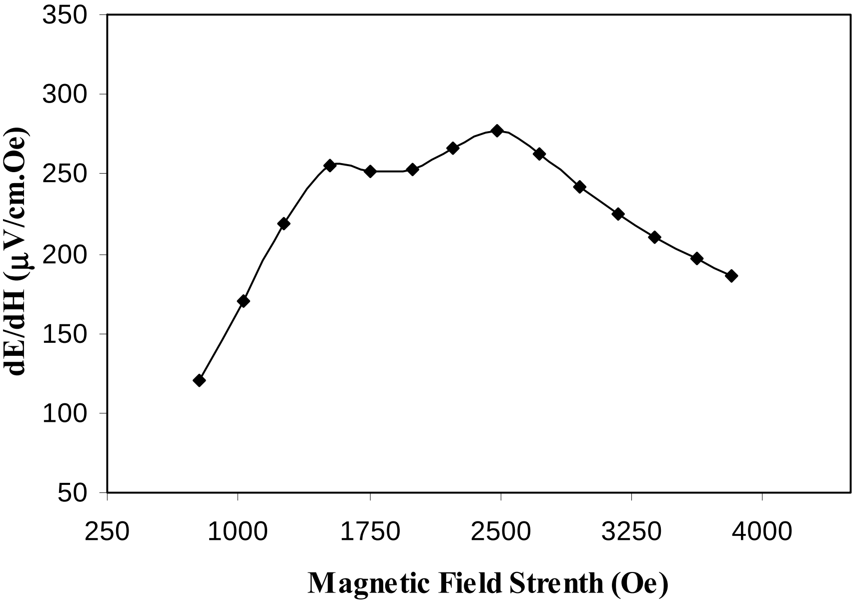

Figure 4.40 Variation in magnetoelectric output (dE/dH) with magnetic field strength for laminated ME composite.

CHAPTER 5

DISCUSSION AND CONCLUSIONS

The conversion of magnetic energy into electric form (or vice versa) is made possible with the utilization of magnetoelectric ceramic composites. The ME outputs observed in such composites are strongly dependent on the properties of their piezoelectric and magnetostrictive constituent phases. Therefore, with the aim of optimizing their properties, sintering studies on the piezoelectric and magnetostrictive components were performed in the first part of the present thesis work prior to the production of ME composites.

In accordance with the preliminary literature survey, the compositions having the molecular formula of $Pb_{0.95}Sr_{0.05}(Zr_{0.53}Ti_{0.47})O_3$+1wt%$Bi_2O_3$+0.4mol%MnO (PSZT) [17] and $NiCo_{0.02}Cu_{0.02}Mn_{0.10}Fe_{1.8}O_{4-k}$ (NF) [29] were selected as the piezoelectric and magnetostrictive constituents, respectively. These ceramics were sintered by soaking at temperatures between 1150 to 1250 ºC for a fixed duration of 2 h.

The dielectric and piezoelectric characterization of PSZT ceramics showed that properties improved at higher sintering temperature. Piezoelectric strain coefficient, dielectric constant and electromechanical coupling factor of the PSZT ceramics increased whereas loss tangent decreased. The mechanical quality factor did not show much variation with sintering temperature. Best properties were attained when ceramics were soaked at 1250 ºC. Results of the present study were similar to those of Çağatay's study [17] as seen in Table 5.1.

Table 5.1 Comparison of piezoelectric and dielectric results of the PSZT-1250 ceramic with Çağatay's study [17]. Ceramics were soaked for 2 h.

Ceramic	**T_{sint} (°C)**	**%TD**	**d_{33} (pC/N)**	**Q_m**	**K^T**	**tanδ**	**k_p**
PSZT [17]	1260	95.70	420	270	1300	0.007	0.48
PSZT	1250	93.02	434	163	1320	0.008	0.48

The enhancement in the properties of PSZT ceramics was attributed to the increase in grain size. This is in agreement with the study of Lal et al. [51]. They examined effects of sintering parameters on the microstructure and properties of PZT ceramic with $Pb_{0.94}Sr_{0.06}(Zr_{0.53}Ti_{0.47})O_3$ composition prepared by spray drying method. Ceramics were soaked between 1000 to 1250 ºC for 0.5 to 12 h. It was noted that with increasing sintering time and temperature, open porosity decreased due to pore closure and migration of pores through the grain boundaries. Moreover, increased grain size produced improvement in the values of dielectric constant, piezoelectric strain coefficient, electromechanical coupling factor and decreased loss tangent of the ceramic.

In the ferrite part of the present study, electrical and magnetic property determinations included DC-resistivity, initial magnetic permeability and magnetostriction measurements. DC-resistivity of NF ceramics showed slightly a decrease and then an increase with increasing sintering temperature. The initial reduction in ρ_{DC} was assigned to the increased grain size. Since grain boundaries act as obstacles to electron flow inside the microstructure, the enlargement in grain size resulted in decrease in grain boundary ratio, thus a decrease in DC-resistivity [52, 53]. Ferrite ceramics had closed and open pores within their microstructure. Open pores could act as conduction paths due to existence of impurities trapped inside [52]. At higher sintering temperatures, owing to the reduction of open pore concentration, increase in ρ_{DC} was observed.

Pores are accepted as demagnetizing fields in the microstructure and they have a retarding effect on the initial magnetic permeability [54, 55]. Accordingly, the initial magnetic permeability of NF samples increased slightly due to the reduction of pores via enhanced densification with sintering temperature.

NF ceramics showed poor densification at all sintering temperatures. In order to improve the sintered density, ferrites were modified with the sintering aid, Bi_2O_3. When ceramics were soaked in the presence of Bi_2O_3 liquid phase was formed, owing to the low melting point of Bi_2O_3, facilitating sintering with enhanced densification.

In the literature, there is an increasing trend of using Bi_2O_3 as a sintering additive, particularly in electrical and magnetic ceramics. Bismuth is seen to exert variable effects on the microstructure of the ceramics. In the present study, owing to the presence of Bi_2O_3 during sintering, significant enlargement in the average grain size was observed. Grains were uniformly distributed throughout the structure at all levels of Bi_2O_3 addition, implying homogeneous distribution of the second phase. For example, in the study of Mürbe et al. [31], conducted for low temperature firing of ferrite ceramics, a bimodal microstructure, where small grains were located between large grains, was observed for 0.5 wt% Bi_2O_3 addition. This was attributed to the heterogeneous distribution of the liquid phase.

Addition of Bi_2O_3 had a noticeable influence not only on the microstructure but also on the electrical and magnetic properties. DC-resistivity of ferrites increased an order of magnitude up to 1 wt% Bi_2O_3 addition and then it decreased. In the previous studies [30, 31] it was noted that the dopant Bi_2O_3 was located at grain boundaries. This phenomenon was also valid in the present study as observed from the BSE images. Therefore, enhancement in the DC-resistivity of ferrites could be attributed to the existence of highly resistive Bi_2O_3 at grain boundaries. The reason for the reduction in DC-resistivity at higher bismuth levels could be the increased concentration of Fe^{2+} in the presence of Bi_2O_3. Drofenik et al. [56] reported that, addition of Bi_2O_3 to MnZn ferrite increased FeO concentration. They noted that at higher temperatures, Bi^{3+} ions have a tendency for oxidation to Bi^{5+} ions promoting the formation of Fe^{2+} ions for charge neutrality. By analogy, the reduction in DC-resistivity of ferrites with further Bi_2O_3 additions could be attributed to the coexistence of Fe^{2+} and Fe^{3+} ions in the lattice, which enables polaron hopping.

Variation in initial magnetic permeability followed a similar trend with DC-resistivity such that it increased up to 1 wt% Bi_2O_3 addition, and then decreased with further Bi_2O_3 additions. The initial magnetic permeability spectrum of polycrystalline ferrites is composed of two mechanisms including spin rotation and domain wall motion [21, 57]. Van der Zaag et al. [58] reported that particles having grain size more than 3 μm are accepted as multidomain. As mentioned in Chapter 4, with the addition of Bi_2O_3 average grain size increased from 4 μm to 18 μm. Therefore, the increase in the initial magnetic permeability should be related closely to the contribution of domain walls. Beyond 1 wt% Bi_2O_3 addition, although particle size and density values remained constant, μ_i decreased. The decrease could be assigned to the presence of excess non-magnetic Bi_2O_3 phase at the grain boundaries [30, 52].

Existence of Bi_2O_3 also affected magnetostriction values of ferrite ceramics. For the bismuth free NF samples, the values slightly varied with sintering temperature; however, a significant increase was observed with the addition of 1 wt% Bi_2O_3. Since magnetostriction is partly associated with domain rotation and domain wall motion [1], higher λ could be attributed to the ease of domain rotation and movement with increased grain size. Further increase in bismuth concentration led to a reduction in magnetostriction. This may be due to the existence of excess Bi_2O_3 in the microstructure pinning the domain wall motion.

Studies on the ferrites showed that, highest DC-resistivity and magnetostriction, which are the key requirements for the magnetostrictive phase in an ME composite, were attained in the NF ceramic modified with 1 wt% Bi_2O_3.

Following completion of the studies on the constituent ceramics, ME composites were produced through two different techniques. The first attempt was the production of bulk composites. For this purpose, a disc compact consisting of 10 wt% NF powder and 90 wt% PSZT powder was sintered at temperatures between

1150 to 1200 ºC for 2 h. The upper limit of the firing temperature was dictated by liquid phase formation at about 1225 ºC. Because of partial fusion, the composite sintered at this temperature stuck to the saggar. Even at 1200 ºC, composite had a tendency for fusion, therefore ME composites having 15 and 20 wt% NF constituent were sintered at 1175 ºC.

Piezoelectric and dielectric properties of 10N-90P composites were generally inferior to those of pure PSZT ceramics. The decline in properties was attributed to the destruction of the continuity of the piezoelectric matrix by the spinel phase. In addition, due to the charge leakage through the low resistivity paths created by the ferrite phase, the applied electric field during the poling process was lower then 3 kV/mm. This was also one of the reasons why composites exhibited worse piezoelectric properties.

Studies on compositional variations in composites did not lead to an improvement in results. 15N-90P and 20N-80P composites exhibited poor densification such that the maximum composite density was only 71 % of the theoretical. These composites showed almost no piezoelectric activity when poled in a field of 1.25 kV/mm.

The problems such as liquid phase formation and charge leakage, which arise during the production of bulk ME composites in the present thesis work, were also reported in the literature by other researchers [4, 32, 43]. For example, in the study conducted by Zhai et al. [32] an additional peak, besides nickel ferrite (NFO) and PZT, was detected in the XRD pattern suggesting that a reaction occurred between NFO and PZT. This peak, which appeared at low NFO concentrations, vanished when NFO proportion was increased. Zhai et al. [32] also noted that piezoelectric properties of PZT weakened due to solid solution of Fe and/or Ni in PZT. At higher NFO concentration (>50 volume percentage), poling became difficult and NFO phase dominated the properties of the composite with its low resistivity; hence effective piezoelectric properties disappeared.

Li et al. [4] also showed that interdiffusion occurred between the constituent phases of ME composites. Moreover, they noted that when ferrite concentration exceeded a critical level, leakage currents occurred by the connection between the ferrite grains, which not only reduced resistivity of the composite but also hindered poling procedure.

Jiang et al. [43] stated that unwanted phases could be formed by chemical reactions as a result of high temperatures applied during sintering. The inter-phase diffusion of the atoms, which are difficult to verify, could facilitate defects and liquid phase formation by lowering the local eutectic points.

In ME effect measurements of bulk ME composites, variation of magnetoelectric output with applied field strength exhibited a typical behaviour. The ME outputs from 10N-90P composites increased with increasing sintering temperature. This was in agreement with the study of Ryu et al. [40] where ME effect of the composites increased with sintering temperature but decreased with larger ferrite proportion. The maximum value of 47.6 μV/cm·Oe was detected in the 10N-90P composite soaked at 1200 °C. No ME output was detected in 15N-90P and 20N-80P composites

In view of the low ME response in bulk composites, the second attempt in this thesis was centered on manufacturing the ME composites by stacking and bonding the individually sintered piezoelectric and magnetostrictive ceramic discs. A PSZT ceramic sintered at 1250 °C and a disc of the NF ceramic modified with 1 wt% Bi_2O_3 were selected as the components of the composite, due to their high piezoelectric strain coefficient and high magnetostriction, respectively.

The ME output of the layered composite was measured as 184 μV/cm·Oe, which was considerably higher than the values observed from bulk ME composites. This was rather expected since interfering events like existence of chemical reaction, liquid phase formation and the charge leakage through low resistive phase were completely prevented.

Present study showed conclusively that:

- PSZT ceramics showed ~93 %TD density at all sintering temperatures in the interval from 1150 to 1250 °C.
- Grain size increased from 5 μm to 12 μm with increasing sintering temperature.
- Dielectric and piezoelectric properties of PSZT ceramics were enhanced; piezoelectric strain coefficient increased from 369 pC/N to 434 pC/N, dielectric constant increased from 1163 to 1320, planar coupling coefficient increased from 0.44 to 0.48 and loss tangent decreased from 0.010 to 0.008 with increasing sintering temperature. Mechanical quality factor remained unchanged at approximately 160. Best piezoelectric and dielectric properties were obtained in PSZT ceramic sintered at 1250 ºC.
- NF ceramics exhibited poor densification at all sintering temperatures; reaching only 70 to 80 %TD.
- Bi_2O_3 was used as a sintering additive in order to improve sinterability of ferrites.
- Grain size increased from 4 μm to 18 μm when ceramics were modified with 3 wt% Bi_2O_3.
- Ferrites attained almost full densification when sintered in the presence of Bi_2O_3.
- Addition of Bi_2O_3 enhanced electrical and magnetic properties of ferrites. Best properties were obtained in NF ceramic modified with 1 wt% Bi_2O_3. DC-resistivity increased from 1.24×10^7 ohm-cm to 1.15×10^8 ohm-cm, longitudinal magnetostriction increased from 17.42 ppm to 25.48 ppm and initial magnetic permeability increased from 10.95 to 21.99 with 1 wt% Bi_2O_3 addition.

Studies on ME composites showed that:

- Bulk ME composites having 10 wt% NF and 90 wt% PSZT densified more than its individual phases. When NF fraction exceeded 10 wt%, poor densification was observed in ME composites.
- In bulk ME composites, liquid phase was developed by the dissolution of NF phase in PSZT matrix.

- Due to presence of low resistive NF phase in the PSZT matrix, charge leakage occurred during poling.
- Bulk composites showed poor piezoelectric and dielectric properties when compared to those of pure PSZT ceramics.
- Reactions, which occurred between the phases of a bulk ME composite during high temperature processing, rendered them weak and unreliable in ME response.
- Laminated composite exhibited higher ME output.

It should be emphasized, however, that the data obtained on the ME outputs of the two kinds of composites manufactured in the present study serve only purposes of comparison between the two types. Because of the lack of Helmholtz coil configuration, the data gathered cannot be compared with the ME outputs of similar composites reported in the literature.

In the extension of this study to the future, the priority should be given to the construction of an ME measurement setup which operates with a properly designed Helmholtz coil. Further attention should be given to the effect of ceramic thickness on the magnitude of the ME output in laminated composites. In general thinner ceramics are known to exhibit enhanced elastic conformity, therefore laminated ME composites produced by thin or thick film technologies may deserve more research interest.

REFERENCES

1. M. Fiebig, *Revival of Magnetoelectric Effect.* Journal of Physics D: Applied Physics, 2005. **38**: p. 123-152.

2. S. V. Suryanarayana, *Magnetoelectric Interaction Phenomena in Materials.* Bulletin of Material Science, 1994. **17**: p. 1259-1270.

3. S. L. Kadam, K. K. Patankar, C. M. Kanamadi, and B. K. Chougule, *Electrical Conduction and Magnetoelectric Effect in* $Ni_{0.50}Co_{0.50}Fe_2O_4$ + $Ba_{0.8}Pb_{0.2}TiO_3$ *Composites.* Materials Research Bulletin, 2004. **39**: p. 2265-2272.

4. Y. J. Li, X. M. Chen, Y. Q. Lin, and Y. H. Tang, *Magnetoelectric Effect of* $Ni_{0.8}Zn_{0.2}Fe_2O_4$ / $Sr_{0.5}Ba_{0.5}Nb_2O_6$ *Composites.* Journal of the European Ceramic Society, 2006. **26**: p. 2839-2844.

5. J. Ryu, S. Priya, K. Uchino, and H. E. Kim, *Magnetoelectric Effect in Composites of Magnetostrictive and Piezoelectric Materials.* Journal of Electroceramics, 2002. **8**: p. 107-119.

6. V. E. Wood and A. E. Austin, *Possible Applications for Magnetoelectric Materials*. Proceedings of Symposium on Magnetoelectric Interaction Phenomena in Crystals, ed. A. Freeman and A. Schmid. 1975, New York: Gordon and Breach Science Publishers.

7. S. R. Kulkarni, C. M. Kanamadi, and B. K. Chougule, *Dielectric and Magnetic Properties of* $(x)Ni_{0.8}Co_{0.1}Cu_{0.1}Fe_2O_4$ / $(1\text{-}x)PbZr_{0.8}Ti_{0.2}O_3$ *Composites.* Materials Research Bulletin, 2005. **40**: p. 2064-2072.

8. B. Jaffe, W. R. Cook, and H. Jaffe, *Piezoelectric Ceramics*. 1971: Academic Press.

9. ed. R. C. Buchanan, *Ceramic Materials for Electronics*. 2004, New York: Marcel Dekker Inc.

10. G. H. Haertling, *Ferroelectric Ceramics: History and Technology.* Journal of American Ceramic Society, 1999. **82**: p. 797-818.

11. L. Wu, C. C. Wei, T. S. Wu, and H. C. Liu, *Piezoelectric Properties of Modified PZT Ceramics.* Journal of Physics C: Solid State Physics, 1983. **16**: p. 2813-2821.

12. T. Ikeda, T. Okano, and M. Watanabe, *A Ternary System* $PbO\text{-}TiO_2\text{-}ZrO_2$. Japanese Journal of Applied Physics, 1962. **1**: p. 218-222.

13. S. Fushimi and T. Ikeda, *Phase Equilibrium in the System* $PbO\text{--}TiO_2\text{--}ZrO_2$. Journal of American Ceramic Society, 1967. **50**: p. 129-132.

14. C. A. Randall, N. Kim, J. P. Kucera, W. Cao, and T. R. Shrout, *Intrinsic and Extrinsic Size Effect in Fine-Grained Morphotropic-Phase-Boundary Lead Zirconate Titanate Ceramics.* Journal of American Ceramic Society, 1998. **81**: p. 677-688.

15. L. Longtu, D. Weiti, C. Jinghe, G. Zhilun, and Z. Xiaowen, *Lead Zirconate Titanate Ceramics and Monolithic Piezoelectric Transformer of Low Firing Temperature.* Ferroelectrics, 1990. **101**: p. 193-200.

16. L. He and C. Li, *Effect of Addition of MnO on Piezoelectric Properties of Lead Zirconate Titanate.* Journal of Materials Science, 2000. **35**: p. 2477-2480.

17. S. Çağatay, *Compositional Modifications of PZT Based Ceramics*. May 2000, Middle East Technical University.

18. E. C. Snelling, *Soft Ferrites: Properties and Applications*. 1 ed. 1969, London: Iliffe Books Ltd.

19. L. L. Hench and J. K. West, *Principles of Electronic Ceramics*. 1990, London: John Wiley & Sons.

20. C. Heck, *Magnetic Materials and Their Applications*. 1974, London: Butterworths.

21. J. Smit and H. P. J. Wijn, *Ferrites: Physical Properties of Ferrimagnetic Oxides in Relation to Their Technical Applications*. 1 ed. 1959 Eindhoven: Philips' Technical Library.

22. A. J. Moulson and J. M. Herbert, *Electroceramics: Materials, Properties, Applications*. 1 ed. 1990, London: Chapman & Hall.

23. G. Engdahl, *Handbook of Giant Magnetostrictive Materials*. 2000, San Diego: Academic Press.

24. E. Cedillo, J. Ocampo, V. Rivera, and R. Valenzuela, *An Apparatus for the Measurement of Initial Magnetic Permeability as a Function of Temperature.* Journal of Physics E: Scientific Instruments, 1980 **13**: p. 383-386.

25. W. D. Kingery, H. K. Bowen, and D. R. Uhlmann, *Introduction to Ceramics*. 1976, New York: John Wiley & Sons.

26. N. W. Grimes, *The Spinels: Versatile Materials.* Physics in Technology, 1975. **6**: p. 22-27.

27. M. I. Mendelson, *Average Grain Size in Polycrystalline Ceramics.* Journal of American Ceramic Society, 1969. **52**: p. 443-446.

28. L. G. V. Uitert, *High Resistivity in Nickel Ferrites-the Effect of Minor Additions of Manganese and Cobalt.* The Journal of Chemical Physics, 1956. **24**: p. 306-310.

29. T .G. Lupeiko, S. S. Lopatin, L. V. Lisnevskaya, and B. I. Zvyagintsev, *Magnetoelectric Composite Materials Based on Lead Zirconate Titanate and Nickel Ferrite.* Inorganic Materials, 1994. **30**: p. 1353-1356.

30. P. S. Kumar, S. R. Sainkar, J. J. Shrotri, S. D. Kulkarni, C. E. Deshpande, and S. K. Date, *Particle Size Dependence of Rotational Responses in Ni-Zn Ferrite.* Journal of Applied Physics, 1998. **83**: p. 6864-6866.

31. J. Mürbe and J. Töpfer, *Ni-Cu-Zn Ferrites for Low Temperature Firing: II. Effects of Powder Morphology and* Bi_2O_3 *Addition on Microstructure and Permeability.* Journal of Electroceramics, 2006. **16**: p. 199-205.

32. J. Zhai, N. Cai, Z. Shi, Y. Lin, and C. W. Nan, *Magnetic -Dielectric Properties of* $NiFe_2O_4$ */ PZT Particulate Composites.* Journal of Physics D: Applied Physics, 2004. **37**: p. 823-827.

33. G. Srinivasan, E. T. Rasmussen, J. Gallegos, and R. Srinivasan, *Magnetoelectric Bilayer and Multilayer Structures of Magnetostrictive and Piezoelectric Oxides.* Physical Review B, 2001. **64** (214408): p. 1-6.

34. G. A. Smolenskii and I. E. Chupis, *Problems in Solid State Physics*. 1984, Moscow: Mir Publishers.

35. J. Van Den Boomgaard and R. A. J. Born, *A Sintered Magnetoelectric Composite Material* $BaTiO_3$ *-* $Ni(Co,Mn)Fe_2O_4$*.* Journal of Materials Science, 1978. **13**: p. 1538-1548.

36. J. V. Suchtelen, *Product Properties: A New Application of Composite Materials* Philips Research Reports, 1972. **27**: p. 28-37.

37. J. Van Den Boomgaard, D. R. Terrell, R. A. J. Born, and H. F. J. I. Giller, *An In Situ Grown Eutectic Magnetoelectric Composite Material Part 1 Composition and Unidirectional Solidification.* Journal of Materials Science, 1974. **9**: p. 1705-1709.

38. A. M. J. G. Van Run, D. R. Terrell, and J. H. Scholing, *An In Situ Grown Eutectic Magnetoelectric Composite Material Part 2 Physical Properties.* Journal of Materials Science, 1974. **9**: p. 1710-1714.

39. S. Mazumder and G. S. Bhattacharyya, *Synthesis and Characterization of In Situ Grown Magnetoelectric Composites in the BaO- TiO- FeO- CoO System.* Ceramics International, 2004. **30**: p. 389-392.

40. J. Ryu, A. V. Carazo, K. Uchino, and H. Kim, *Piezoelectric and Magnetoelectric Properties of Lead Zirconate Titanate / Ni-Ferrite Particulate Composites.* Journal of Electroceramics, 2001. **7**: p. 17-24.

41. K. K. Patankar, S. L. Kadam, V. L. Mathe, C. M. Kanamadi, V. P. Kothawale, and B. K. Chougule, *Dielectric Behaviour and Magnetoelectric Effect in* $Ni_{0.25}Co_{0.75}Fe_2O_4$ - $Ba_{0.8}Pb_{0.2}TiO_3$ *Ceramic Composites.* British Ceramic Transactions, 2003. **102**: p. 19-22.

42. S. S. Chougule and B. K. Chougule, *Response of Dielectric Behaviour on Ferroelectric rich (y)* $Ni_{0.8}Zn_{0.2}Fe_2O_4$ + $(1 - y)$ *PZT ME Composites.* Materials Chemistry and Physics, 2007. **108**: p. 408-412.

43. Q. H. Jiang, Z. J. Shen, J. P. Zhou, Z. Shi, and C. W. Nan, *Magnetoelectric Composites of Nickel Ferrite and Lead Zirconate Titanate Prepared by Spark Plasma Sintering.* Journal of the European Ceramic Society, 2007. **27**: p. 279-284.

44. J. Ryu, S. Priya, A. V. Carazo, K. Uchino, and H. E. Kim, *Effect of the Magnetostrictive Layer on Magnetoelectric Properties in Lead Zirconate Titanate/Terfenol-D Laminate Composites.* Journal of American Ceramic Society, 2001. **84**: p. 2905-2908.

45. G. Srinivasan, E. T. Rasmussen, A. A. Bush, K. E. Kamentsev, V. F. Meshcheryakov, and Y. K. Fetisov, *Structural and Magnetoelectric Properties of* MFe_2O_4*-PZT (M=Ni, Co) and* $La_x(Ca,Sr)_{1-x}MnO_3$*-PZT Multilayer Composites.* Applied Physics A, 2004. **78**: p. 721-728.

46. J. Ryu, S. Priya, K. Uchino, H. E. Kim, and D. Viehland, *High Magnetoelectric Properties in* $0.68Pb(Mg_{1/3}Nb_{2/3})O_3$*-*$0.32PbTiO_3$ *Single Crystal and Terfenol-D Laminate Composites.* Journal of the Korean Ceramic Society, 2002. **39**: p. 813-817.

47. K. K. Patankar, V. L. Mathe, R. P. Mahajan, S. A. Patil, R. M. Reddy, and K. V. SivaKumar, *Dielectric Behaviour and Magnetoelectric Effect in* $CuFe_2O_4$*-*$Ba_{0.8}Pb_{0.2}TiO_3$ *Composites.* Materials Chemistry and Physics, 2001. **72**: p. 23-29.

48. R. P. Mahajan, K. K. Patankar, M. B. Kothale, S. C. Chaudhari, V. L. Mathe, and S. A. Patil, *Magnetoelectric Effect in Cobalt Ferrite-Barium Titanate Composites and Their Electrical Properties.* Journal of Physics, 2002. **58**: p. 1115-1124.

49. S. K. Saha and D. C. Agrawal, *Composition Fluctuations and Their Influence on the Properties of Lead Zirconate Titanate Ceramics.* American Ceramic Society Bulletin, 1992. **71**: p. 1424-1428.

50. *IRE Standards on Piezoelectric Crystals, Measurement of Piezoelectric Ceramics, Proc. IRE, 611RE, 14S1*. 1961.

51. R. Lal, N. M. Gokhale, R. Krishnan, and P. Ramakrishnan, *Effect of Sintering Parameters on the Microstructure and Properties of Strontium Modified PZT Ceramics Prepared Using Spray-Dried Powders.* Journal of Materials Science, 1989. **24**: p. 2911-2916.

52. L. B. Kong, Z. W. Li, G. Q. Lin, and Y. B. Gan, *Electrical and Magnetic Properties of Magnesium Ferrite Ceramics Doped with Bi_2O_3.* Acta Materialia, 2007. **55**: p. 6561-6572.

53. K. O. Low and F. R. Sale, *Electromagnetic Properties of Gel-derived NiCuZn Ferrites.* Journal of Magnetism and Magnetic Materials, 2002. **246**: p. 30-35.

54. J. J. Shrotri, S. D. Kulkarni, C. E. Deshpande, A. Mitra, S. R. Sainkar, P. S. Kumar, and S. K. Date, *Effect of Cu Substitution on the Magnetic and Electrical Properties of Ni-Zn Ferrite Synthesized by Soft Chemical Method.* Materials Chemistry and Physics, 1999. **59**: p. 1-5.

55. S. F. Wang, Y. R. Wang, T. Yang, C. F. Chen, C. A. Lu, and C. Y. Huang, *Densification and Magnetic Properties of Low-Fire NiCuZn Ferrites.* Journal of Magnetism and Magnetic Materials, 2000. **220**: p. 129-138.

56. M. Drofenik, Z. Andrej, and D. Makovec, *Influence of the Addition of Bi_2O_3 on the Grain Growth and Magnetic Permeability of MnZn Ferrites.* Journal of American Ceramic Society, 1998. **81**: p. 2841-2848.

57. T. Tsutaoka, M. Ueshima, T. Tokunaga, T. Nakamura, and K. Hatakeyama, *Frequency Dispersion and Temperature Variation of Complex Permeability of Ni-Zn Ferrite Composite Materials.* Journal of Applied Physics, 1995. **78**: p. 3983-3991.

58. P. J. van der Zaag, P. J. van der Valk, and M. T. Rekveldt, *A Domain Size Effect in the Magnetic Hysteresis of NiZn-Ferrites.* Applied Physics Letters, 1996. **69**: p. 2927-2929.

APPENDIX A

MAGNETOSTRICTION DATA OF NF CERAMICS

Table A.1 Data of magnetic field strength, H, and transverse magnetostriction, $\lambda(\perp)$, of NF ceramics soaked at various temperatures.

	NF-1150	**NF-1175**	**NF-1200**	**NF-1225**	**NF-1250**
H (Oe)	**$\lambda(\perp)$ (ppm)**	**$\lambda(\perp)$ (ppm)**	**$\lambda(\perp)$ (ppm)**	**$\lambda(\perp)$ (ppm)**	**$\lambda(\perp)$ (ppm)**
0	0	0	0	0	0
70	0.11	0.54	0.64	0.41	0.79
150	0.89	1.55	1.33	1.47	1.66
220	2.12	2.86	2.79	2.73	3.03
300	3.27	4.07	4.08	3.97	4.43
370	4.36	5.12	5.22	5.17	5.63
450	5.46	6.21	6.31	6.14	6.82
530	6.3	6.93	7.06	7.04	7.77
610	6.92	7.78	7.88	7.44	8.48
680	7.48	8.24	8.49	8.05	9.08
760	8.03	8.94	8.96	8.58	9.65
840	8.36	9.35	9.4	9.01	10.05
940	8.75	9.66	9.87	9.25	10.34
1020	8.87	9.96	9.98	9.52	10.64
1090	9.23	10.13	10.37	9.75	10.87
1170	9.51	10.25	10.44	9.97	11.11
1250	9.75	10.26	10.64	10.13	11.33

Table A.2 Data of magnetic field strength, H, and longitudinal magnetostriction, λ(//), of NF ceramics soaked at various temperatures.

H (Oe)	**NF-1150**	**NF-1175**	**NF-1200**	**NF-1225**	**NF-1250**
	λ(//) (ppm)	**λ(//) (ppm)**	**λ(//) (ppm)**	**λ(//) (ppm)**	**λ(//) (ppm)**
0	0	0	0	0	0
110	-0.36	-1.11	-0.32	-0.38	-0.29
150	-2.23	-2.7	-1.65	-1.64	-1.33
190	-4.22	-4.67	-3.19	-3.25	-2.59
230	-6.32	-6.64	-4.94	-5.22	-4.27
270	-7.87	-8.44	-6.86	-7.07	-6.17
310	-9.23	-10.1	-8.45	-8.93	-7.91
350	-10.58	-11.47	-9.82	-10.38	-9.45
400	-11.63	-12.83	-10.98	-11.7	-10.73
440	-12.77	-13.84	-11.99	-12.8	-11.81
480	-13.78	-14.85	-12.9	-13.72	-12.77
530	-14.69	-15.55	-13.65	-14.41	-13.53
570	-15.18	-16.25	-14.54	-15.14	-14.2
620	-15.65	-16.85	-15.11	-15.79	-14.75
660	-16.14	-17.38	-15.53	-16.3	-15.22
700	-16.61	-17.87	-15.91	-16.71	-15.73
750	-17.07	-18.15	-16.29	-16.96	-16.05
790	-17.28	-18.56	-16.49	-17.2	-16.16
840	-17.53	-18.81	-16.72	-17.59	-16.36
940	-18.11	-19.32	-17.19	-17.88	-16.8
1030	-18.32	-19.57	-17.42	-18.16	-16.94
1120	-18.7	-19.99	-17.85	-18.54	-17.33
1250	-18.9	-20.16	-17.81	-18.79	-17.42

Table A.3 Data of magnetic field strength, H, and transverse magnetostriction, λ(⊥), of bismuth modified NF ceramics. Ceramics were soaked at 1250 °C for 2 h.

H (Oe)	NF+0.5 Bi_2O_3 λ(⊥) (ppm)	NF+1 Bi_2O_3 λ(⊥) (ppm)	NF+2 Bi_2O_3 λ(⊥) (ppm)	NF+3 Bi_2O_3 λ(⊥) (ppm)
0	0	0	0	0
70	0.48	0.8	0.31	0.32
150	1.58	1.87	1.26	0.87
220	2.87	3.11	2.35	1.79
300	4.53	4.66	4.09	3.42
370	6.44	6.61	5.85	5.05
450	8.14	8.4	7.59	6.7
530	9.52	9.92	8.91	8.02
610	10.41	10.93	9.73	9.21
680	11.01	11.63	10.29	9.97
760	11.52	12.12	10.61	10.52
840	11.83	12.54	10.93	10.55
940	12.14	12.8	11.09	10.73
1020	12.35	13.04	11.29	10.96
1090	12.54	13.32	11.34	11.27
1170	12.75	13.37	11.46	11.55
1250	12.81	13.57	11.55	11.6

Table A.4 Data of magnetic field strength, H, and longitudinal magnetostriction, λ(//), of bismuth modified NF ceramics. Ceramics were soaked at 1250 °C for 2 h.

H (Oe)	**NF+0.5 Bi_2O_3**	**NF+1 Bi_2O_3**	**NF+2 Bi_2O_3**	**NF+3 Bi_2O_3**
	λ(//) (ppm)	**λ(//) (ppm)**	**λ(//) (ppm)**	**λ(//) (ppm)**
0	0	0	0	0
110	-0.23	-0.91	-0.92	-0.78
150	-1.34	-2	-2.19	-1.75
190	-2.53	-3.54	-3.51	-2.92
230	-4.17	-5.16	-5.49	-4.51
270	-6.01	-7.17	-7.26	-6.46
310	-7.94	-9.35	-9.34	-8.51
350	-10.2	-11.75	-11.73	-10.95
400	-12.82	-14.1	-14.13	-12.60
440	-14.68	-16.27	-16.14	-14.66
480	-16.09	-18.23	-18.48	-16.02
530	-17.27	-19.7	-19.35	-17.12
570	-18.35	-21.2	-20.5	-18.13
620	-18.86	-21.74	-21.12	-18.85
660	-19.5	-22.43	-21.77	-19.34
700	-19.82	-22.96	-22.12	-19.91
750	-20.22	-23.56	-22.41	-20.2
790	-20.38	-24.08	-22.78	-20.51
840	-20.62	-24.44	-22.93	-20.68
940	-20.91	-25.03	-23.09	-20.91
1030	-21.17	-25.07	-23.53	-21.03
1120	-21.27	-25.23	-23.42	-21.01
1250	-21.33	-25.48	-23.53	-21.01

APPENDIX B

SEM IMAGES OF BULK ME COMPOSITES

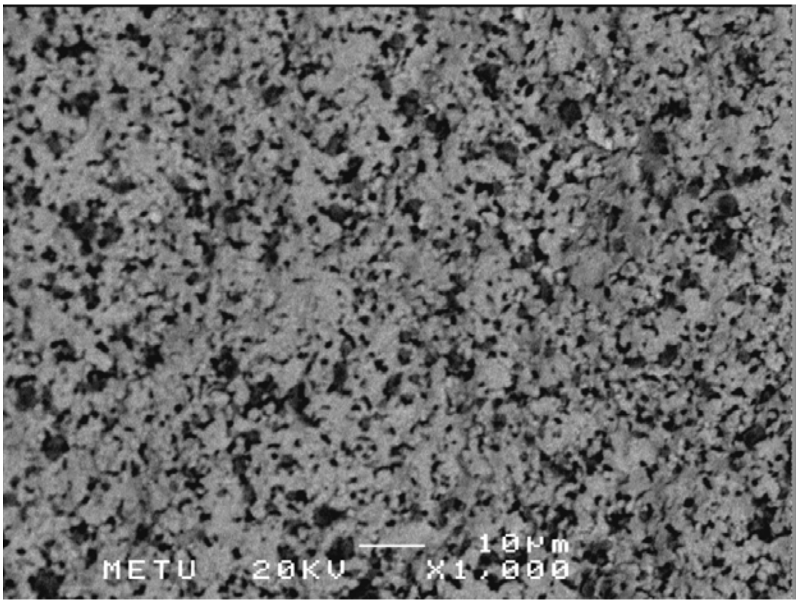

Figure B.1 BSE image of the 10N-90P ceramic sintered at 1150 ºC for 2 h.

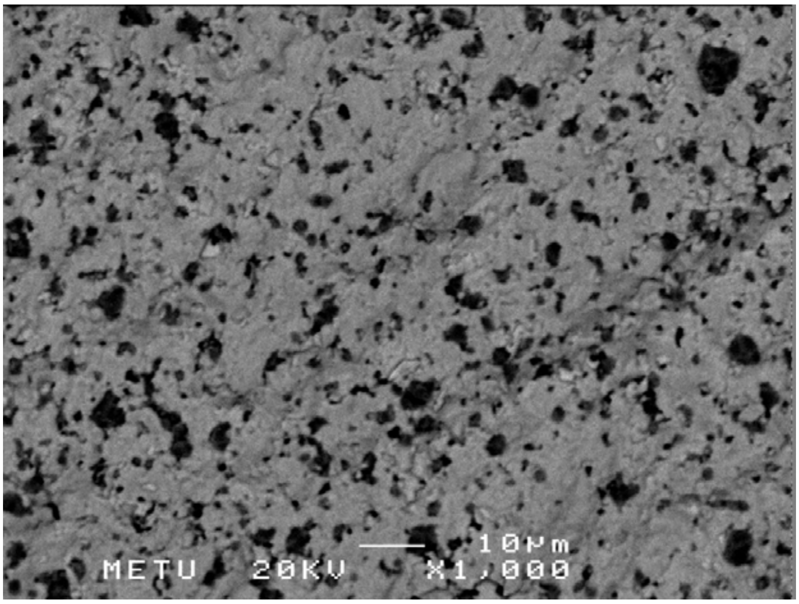

Figure B.2 BSE image of the 10N-90P ceramic sintered at 1175 ºC for 2 h.

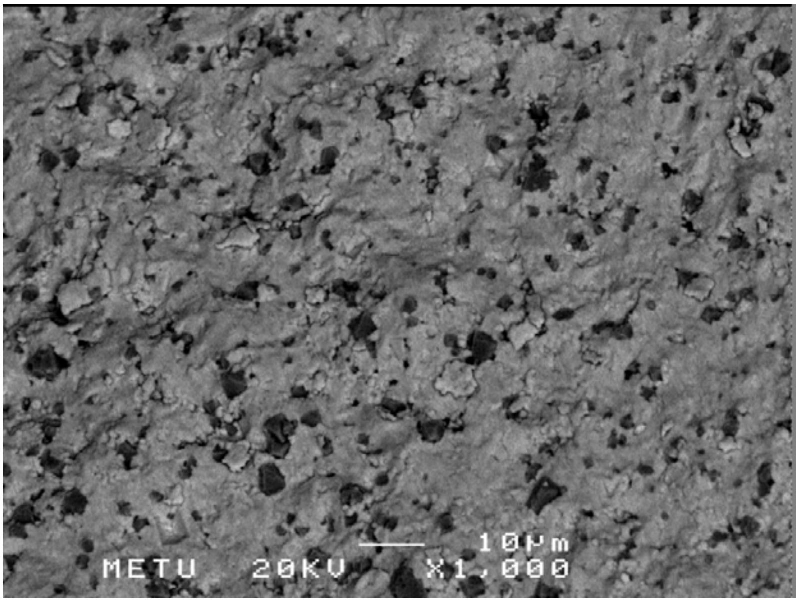

Figure B.3 BSE image of the 10N-90P ceramic sintered at 1200 ºC for 2 h.

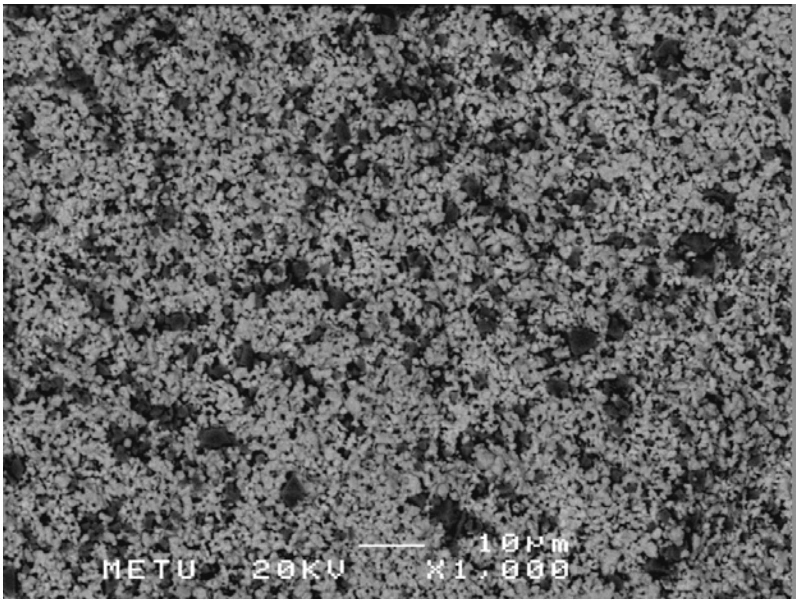

Figure B.4 BSE image of the 15N-85P ceramic sintered at 1175 ºC for 2 h.

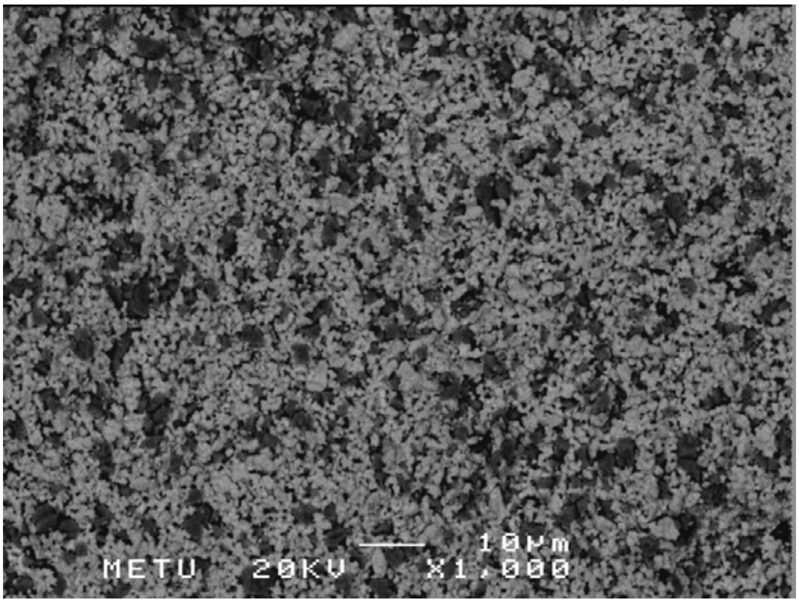

Figure B.5 BSE image of the 20N-80P ceramic sintered at 1175 ºC for 2 h.

APPENDIX C

OSCILLOSCOPE SCREEN IMAGES FROM MAGNETOELECTRIC EFFECT MEASUREMENTS

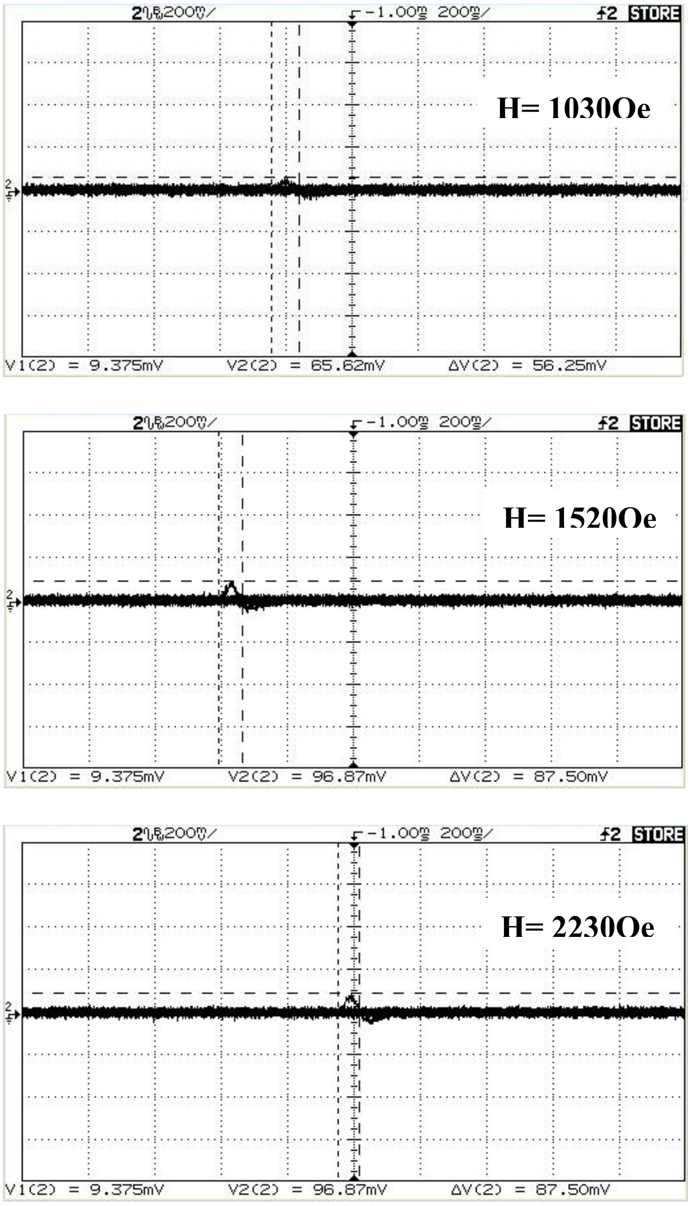

Figure C.1 Oscilloscope screen images at different magnetic field strengths for the 10N-90P-1150 bulk ME composite.

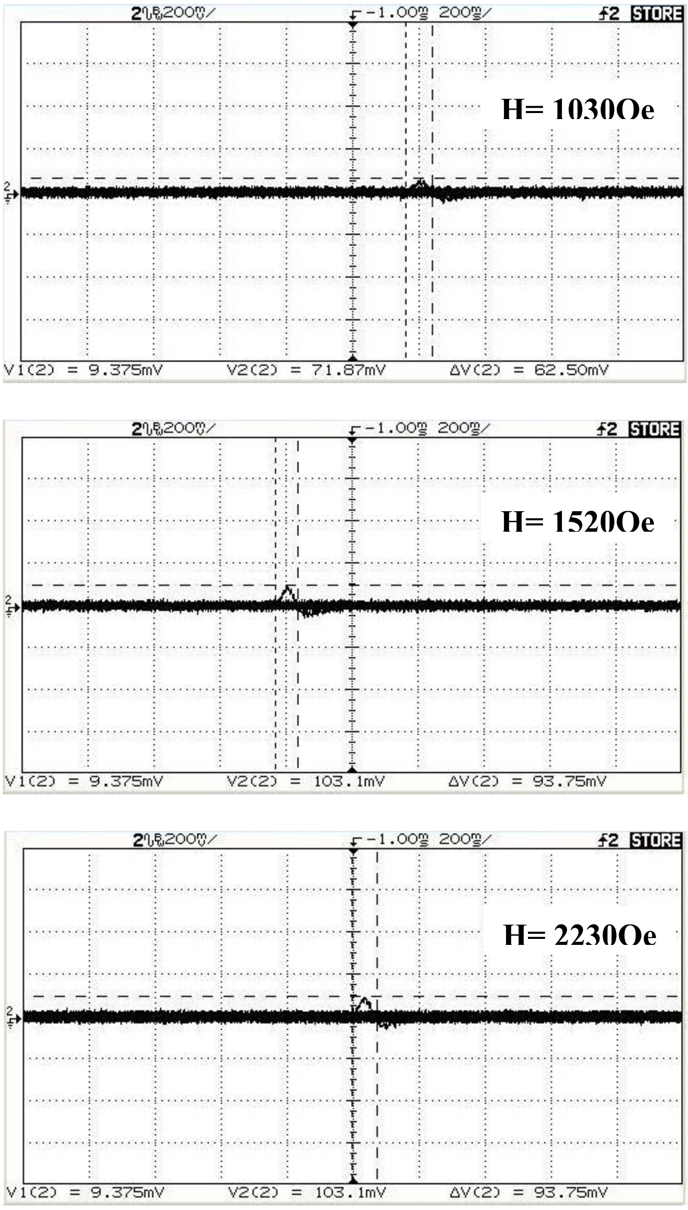

Figure C.2 Oscilloscope screen images at different magnetic field strengths for the 10N-90P-1175 bulk ME composite.

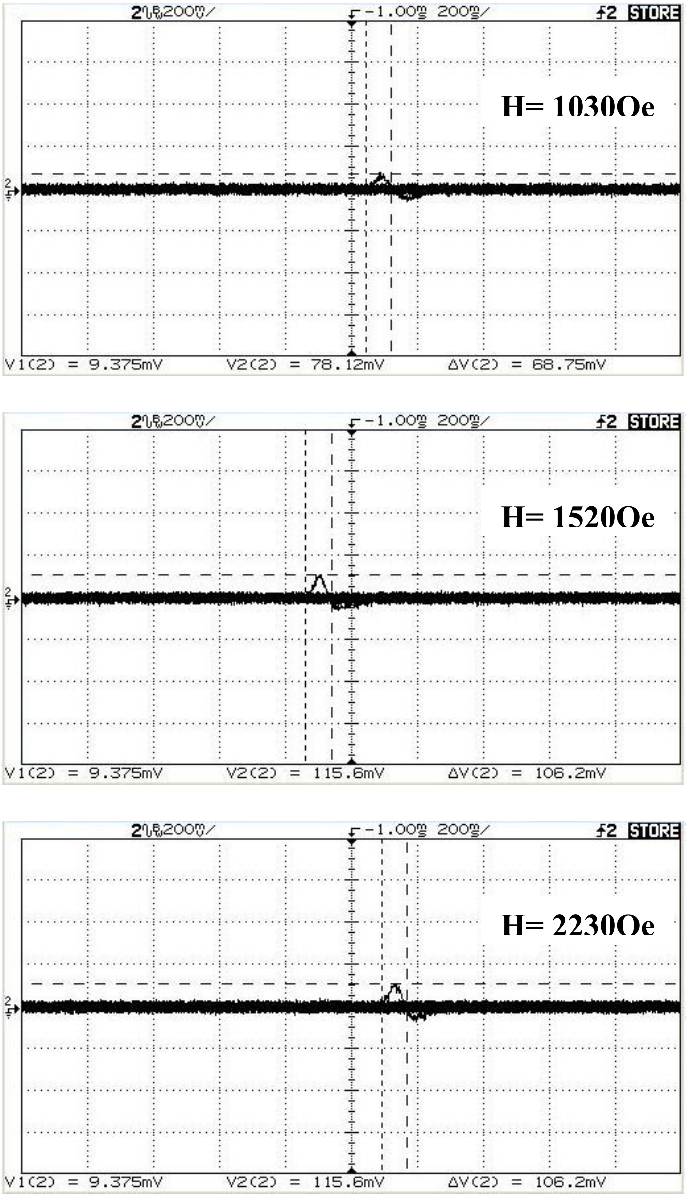

Figure C.3 Oscilloscope screen images at different magnetic field strengths for the 10N-90P-1200 bulk ME composite.

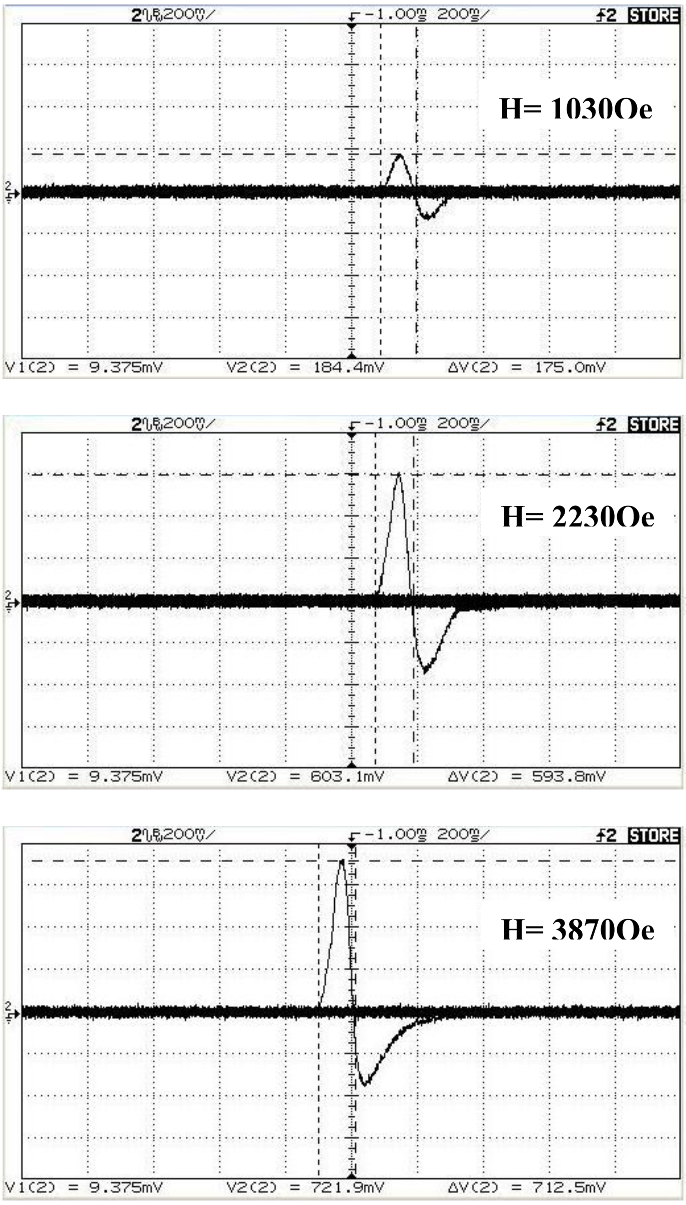

Figure C.4 Oscilloscope screen images at different magnetic field strengths for the laminated ME composite.